Russell G. Herron, Commander, U. S. Navy

PROTON MEASUREMENTS ON A ROCKET PROBE INTO THE SOUTH ATLANTIC RADIATION ANOMALY.

PROTON MEASUREMENTS ON A ROCKET PROBE INTO THE SOUTH ATLANTIC RADIATION ANOMALY

By

Russell G. Herron
Commander, U. S. Navy

A Dissertation

Submitted in Partial Fulfillment of the

Requirements for the Degree of

Doctor of Philosophy in Physics

The University of New Mexico

1965

FOREWORD

Technological advances during the last few decades have provided experimenters with powerful methods and tools to probe for new knowledge. Prominent among these advances has been the birth and phenomenal growth of space technology. Experiments can now be conducted beyond the limiting environs of Earth. Today, at increasingly frequent intervals, rockets are carrying men and experimental equipment into Nature's laboratory of space. The many contributions to the recent literature of numerous scientific disciplines indicate the great variety of space exploration now in progress. Because of its scope, complexity, and expense, this exploration requires the closest cooperation among scientists, engineers, and governmental agencies.

In the following sections, the concepts, design philosophies, results, and interpretations of one such experiment will be discussed. The research reported herein was commenced by the author while on military assignment at the University of New Mexico in the Doctoral Studies Program of the U. S. Navy. Details of this naval postgraduate program can be found in BUPERS INST 1520.50A of 14 January 1963.

The instrument, a proton scintillation spectrometer, was designed and constructed by the author with the extensive aid of the Space Physics Branch of the Air Force Weapons Laboratory, Kirtland Air Force Base, Albuquerque, New Mexico, under a contract with the University of New Mexico. The space flight was sponsored by the U. S. Atomic Energy Commission under the High Altitude Physics Group, E. O. Lawrence Radiation Laboratory, Livermore, California. Operations at sea were conducted and telemetry support for the water launch of the rocket in the South Atlantic Ocean was given by the Atlantic Test Range ship Twin Falls Victory. The techniques of water launch, which made possible this first vertical rocket probe of the South Atlantic Radiation Anomaly, were developed by personnel from the U. S. Naval Missile Center,

Point Mugu, California.

Acknowledgment is made to the many personnel of the aforementioned groups who assisted in the design, fabrication, testing, and launch of the flight instrument. Special thanks are due to F. C. Gilbert and F. D. Seward, of the Lawrence Radiation Laboratory, for acquainting me with the subject area of radiation anomalies. Grateful recognition is also given to D. J. Knecht, P. Dyal, W. E. Cantrell, and E. L. Breen, of the Air Force Weapons Laboratory, and especially Professor C. P. Leavitt of the Physics Department, University of New Mexico, who were always willing to advise possible courses of action.

PROTON MEASUREMENTS ON A ROCKET PROBE INTO THE SOUTH ATLANTIC RADIATION ANOMALY

ABSTRACT

On January 26, 1965 a proton scintillation spectrometer was carried to an apogee of 285 km in the South Atlantic Radiation Anomaly by a two-stage rocket which was launched vertically from a water-launch site in the South Atlantic Ocean in the vicinity of longitude 35°42'W and latitude 34°36'S. A detailed description is given of the experimental concepts, design philosophies, and system selection criteria used in the design and development of the proton scintillation spectrometer. Construction specifications and electronic circuitry are presented for the instrument, which consisted basically of a directional radiation telescope comprised of three detectors, and associated pulse-height analyzers and circuitry necessary to register the flux characteristics (energy and counting rates) of radiations that activated the telescope. Methods used in qualifying the instrument for space flight including calibration procedures are discussed. A brief discussion of water-launch operations is made. The actual flight trajectory is established by correlating radar track of the payload to 203 km with a computed trajectory based upon vehicle performance in earlier test firings. The experimental results are developed indicating the methods and procedures used in data reduction. Approximately 400 seconds of useful telemetry information was obtained from experimental turn-on at 160 km up through apogee at 285 km and down until reentry tumbling occurred at about 75 km. A plot of the counting rates of the phosphor guard fluor detector versus the inverse of the atmospheric density displays a direct relationship between altitudes of 150 km and 280 km, thereby establishing atmospheric interactions to be the primary cause of decreased counting rates in radiations that activated the guard fluor. Scale heights of the atmosphere over the range 150 to 280 km are calculated from the counting rates and found to

be in excellent agreement with the U. S. Standard Atmosphere, 1962. The proton energy spectrum near apogee (285±2 km) is determined based upon eight energy-dependent channels between 1 and 110 Mev. The spectrum is in good agreement with other experimenters and verifies that the spectrum rises sharply at low energies below the local inflection point in the vicinity of 20 Mev. The directional asymmetry of the proton flux, expected to be in an East-West plane near the mirror points in the South Atlantic Radiation Anomaly, was observed qualitatively for 8-10 Mev protons. Based upon preliminary analysis of data, an East-West asymmetry ratio of 1.15±0.1 is calculated. Some uncertainties in the results due to excessive R-F pickup noise in one detector channel and the geometrical and electrical resolution of the instrument are discussed.

CONTENTS

ILLUSTRATIONS

ILLUSTRATIONS (cont'd)

ILLUSTRATIONS (cont'd)

TABLES

SECTION I

EARLIER INVESTIGATIONS

1. Geomagnetically Trapped Radiation

A summary of results of space measurements during the 1950's has been published by Rossi (reference 1). Foremost among these results was the discovery of geomagnetically trapped radiation observed in increased counting rates in geiger counters on Sputnik II and Explorer I. In 1958, Van Allen (reference 2) correctly interpreted these experiments in terms of belts of geomagnetically trapped particles. In 1961, Singer and Lenchek (reference 3) reviewed progress in the burgeoning field of geomagnetically trapped radiation. In September 1962, Rosen et al. (reference 4) summarized the accepted information on the space radiation environment in a convenient handbook. A principal feature of this handbook is the Space Radiation Map which is shown in figure 1. The four regions shown in this map are categorized by Rosen according to their quasi-steady state properties as follows:

> The Inner Radiation Zone: A region characterized by the presence of large fluxes (>100 protons/cm^2 sec) of trapped protons with E>10 Mev, and small time variations in intensity which are temporally correlated with major solar proton events and/or major geomagnetic storms.
>
> The Outer Radiation Zone: A region characterized by the absence of large fluxes of protons with E>10 Mev, and large time variations in intensity without as clear a correlation with major solar proton events and/or geomagnetic storms.
>
> The Auroral Zone: A region containing the particles which directly cause the visible aurora.
>
> Interplanetary Space: The region external to the three aforementioned regions.

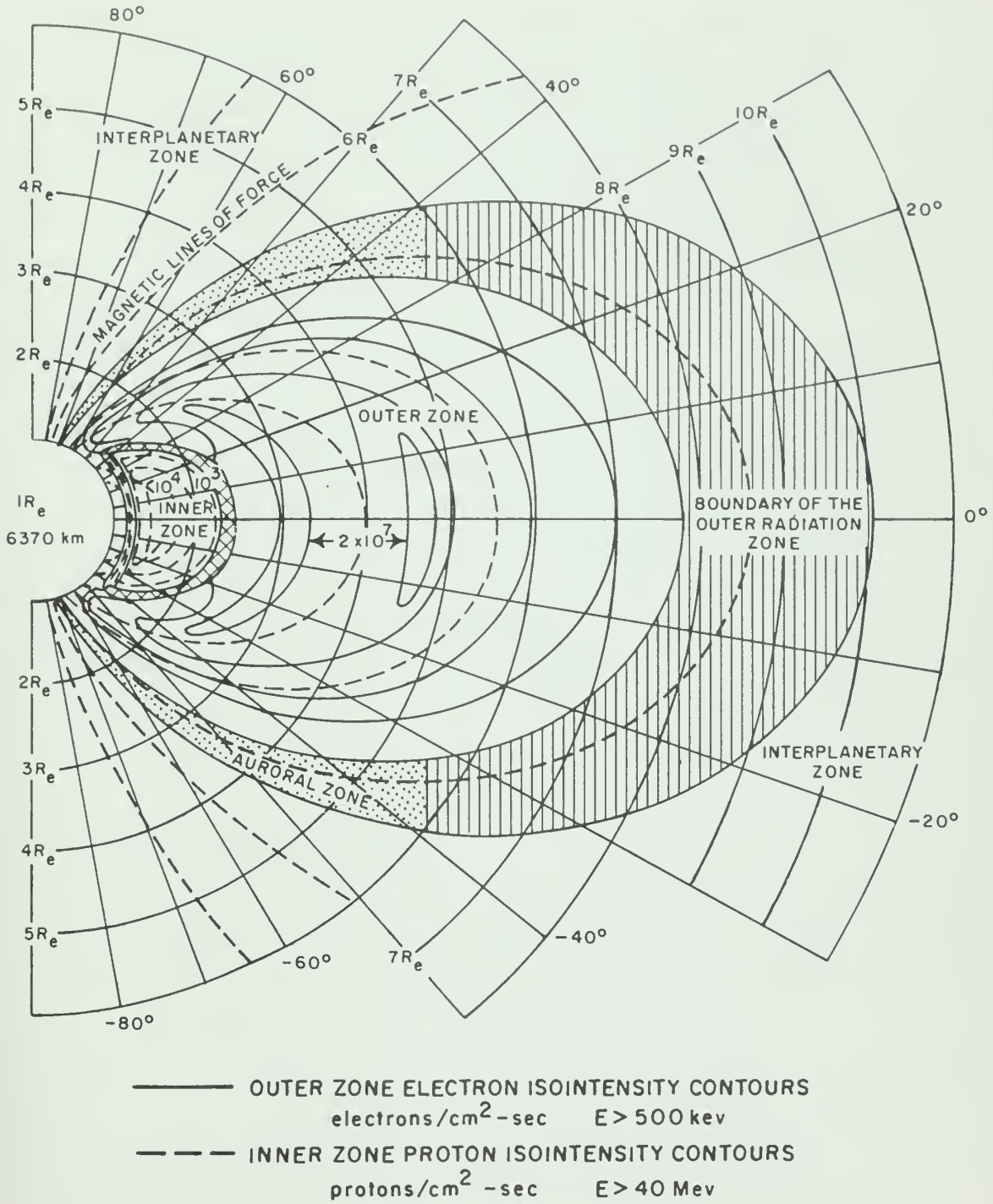

Figure 1. Geomagnetic Meridian Projection Map of the Space Radiation Environment (After Rosen et al., ref. 4)

The characteristics of radiation in these four regions are not completely determined. In particular, atomic tests conducted by the United States and the Soviet Union, especially the U. S. detonation on July 9, 1962, have produced artificial radiation belts. These artificial belts, composed mostly of electrons, can vitally affect the composition, structure, intensity, and energy spectrum of particles trapped in the Inner Radiation Zone. These effects were not considered in figure 1 for the Inner Radiation Zone. This figure should be regarded as characteristic of that region prior to the July 9, 1962, detonation. In addition, the radiation properties of the inner radiation zone are not easy to determine experimentally because of the difficulties inherent in separating the penetrating proton component superimposed on the intense electron component. Hence, although the presence of belts of geomagnetically trapped radiation is definitely established, new and more definitive experiments are necessary to determine fully the space radiation environment. Only with such additional data will it be possible to judge the correctness of current theories on the nature and origin of geomagnetically trapped particles.

2. Near-Earth Radiation Anomalies

Despite the disturbing influence of artificial belts and the inherent experimental difficulties mentioned earlier, scientific exploration of the Inner Radiation Zone is the principal means of gathering information needed for a full understanding of the space radiation environment closest to Earth. In figure 1, the inner edge of the Inner Radiation Zone is depicted at an altitude of about 1000 km. This is an oversimplification of the meager experimental evidence; the altitude of this inner edge does not hold constant over the complete surface of the earth. Trapped radiations have been measured far below 1000 km. For ease of reference, the region of space below 500 km will be referred to as near-Earth space, which space is well below the average altitude of the inner edge of the Inner Radiation Zone. A radiation

anomaly in this region will be said to exist if the radiation intensity at the maximum of the anomaly is appreciably greater (about two orders of magnitude) than radiation intensity in neighboring regions outside the anomaly. Near-Earth radiation anomalies of significant intensities have been experimentally observed and theoretical conjectures about their origins appear in the literature. The subject of the nature and origin of near-Earth radiation anomalies is an active frontier in space physics.

a. Experimental Observations

In 1961, Kurnosova et al. (reference 5) reported the discovery of radiation anomalies above the South Atlantic Ocean at heights of 310-340 km. A gas-discharge counter telescope, capable of recording electrons with an energy over 8 Mev and protons with an energy over 60 Mev, was carried in an orbiting satellite. An anomalously high counting rate was measured in the South Atlantic. The region of maximum intensity was located near 35°S latitude and 25°W longitude. The number of counts in the region of maximum intensity was about two orders of magnitude greater than the number of counts recorded by the telescope in neighboring regions lying outside the anomaly. No definite conclusions were advanced by Kurnosova concerning the nature of the radiation in this Southern Atlantic Anomaly. Conjecture was made, however, that the Southern Atlantic Anomaly and another Southern Anomaly located between 50-65°S latitude and 30-40°E longitude were connected with the existence in the southern hemisphere of large negative magnetic anomalies, i.e., areas in which the magnetic field strength is less than the normal field strength expected at a given geomagnetic latitude. A geographical plot showing the projection onto Earth's surface of these regions of anomalous radiation intensity is shown in figure 2. The two separate southern anomalies are presented as well as a Northern Anomaly in Eastern Siberia. This Northern Anomaly was observed only on one orbit of the satellite. It was considered not stable in time. Kurnosova conjectured that it may be connected with

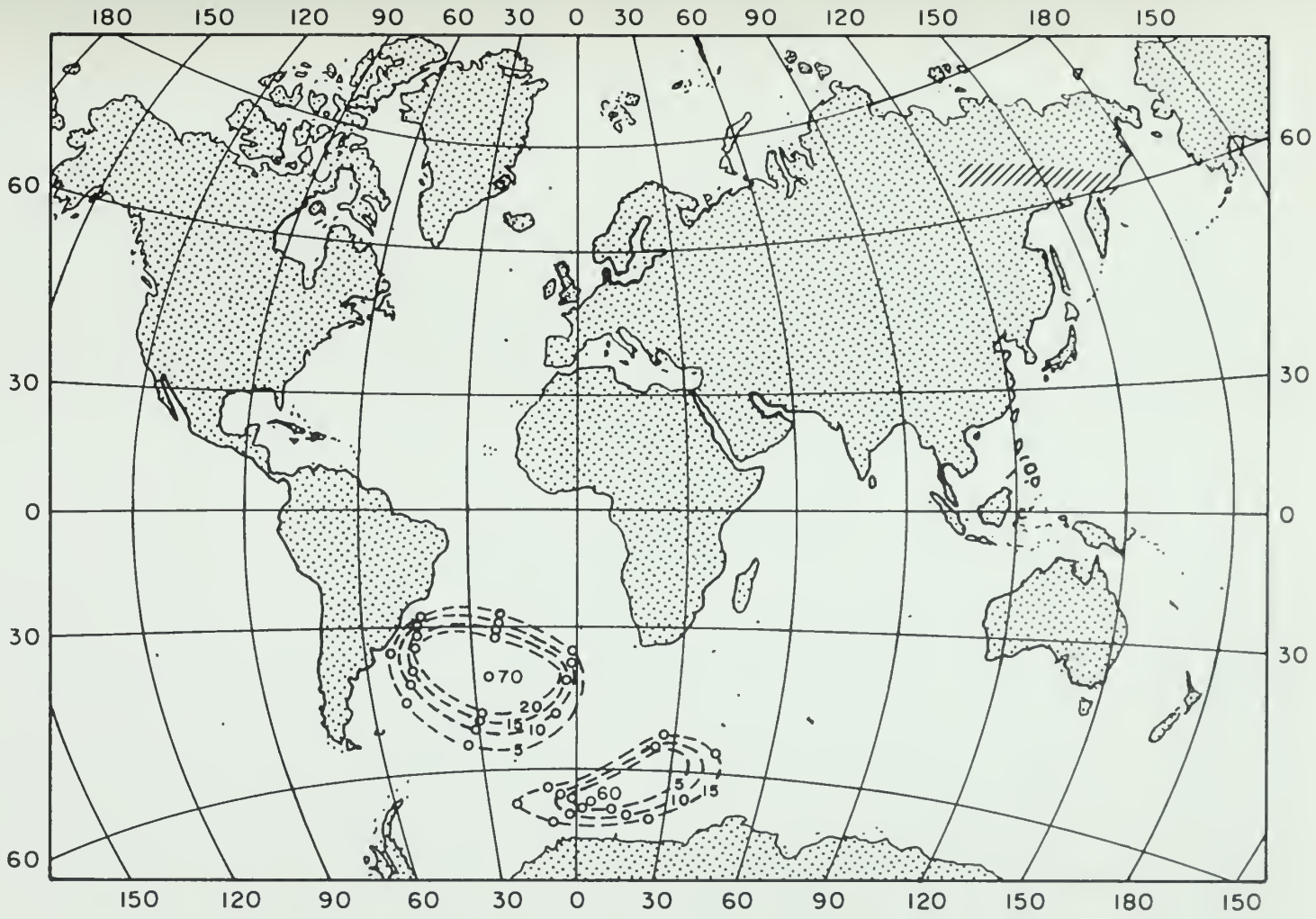

Figure 2. Projection Onto the Earth's Surface of Regions of Anomalous Radiation Intensity (After Kurnosova et al., ref. 5)

the Outer Radiation Zone or with the direct arrival on Earth of particles from the Sun. This latter hypothesis was suggested by the fact that the transient appearance of the Northern Anomaly was recorded immediately after the observance of intense chromospheric flares of intensity 2+.

Also in 1961, Seward conducted X-ray experiments on two satellites whose polar orbits completely covered the surface of Earth. The experiments were expected to give information of auroral zone radiation and other effects of particles trapped in the earth's magnetic field. Three regions of high counting rates in the guard detectors of the X-ray experiment were found during orbits between altitudes of about 160-550 km. These regions were (1) the northern polar zone, (2) the southern polar zone, and (3) a region over the South Atlantic Ocean stretching from South America to Africa. The guard detector system consisted of plastic phosphor fluors surrounding each X-ray detector. The guard fluors were shielded by an aluminum casing which absorbed electrons of energy below 2 Mev and protons of energy below 15 Mev. Two radiation anomalies over the South Atlantic, geographically correlated with those of Kurnosova, were evident. Concerning these anomalously high counts over the South Atlantic, Seward concluded they were probably due to particles trapped in Earth's magnetic field. (There is known to be an anomaly in the magnetic field over the South Atlantic.) This weakness in the field probably causes the mirror points of geomagnetically trapped radiation to be lower in this region. More definitive conjectures concerning the nature of the radiation were made by Seward (reference 6) after completion of data processing for the two aforementioned satellite flights. This report states it was probable that the South Atlantic Anomaly near Brazil contained trapped protons which were associated with the Inner Radiation Zone. The Southern Anomaly, on the other hand, probably contained geomagnetically trapped electrons. Refined particle counting-rate contours of Seward are shown in figure 3.

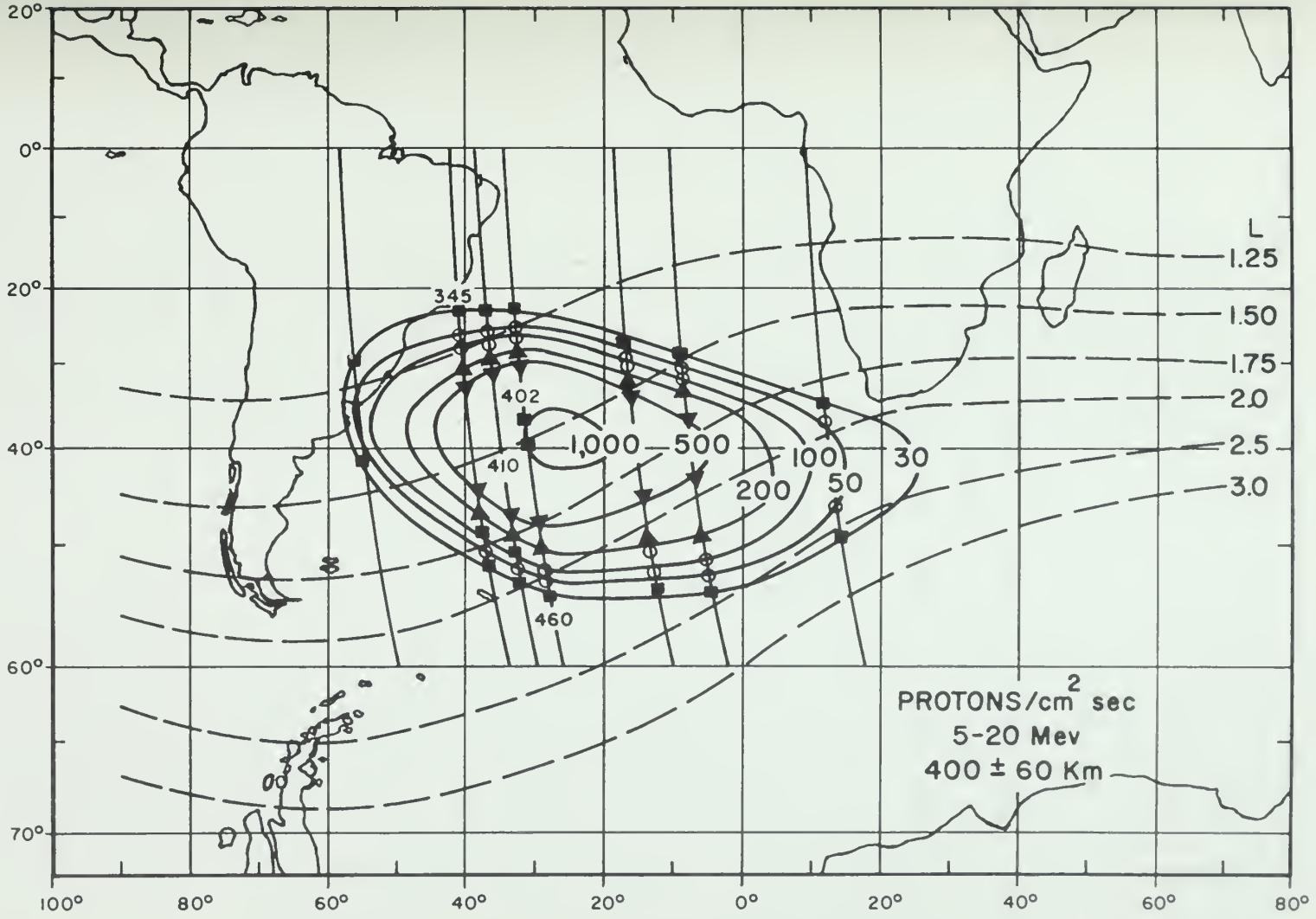

Figure 3. Projection Onto the Earth's Surface of Regions of Anomalous Radiation Intensity (After Seward and Kornblum, ref. 6)

In December 1962, Heckman and Nakano (reference 7) reported the visual detection of geomagnetically trapped protons in the region of the South Atlantic Magnetic Anomaly. Protons having kinetic energies of $\geq$57 Mev were recorded in electron-insensitive Ilford K.2 nuclear emulsions during a four-day, oriented satellite flight between altitudes of 178 and 407 km. Because more than 90 percent of all the particles recorded by the emulsions were located in a well-defined plane, they concluded that they had detected protons from the Inner Radiation Zone at and near their mirror planes (planes at which trapped particles are reflected). They further deduced a unique location for this mirroring region: 39 degrees S latitude, 41 degrees W longitude, a geographical location shown in figure 4. This mirroring region for protons coincides with the South Atlantic Radiation Anomaly independently reported by Kurnosova and Seward. Heckman and Nakano (using the "wobble" of magnetic declination and magnetic inclination) estimated roughly the size of the region in which the mirroring particles were detected: the shaded area in figure 4, delineated by the isogonic lines (8.6 and 13.6 deg) and the isoclinic lines (31.2 and 52.6 deg). Considering the directions from which the proton flux arrives, an east-west asymmetry was observed in the flux of geomagnetically trapped protons, confirming an effect predicted by Lenchek and Singer (reference 8). In addition, based upon 720 seconds of satellite flight time in the region of the anomaly, an omnidirectional flux of $N = 2.0 \pm 0.2 \times 10^4$ protons cm^{-2} Mev^{-1}, averaged over 60-70 Mev, was reported at an altitude of about 364 km. Based upon this flux, the peak counting rate, assuming Gaussian counting-rate contours, was about 15 cm^{-2} Mev^{-1} sec^{-1}, and the mean rate of detection for 65-Mev protons was about 12 cm^{-2} Mev^{-1} sec^{-1}.

In September and October of 1962, Freden and Paulikas (reference 9) measured the flux of protons from 5 to 20 Mev and 60 to 120 Mev on satellite flights at low altitudes over the South Atlantic Magnetic Anomaly. Their results indicated that the proton spectrum might turn back up below a local minimum near

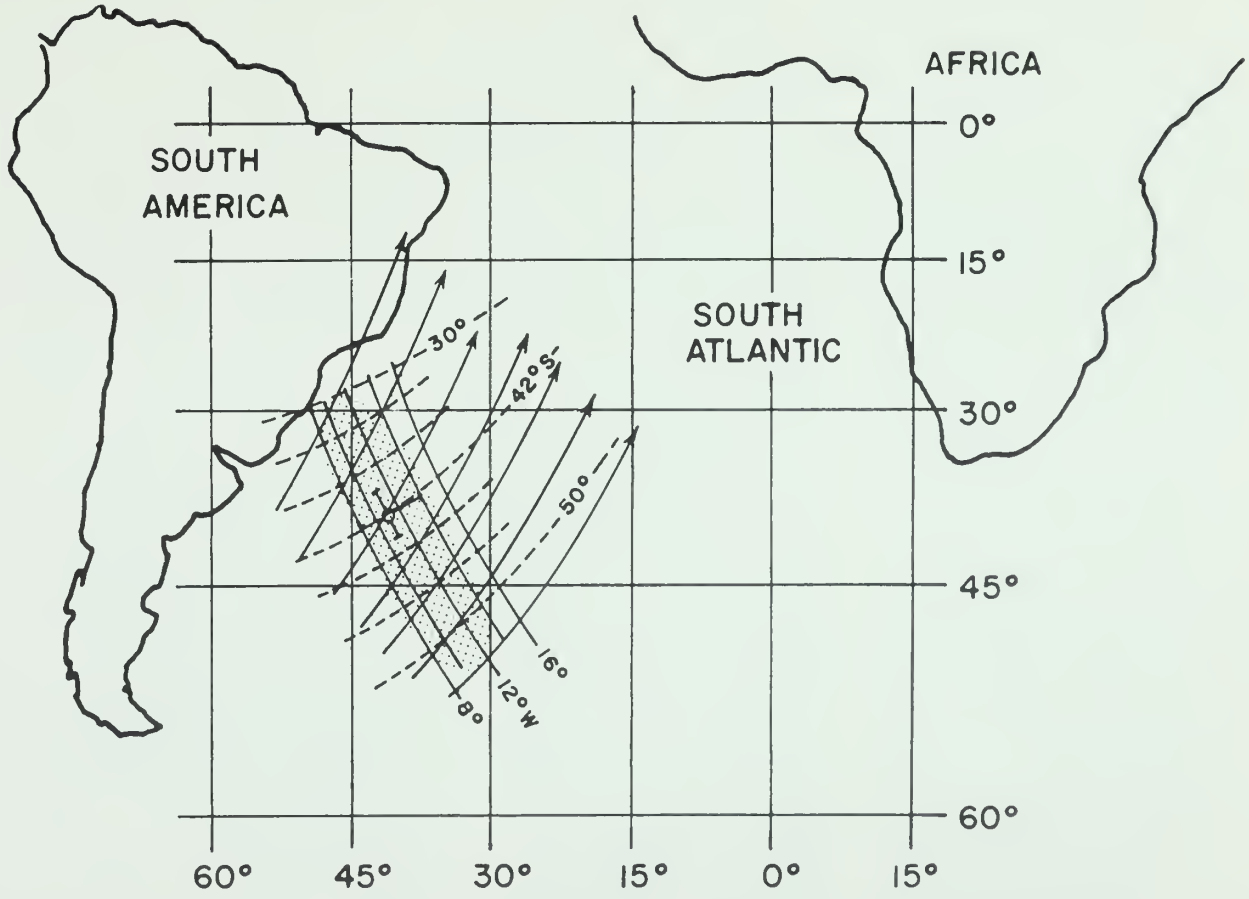

Figure 4. Projection Onto the Earth's Surface of Regions of Anomalous Mirroring-Proton Radiation (After Heckman and Nakano, ref. 7)

20 Mev. The need for additional experimental observations was evident.

b. Theoretical Observations

Dessler (reference 10) in 1959 pointed out that the existence of pronounced magnetic anomalies on the earth's surface can have a strong influence on the location of the radiation belts. Yoshida et al. (reference 11) expected that because of the magnetic anomaly, the boundary of the inner radiation belt over the South Atlantic would lie at considerably lower altitudes than in other regions.

Vernov et al. (reference 12) discussed the experimental evidence obtained by the second Soviet spacecraft-satellite and concluded that the enhanced radiation intensity found at an altitude of about 320 km above the Brazilian magnetic anomaly is due to the inner radiation belt. Because, without the magnetic anomaly, the mirror points are higher at comparable points north of the geomagnetic equator, a similar conjugate radiation anomaly is not observed in the northern hemisphere.

Gledhill and Van Rooyen (reference 13) point out that the Southern Radiation Anomaly lying between Cape Town and Antarctica can be attributed to the Outer Radiation Zone, and the South Atlantic Radiation Anomaly can be attributed to the Inner Radiation Zone. These interpretations were supported by the observation that the belts of particles caused by nuclear detonations lie in the region between the two anomalous radiation regions. Using longitudinal integral-invariant curves published by Vestine and Sibley (reference 14), Gledhill and Van Rooyen estimated the traces on Earth's surface of the mirror points of particles entering the Southern Radiation Anomaly as observed by the Soviet's second spacecraft-satellite. These traces are shown in figure 5. Because of these conjugate traces, Gledhill conjectures that data on electron flux obtained by O'Brien et al. (references 15 and 16) at altitudes of 1000 km over Iowa City (point C in figure 5), can

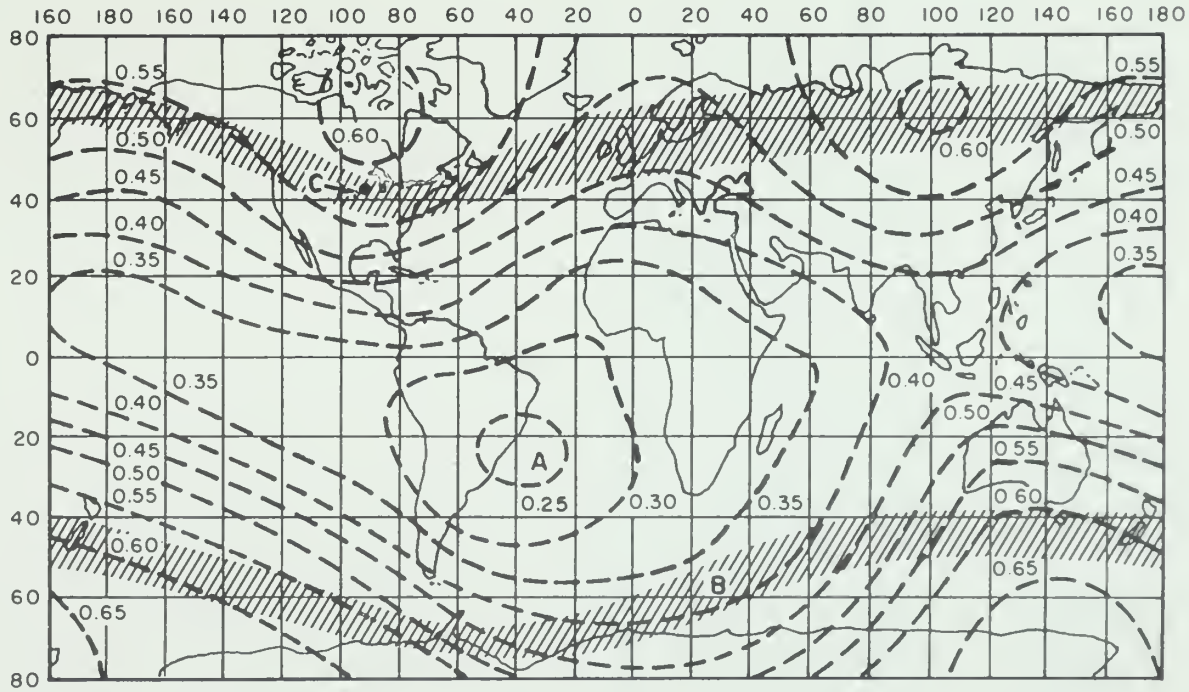

Figure 5. Traces on the Earth's Furface of Particles Entering the Southern Radiation Anomaly (After Gledhill and Van Rooyen, ref. 13)

be used as a reasonable sample of properties of electrons entering the Southern Radiation Anomaly. These properties include an energy flux characterized by 100 ergs cm^{-2} sec^{-1}, about 90 percent of which is carried by electrons in the energy range 1 to 40 kev. They conjecture that this particle flux into the Southern Radiation Anomaly is probably large enough to produce observable auroral effects and they announce such auroral investigations are being undertaken.

Understanding and theoretical description of near-Earth radiation anomalies is incomplete at this time. Yet these anomalies must be explored and new data obtained before theories about injection mechanisms for geomagnetically trapped radiation can be accepted unambiguously. Specifically, an important unanswered question in current space research is "What is the exact nature and origin of the radiations in the radiation anomalies over the southern hemisphere?"

SECTION II

THE EXPERIMENT

1. Techniques Considered

Insofar as investigations to date had not determined fully the nature of radiations in space near Earth, particularly in the high-flux regions over the South Atlantic, it was decided in August 1962 that further investigations to obtain information on the location, time dependence, composition, intensity, and energy spectra of these radiations were warranted.

Generally such investigations may be conducted by either of two experimental techniques, which may be loosely categorized according to the type of detector response utilized:

a. Permanent-response techniques. Examples of this technique are the use of emulsion films or radiation dosimeters which undergo a permanent physical change after exposure to certain radiations. A characteristic of this technique is the requirement that the detector must be recovered before data processing.

b. Transient-response techniques. Examples of this technique are the use of scintillation detectors or solid-state detectors which respond to radiations by generating a transient signal, such as light or electrical currents, and which after a certain dead time of the order of microseconds return to their initial conditions. A characteristic of this technique is that detector responses can be externally recorded, and hence recovery of the detectors is not required. The recorded responses, naturally, must be obtained before data processing. In space experiments, this recovery is usually accomplished by telemetering the response data to ground stations by a radio-frequency telemetry link.

One proven approach to measuring radiations accurately positioned in space with permanent-response techniques is to use emulsion films. This technique was investigated briefly. Such an approach involves the programmed exposure of segments of film

to radiation through a collimated entrance channel of a heavily shielded film receptacle. The programming is used to correlate the time of exposure of each segment with the flight ephemeris, i.e., the spatial location of the satellite. Since definitive information on protons with energies principally below 60 Mev was desired for more complete knowledge of the energy spectrum, the method of Heckman discussed in section I is not appropriate. Instead, more sensitive emulsion films must be used. One major obstacle of this approach for sustained space flight is the large amount of material needed to shield the film segments properly, both before and after programmed exposures. This shielding material can possibly weigh over 20 pounds. Without adequate shielding material, a high flux of energetic radiation not only fogs the exposed film segment but partially exposes the other film segments. This unprogrammed partial exposure to radiations completely invalidates correlation of film segments with the flight ephemeris.

Although the above approach appeared feasible, it could properly be undertaken only by a research group which was well equipped for emulsion studies. Because of this primary consideration, and others that follow, it was decided to pursue the investigation using transient-response techniques. This decision was made in the belief that more data could be obtained more cheaply and quickly, more reliably, from a successful space flight using transient-response techniques than any other techniques investigated. Reasons for this belief included the following:

a. The availability of payload space for recoverable experiments was severely limited in satellite vehicles that passed through the geographical areas of interest. The required weight of shielding material for an emulsion-technique experiment made flight scheduling difficult, if not impossible, in current experimental programs.

b. The emulsion-film technique was limited to obtaining data from very few orbits (perhaps less than one) because of mechanical complications present in programming exposures with a film receptacle of "minimal" weight.

c. Research facilities to fabricate and interpret experiments using transient-response techniques were more readily available than those for permanent-response techniques.

d. Transient-response techniques presented many challenging technical and scientific problems to an experimenter. Solution of any of these problems would provide improved experimental methods for space investigations.

e. Transient-response techniques provided greater flexibility in matching the experiment to available space flights, including probes, than if payload recovery was required.

2. Design Considerations

In designing the experiment so as to use transient-response techniques, first attention was given to the basic concepts shown in figure 6, which is a simplified schematic of the initial logic for the experiment.

It was decided that three detectors would be necessary and sufficient to achieve the major goals of the investigation as regards measurements of charged-particle radiation (protons and electrons). Detector 1 would be used primarily to measure the differential deposit of energy, dE/dx, of particles that activated it. Detector 2 would be used primarily to measure the total energy, E, of the particle. These two measurements are sufficient to identify type and energy of the particle. Detector 3 would be used to limit the range of angles of the path of the particle being analyzed in Detectors 1 and 2. Briefly stated, it was planned to use three detectors to constitute a directional radiation telescope.

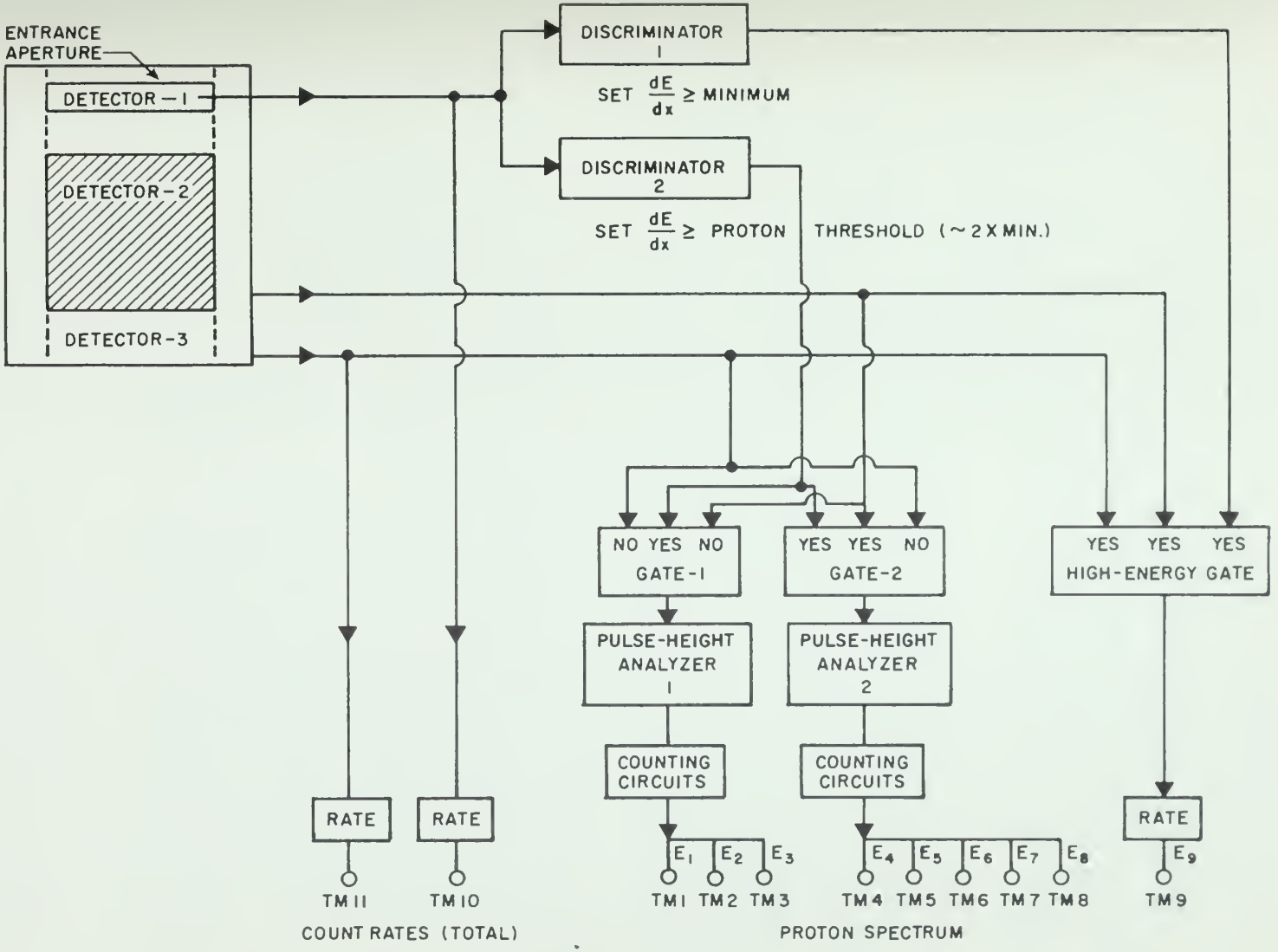

Figure 6. Initial Concepts of the Experiment

The interpretation of the responses from these detectors depends on the logic used. This logic is outlined in figure 6. The directional telescope consists of two in-line detectors, Detectors 1 and 2, which are partially surrounded by a "guard" detector, Detector 3. Detector 3 responds to particles with out-of-line trajectories. Electronic circuitry will receive the outputs of the detectors and furnish inputs to telemetry according to the following concepts:

a. In-line protons with energy between $E_{p\ threshold}$ and $E_{p\ high}$ will register a dE/dx response in Detector 1 greater than the chosen proton threshold. Of these protons, many will enter Detector 2 and be totally absorbed. Thus if there occurs a pulse of greater than proton threshold in Detector 1 in coincidence with a pulse in Detector 2 and not accompanied by a pulse from Detector 3, then the coincidence circuitry permits the pulse from Detector 2 to be analyzed and recorded in telemetry channels TM1 through TM8.

b. In-line protons with excessively high energy will register a dE/dx of less than proton threshold in Detector 1, yet above minimum response. They will then pass through Detector 2 and out of the telescope through Detector 3. Assuming a certain minimum energy is deposited in Detector 1 and Detector 2, this threefold coincidence can be recorded in telemetry channel TM9 as a high-energy particle. (This logic appears most favorable for accurately registering high-energy particles. However, because of light-collection problems, it was found necessary to use another method to count high-energy particles without obtaining the threefold coincidence. This change will be discussed in a later subsection.)

c. In-line electrons of appropriate energies will register a small dE/dx response below proton threshold yet above minimum response in Detector 1 and will be stopped in Detector 2 without entering Detector 3. The resulting pulse combination can be registered in telemetry channel TM10.

d. Total counting rates of Detector 3 can be recorded, if desired, in telemetry channel TM11.

Using these concepts, implementation of the experiment consisted primarily of selecting appropriate components for the telescope and designing the electronic subsystems. These areas will be covered in the subsection that follows.

In designing the experiment, primary consideration was given to (a) the telescope, (b) electronic circuitry, and (c) power supply and voltage regulation.

a. The Telescope

Primary goal in design of the telescope was to choose radiation detection devices which had suitable transient responses. Three detectors and ancillary signal collecting systems were selected.

(1) Detector 1. Since Detector 1 was to furnish dE/dx measurements without absorbing excessive energy from the particle, the choice was narrowed to either a thin wafer of scintillation material viewed by a photomultiplier tube, or a thin solid-state detector used with a stable high-gain, low-noise amplifier system. Either system could perform the desired function of identifying the type of particle registered by the telescope.

A solid-state detector was chosen as Detector 1 in view of the following considerations:

(a) Solid-state detectors require minimum volume, weight, and power, distinct advantages in space flight applications.

(b) These detectors can provide relatively large active areas (~3 cm^2) with reasonable depletion layers (~400 microns), yet with negligible dead layers (loss of ~50 kev).

(c) Solid-state detectors permit pulse-height analysis of entering protons at lower energies. This advantage occurs since it is relatively simple to analyze the linear signal output from a solid-state detector for low-energy protons between

threshold and its total stopping power (~7.5 Mev). Because of the probable nonlinearity and poor collection of light from a thin wafer of scintillation material, it would not be as simple to pulse-height-analyze protons with a thin wafer of scintillation material and a photomultiplier tube mounted external to the guard detector. This advantage is gained without sacrificing the energy range covered by Detector 2, because both types of detector wafers possessed comparable absorption properties.

(d) Thin wafers of scintillation material, if viewed by a photomultiplier tube, although feasible, would complicate the physical construction and design geometry of the telescope.

(2) Detector 2. Since Detector 2 was to furnish total E measurements on particles of interest, it was important that this detector possess a large dynamic range of stopping power. This requirement suggested that it would be advantageous to use an inorganic scintillator of high atomic mass which provides large stopping power and a linear output response in a reasonably short crystal.

A crystal of thallium-activated cesium iodide, CsI(Tℓ), was chosen for Detector 2 in view of the following considerations:

(a) The scintillation characteristics of CsI(Tℓ) were suitable. These characteristics are shown in figure 7.

(b) Because of its high density, a cylindrical CsI(Tℓ) crystal of only 1.5-inch length would be sufficient to completely absorb protons of incident energy up to approximately 110 Mev. Other scintillators of lower atomic mass require longer path lengths to absorb this same energy range. (Longer paths were a distinct disadvantage in this experiment since they would decrease the effective solid angle and increase the problems of light collection.)

(c) Cesium iodide crystals were easily available and required only minor machine work to fit them for the telescope.

DECAY CONSTANT	1.2 MICROSECONDS
PULSE HEIGHT	0.4 NAI (TI)
PROPORTIONALITY	EXCELLENT
DENSITY	4.51 G/CC
RELATIVE ATTENUATION COEFFICIENT	1.5 NAI (TI)
STABILITY IN AIR	GOOD

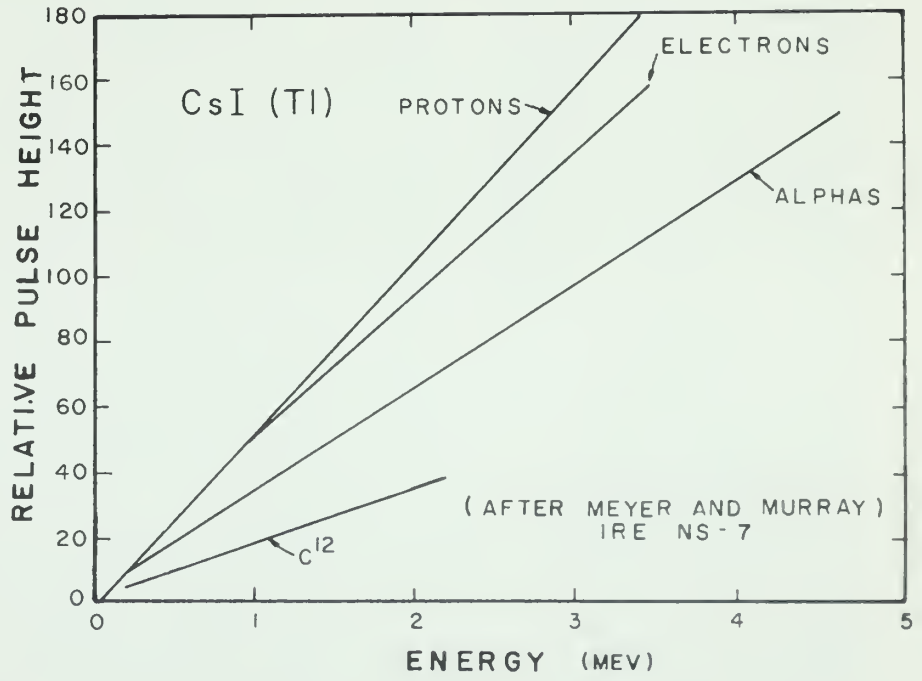

Figure 7. Scintillation Characteristics of Cesium Iodide (After Meyer and Murray, ref. 17)

Since the CsI(Tℓ) crystal would be positioned within the guard detector, it would be necessary to pierce Detector 3 with a lightpipe to collect the light from Detector 2 for analysis. After experimentally investigating various schemes for lightpipe arrangements, it was decided to pierce the guard detector along the telescope axis and to directly view the CsI(Tℓ) crystal from the rear through a cylindrical lucite lightpipe. This arrangement was chosen for the following reasons:

(a) It provided the best energy resolution of all light-collection schemes investigated.

(b) The logic of the experiment was least affected by removal of guard-detector material along the telescope axis. Furthermore, one can compensate for high-energy particles which completely transit the telescope along its "unguarded" axis by the following change in original logic: Since, with the light-pipe for Detector 2 in place, axial high-energy particles do not activate Detector 3, the requirement for a coincidence among Detectors 1, 2, and 3 as shown in figure 6 must be changed. The revised coincidence requirements are shown in figure 8. They are a minimal response of less than proton threshold in Detector 1, an energy deposit of over a certain minimum (48 Mev) in Detector 2, and no pulse in Detector 3. This change in logic does not affect the ability of the telescope to reject low-energy particles entering through the "rear window" since they will be totally absorbed by the CsI(Tℓ) crystal without coincidence signals from Detector 1. However, high-energy particles entering through the rear window might completely transit the telescope incorrectly in the reverse direction. Actually the logic of the experiment is still valid since these reverse-track protons have a negligible effect. Because protons traveling in either direction with $E_p >$ 200 Mev will not deposit over 48 Mev in Detector 2, no erroneous high-energy counts are introduced in telemetry channel TM9 for reverse-track protons with $E_p > 200$ Mev. For protons which transit the telescope in reverse with 110 Mev$< E_{pr} <$200 Mev, even though

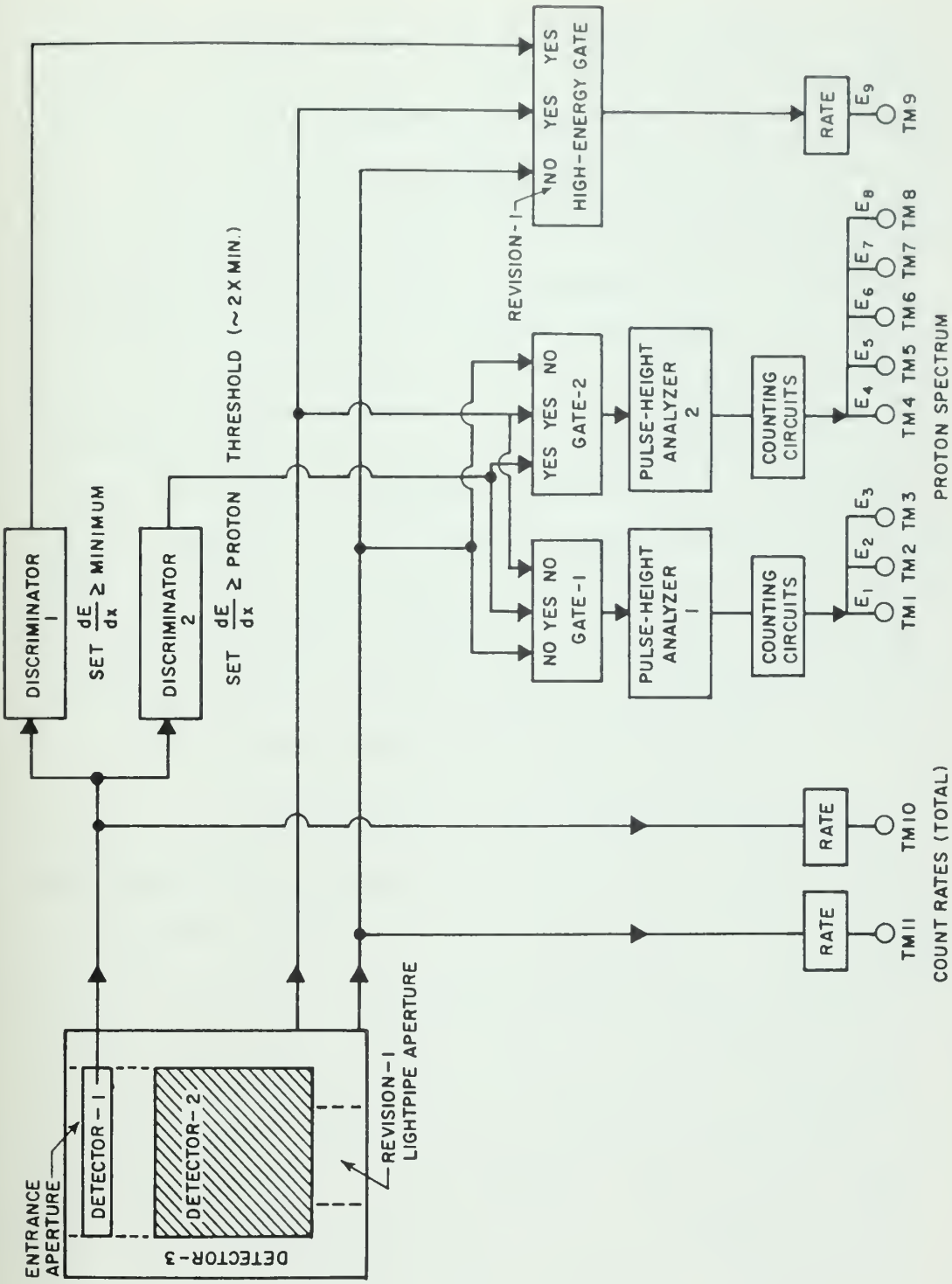

Figure 8. Revised Logic Necessitated by the Lightpipe of Detector 3

the required deposit of over 48 Mev is made in Detector 2, the deposit in Detector 1 will be greater than 550 kev. Hence these particles will not be registered incorrectly in telemetry channel TM9. Unfortunately some of these reverse-track protons will fulfill the requirements for being registered incorrectly as protons with energies supposedly between ~48 and 110 Mev. By choice of energy channels, however, all these improper counts can be made to register in one channel, telemetry channel TM8. This channel will then indicate the sum of the correct-path protons with 48 Mev$<E_p<$110 Mev plus reverse-track protons of 110$<E_{pr}<$200 Mev. Nevertheless, since the correct-path proton events with 110$<E_p<$ 200 Mev are counted in telemetry channel TM9, it is relatively easy to compensate for the incorrect, reverse-track protons registered in telemetry channel TM8. In addition, the proton spectrum was expected to decrease rapidly in a steep, nearly logarithmic decline as the energy increases. Hence the compensating corrections necessary to unfold the effects of reverse-track protons in telemetry channel TM8 should be relatively small.

It should be noted that perhaps a better light-collection system for Detector 2 is obtainable. In particular, experimental investigations were conducted concerning the use of a solid-state photodiode to collect light from the CsI(Tℓ) crystal in a manner reported by Tuzzolino (reference 18). In the Tuzzolino method a large-area solid-state photodiode would be optically coupled to the CsI(Tℓ) crystal (say at its rear surface), and the guard detector pierced only by a small wire to extract the electrical signal response of the solid-state photodiode for pulse-height analysis. This arrangement would avoid the light-collection problems discussed above, and advantageously reduce the requirements of space, weight, and power for the telescope. Although this method appears desirable from many viewpoints, nevertheless it possesses a serious limitation in that the photodiode responds suitably only to energy deposits in CsI(Tℓ) of over ~50 Mev. Insofar as the energy spectrum below 50 Mev was

considered important to this investigation, it was decided not to use a solid-state photodiode but rather to accept the minor limitations imposed by use of a photomultiplier tube and the axial light-collection system discussed previously.

(3) Detector 3. Because Detector 3 was to be used primarily as a guard detector to limit the range of angles of particle paths in the telescope, it was necessary to select a detector which would have the following characteristics:

(a) Be of quick response to radiations of interest, thereby facilitating use of its signal to block unwanted signals from registering;

(b) Be easily machinable, yet possess structural strength, thereby facilitating fabrication of a custom-fitted guard detector to surround and support Detectors 1 and 2;

(c) Be of relatively low-Z material, thereby gaining two advantages:

1. Reduction of bremsstrahlung radiations produced in the guard detector to minimize background radiations in high-flux regions that might occasionally saturate Detector 2.

2. Reduction of weight in the guard detector, the volume of which would be large.

Because of these requirements, a plastic phosphor scintillator was chosen for Detector 3.

A light-collection system would be necessary to extract signals from this plastic scintillator. A photomultiplier tube, optically coupled to Detector 3 by means of a lucite light-pipe, could be used to view the plastic scintillator from the side at a right angle to the telescope axis. The following reasons governed choice of location for the lightpipe:

(a) Since it was already planned to pierce the rear face of the guard detector to accommodate the lightpipe for Detector 2, the side location was most nearly symmetric with

respect to the remaining detector material. This symmetry would enhance the probability of collecting light of low intensity from most regions of the plastic scintillator.

(b) This location would facilitate fabrication of the telescope since it was the simplest light-collection geometry compatible with the experiment.

General light-collection problems for the complete telescope included protecting the three detectors and both collection systems against extraneous light. In addition, protection should be provided to prevent internal light leaks between separate detectors.

To protect solid-state Detector 1 from extraneous light, it was decided to sandwich it between two thin opaque diaphragms, each formed by a sheet of 0.25-mil mylar with a highly reflective, aluminized coating on each side.

To protect Detector 2 from extraneous light and to aid internal reflectivity, the cylindrical sides of the CsI(Tℓ) crystal were coated with highly reflective white paint. The front face of the CsI(Tℓ) crystal would be machined clean because it is undesirable to have particle-absorptive materials, such as a variable coating of white paint, in the entrance path of the telescope. The light loss through the front face of Detector 2 would be partially compensated by light reflected from the lower aluminized diaphragm of Detector 1, which was ~0.25 inch from the front face of Detector 2. This diaphragm in combination with the reflective white-painted sides would reflect a large percentage of light signals generated in Detector 2 through the machined-clean bottom face of the CsI(Tℓ) crystal into an optically coupled lightpipe and photomultiplier tube.

To protect the plastic scintillator, Detector 3, from extraneous light and to aid internal reflectivity, all surface areas except the side area that formed the optical junction to its lightpipe would be coated with highly reflective white paint. To add further protection, and to isolate the guard detector optically,

it was decided to use an inner support liner of very thin, machined aluminum (~17 mils). This liner would serve the dual purpose of an opaque interface between detectors and a structural support to hold the inner components of the telescope. The presence of this inner liner, because of its absorption characteristics, must be considered when determining the theoretical energy resolution of the telescope. This consideration is important in calculating limits of error for energy spectra obtained in the experiment.

(4) Inflight Calibration. A question which was of interest in designing the telescope concerned the use of radioactive inflight-calibration sources. Arguments for using such sources, mounted within the telescope adjacent to the detectors, include the following:

(a) Preliminary system checks require frequent use of radioactive sources. Such checks are necessary to accumulate consistent information needed in analyzing system operation. Because the sources are used frequently, they should be mounted permanently rather than risk component damage by repeated dismantling of the telescope. When properly chosen, the sources provide a convenient and necessary reference standard to check the accuracy of operation of a detector channel.

(b) Suitable locations and a mounting technique were available for use with Detectors 1 and 2. (The best location appeared to be on the mylar diaphragms; the technique considered would be to deposit a radioactive source material (Americium 241) in droplets, which would be evaporated to leave a radioactive residue. If changes to the source were necessary, they could be easily accomplished by exchanging diaphragms.) Detectors 1 and 2 are the two detectors of primary interest since they provide signals for pulse-height analysis. They should be checked for stability of system gain, before and during an experiment. Use of radioactive deposits on the removable mylar diaphragms would not permanently contaminate any other component.

Despite some admitted complications, actually very minor in the overall design of the experiment, it was decided to use evaporated droplets of Am^{241} in HCℓ deposited on the two mylar diaphragms. Each of these deposits would provide a low-activity flux (less than 100 counts detected per second) of nearly monoenergetic 5.5-Mev alpha particles.

A change in the functional concepts of the experiment was dictated by use of an inflight-calibration source with Detector 2. The response of Detector 2 to the alpha flux which activates its lowest channel must be registered in a telemetry channel other than the normal output channel, TM4. This change was necessary because of the following reasons:

(a) No pulse in Detector 1 is coincident with the pulses from the alpha particles to permit registering them in output channel TM4.

(b) The alpha flux necessary for a satisfactory inflight check is comparable to, and for a great percentage of flight time will actually exceed, the flux expected to be registered in the lowest energy channel of Detector 2. (This was also true for every energy-dependent channel including those of Detector 1.)

Assuming no extra telemetry channels would be available for inflight checks, only two telemetry channels remain for consideration, TM10 and TM11. These channels provide total counting rates of Detectors 1 and 3. It was decided to couple Detector 2 directly into the total counting-rate channel for Detector 1, TM10. This choice was made in view of the following considerations:

(a) A large percentage of the proton flux that activated Detector 1 would also be pulse-height analyzed and recorded in the other nine energy-dependent channels. Hence, it should be possible to unfold the effect of the additional counting rate coupled into TM10 by Detector 2.

(b) The comparative counting rates due to the alpha source acting on Detector 2 and flux measurements expected in Detector 1 could be set so that in low flux areas the counting rate of Detector 1 would be sufficiently low that the counting-rate output of TM10 would be due almost entirely to Detector 2. These low flux regions would therefore provide an inflight check of the accurate operation of the CsI(Tℓ) detector channel. Conversely, in expected regions of high flux (such as the anomalies over the South Atlantic), the counting rate of Detector 1 would be effectively greater (by an order of magnitude) than the counting rate due to the alpha source acting in Detector 2. Hence, little confusion should ensue concerning the true counting rate of Detector 1.

(c) Because of the large surface area of Detector 3, it was not certain that its counting rate, even in low flux regions, would fall sufficiently low to permit analysis of a composite counting rate into the separate contributions from Detector 2 or Detector 3. This uncertainty could not be removed by increasing significantly the activity of the alpha sources without introducing certain disadvantageous effects into the energy-dependent channels of Detector 1. These effects will be discussed in a later paragraph which considers the distribution of pulses from alpha particles in Detector 1.

It should be noted that in the above arrangement, which effectively combined the total counting rates of Detectors 1 and 2 in telemetry channel TM10, particles which activated both Detectors 1 and 2 need not be registered twice. An undesired double count should be prevented by suitable electronic circuitry. Specifically, the nearly simultaneous pulses from Detectors 1 and 2 were stretched and shaped so that they overlapped in time. The count-rate meter circuitry responded to the application of the two overlapping pulses in a manner not significantly different than the manner in which it responded to either of them individually. Hence the noncoincident counting rate of Detector 2 was

added algebraically to the counting rate of Detector 1 in telemetry channel TM10, but no double counting occurred from particles that activated both Detectors 1 and 2 simultaneously. Nevertheless, any flux of particles that activates Detector 2 and not Detector 1 will be registered in the composite counting-rate channel. This flux would include particles that enter Detector 2 through Detector 3 or the axial lightpipe window. However, since the counting rate of these particles is expected to be highly energy-dependent, only relatively few particles would be able to penetrate through the casing of the telescope (~1/4 inch of aluminum) and Detector 3 (~1/2 inch of plastic fluor material). Such high-energy particles will complicate unfolding the individual total counting rates of Detectors 1 and 2. This complication was considered however to be a reasonable price to pay for the advantage of inflight checks on the system operation of Detector 2.

No change in the functional concepts of the experiment was necessary for the use of an inflight-calibration source with Detector 1. The net effect, as regards Detector 1, due to the deposit of the two alpha sources on the mylar diaphragms was that Detector 1 would be activated by two different energy distributions of alpha particles. The separation in energy of the two distributions of alpha particles results from the fact that alpha particles emitted from the radioactive deposit on the far side of the rear mylar diaphragm are degraded in energy by about 1 Mev in passing through the ~1 mg/cm^2 of aluminum on the mylar diaphragm before entering Detector 1 from the rear. Advantage was taken of this situation, however, by including both the lower distribution from the rear source (peaking at ~4.5 Mev) and the higher distribution from the front source (peaking at ~5.5 Mev) in the middle channel, TM2, of the three energy-dependent telemetry channels from Detector 1. Thus a shift of system gain, either up or down, would be noticed in low-flux regions by a significant shift of the alpha particle counts into either the lower or the upper channel, TM1 or TM3.

It should be noted that if the intensity of the inflight-calibration sources is increased significantly, then it would no longer be possible to include all counts of the two distributions conveniently in a single center channel. Especially is this true if the intensity of the rear source, primarily used to check Detector 2, were increased. The spreading out of the distribution due to absorption in noncollimated paths through the rear aluminized mylar diaphragm would place many counts in the lowest energy channel,TM1. An increased intensity would also be more critically detrimental since, in expected regions of high flux, none of the three energy-dependent channels of Detector 1 were expected to register flux greater than ~500 counts per second with an uncertainty factor of 2 or more. The presence of source counts of comparable strength in these channels would nullify the intended use of the channel. It was therefore necessary to use radioactive sources giving rise to only about 50 counts detected per second in each direction for the rear source, Source 2, and about 25 counts detected per second in each direction for the front source, Source 1. This choice would produce approximately 50 counts detected per second in Detector 2 due to Source 2 (none from Source 1 due to total absorption of the alpha particles by intervening materials) and approximately 75 counts detected per second in the center energy channel (TM2) of Detector 1 (50 counts from Source 2, 25 from Source 1).

(5) Summary

To recapitulate, the major points discussed in this subsection on the telescope include the design considerations used in selecting

(a) The transient-response detectors:

A solid-state detector for Detector 1 (dE/dx).

A cesium iodide detector for Detector 2 (E).

A plastic phosphor detector for Detector 3 (guard fluor).

(b) The signal coupling systems for the detectors:

A stable high-gain, low-noise amplifier for Detector 1.

An optically coupled lucite lightpipe mounted axially on the rear face of the CsI(Tℓ) crystal of Detector 2.

An optically coupled lucite lightpipe mounted at a right angle to the telescope axis on the cylindrical side of Detector 3.

(c) Evaporated droplets of Am^{241} in HCℓ deposited on two aluminized mylar diaphragms as alpha-radioactive, inflight-calibration sources. Minor changes in the functional concepts were made to accommodate a composite counting-rate channel for Detectors 1 and 2. These changes are shown in figure 9, a diagram of the final concepts of the experiment.

(d) Certain light-protection, internal-reflection, and detector-isolation techniques. These selections are portrayed graphically in figure 10, an isometric diagram of the telescope.

b. Electronic Circuitry

The primary goal for the design of electronic circuitry was to process the signal responses of the telescope according to the final functional concepts (figure 9), so as to provide suitable electrical outputs for use with a telemetry system. The telemetry system was expected to require positive input signals ranging from zero to five volts d.c. Weight requirements for space applications dictated use of transistors and miniaturized components throughout the system.

Since the signal responses from Detectors 2 and 3 were light scintillations, these responses were converted to electrical signals by optically coupled photomultiplier tubes which viewed their respective lightpipes. RCA type 6649 photomultiplier tubes were chosen to view both detectors because they were of the appropriate size, possessed the necessary operating characteristics,

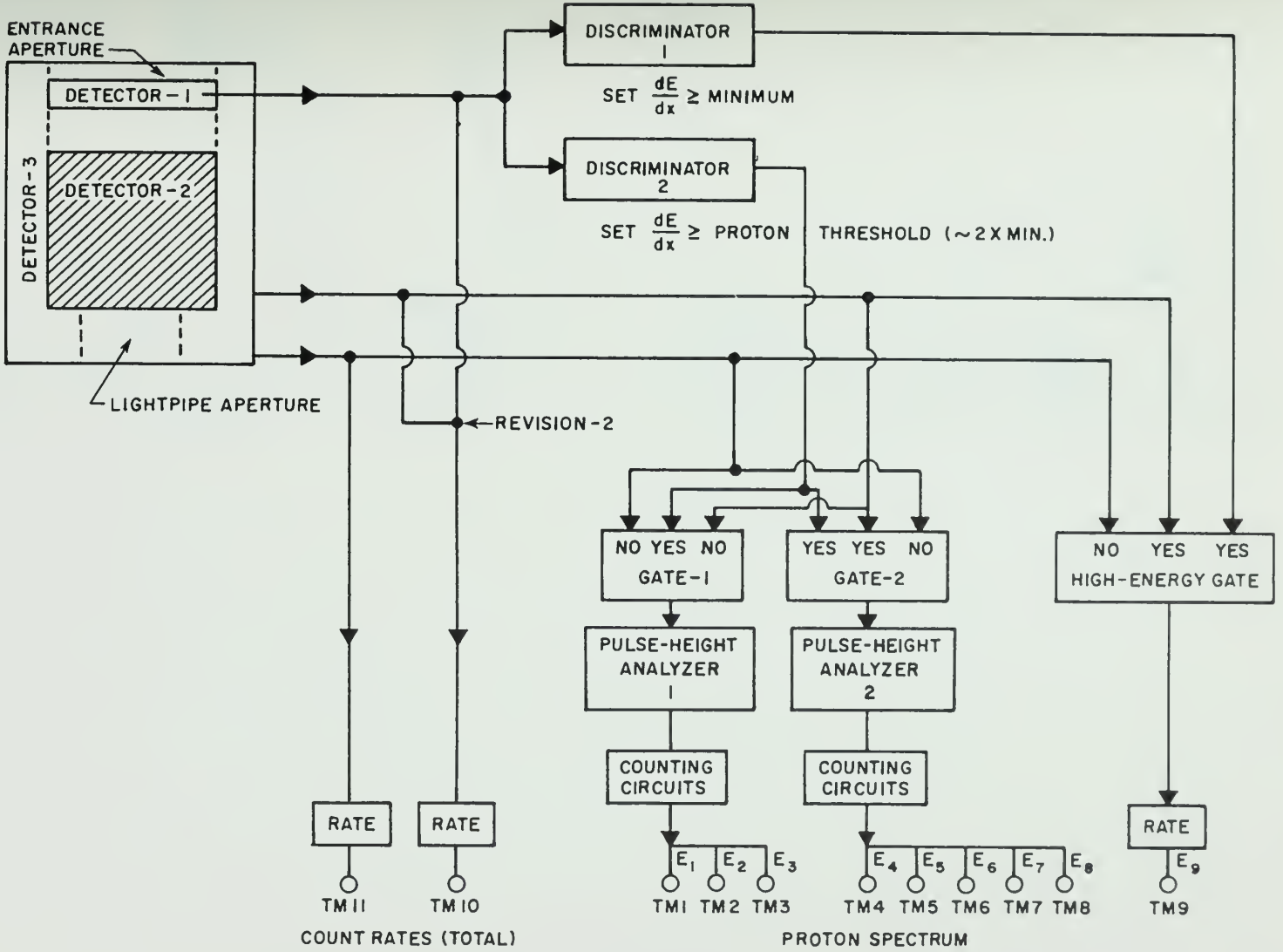

Figure 9. Final Concepts of the Experiment

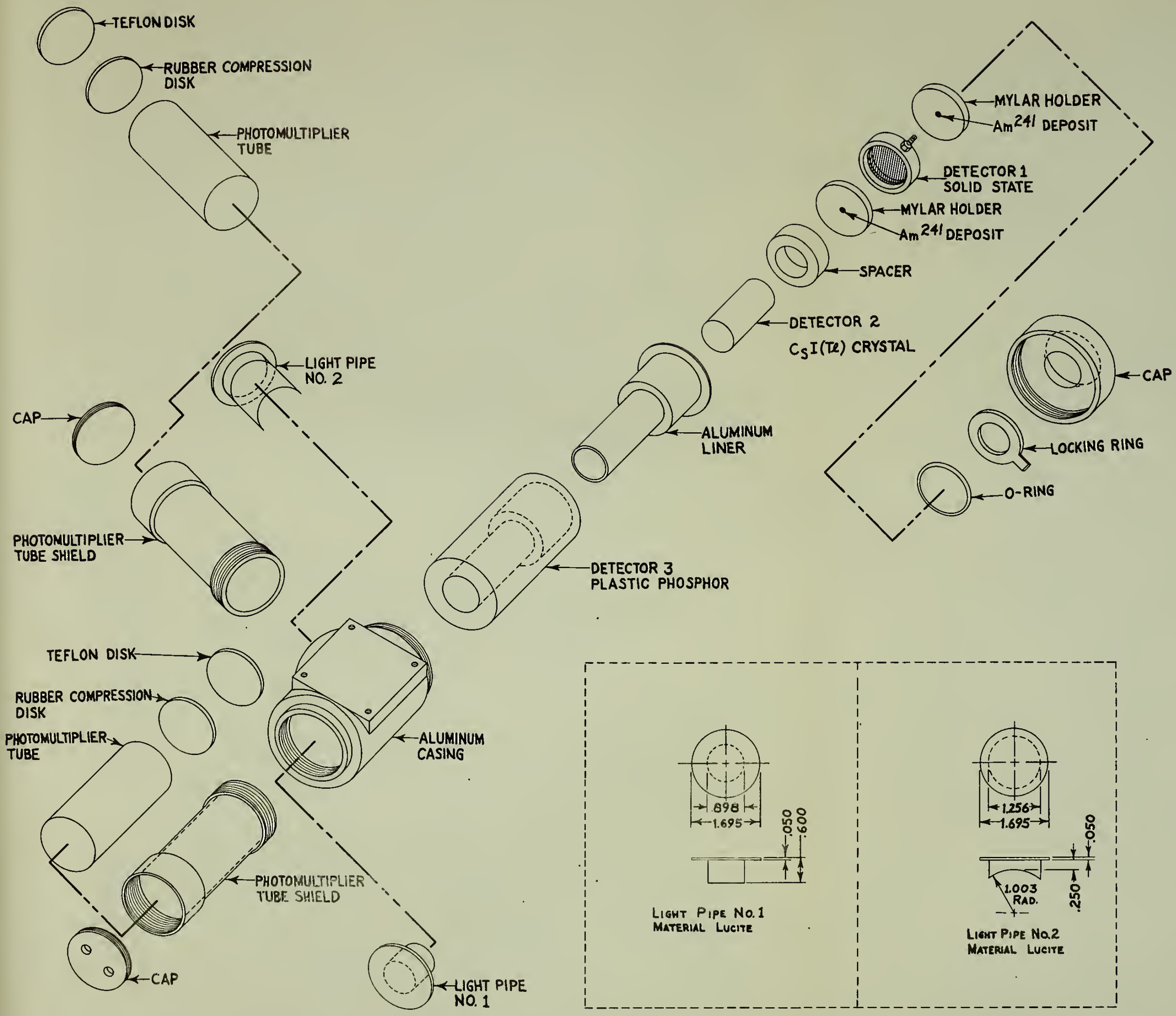

Figure 10. The Telescope (Isometric View)

and were of a ruggedized construction suitable for space flight. The tube-base circuitry used for these photomultiplier tubes provided output pulses suitable for pulse-height analysis. This circuitry is shown in figure 11. The relatively low (10 kohms) anode load resistor, R1, was chosen so that the response of the photomultiplier was not integrated excessively. This ensured that the output pulse of the photomultiplier reached its peak in a short time, and was of short duration. With this circuitry, the pulse reached peak value in under 0.5 microsecond and fell to less than 10 percent of peak value in under 3 microseconds. Both of these pulse-shape factors, which affect resolution and dead time for the system, were advantageous to signal processing in coincidence circuitry and pulse-height analyzer circuitry. The resultant low amplification in the output signal of the photomultiplier tube due to the low anode load resistor could be easily compensated for by use of additional signal amplification. The same tube-base circuitry was used for both Detectors 2 and 3. Thus, besides the advantage of simplicity in fabrication, interchangeability of photomultiplier tubes was possible even after permanent potting of tube-base circuitry. The tube-base circuitry also provided that a high-beta transistor, operated at positive 20 volts d.c. collector voltage, be used as an emitter follower to decouple the photomultiplier tube from its signal output. This transistor was physically located in an insulated well in the base potting of the photomultiplier. This arrangement minimized extraneous noise fluctuations caused by long, high-voltage photomultiplier signal leads; yet it did not introduce signal distortion. The range of signal strengths at the output of the emitter follower which were to be used for pulse-height analysis were expected to extend from 70 millivolts to 4 volts (negative peak of signal pulse).

Amplification for these signals was necessary to provide the appropriate dynamic range of signal strengths suitable for pulse-height analysis. (The dynamic range required was approximately

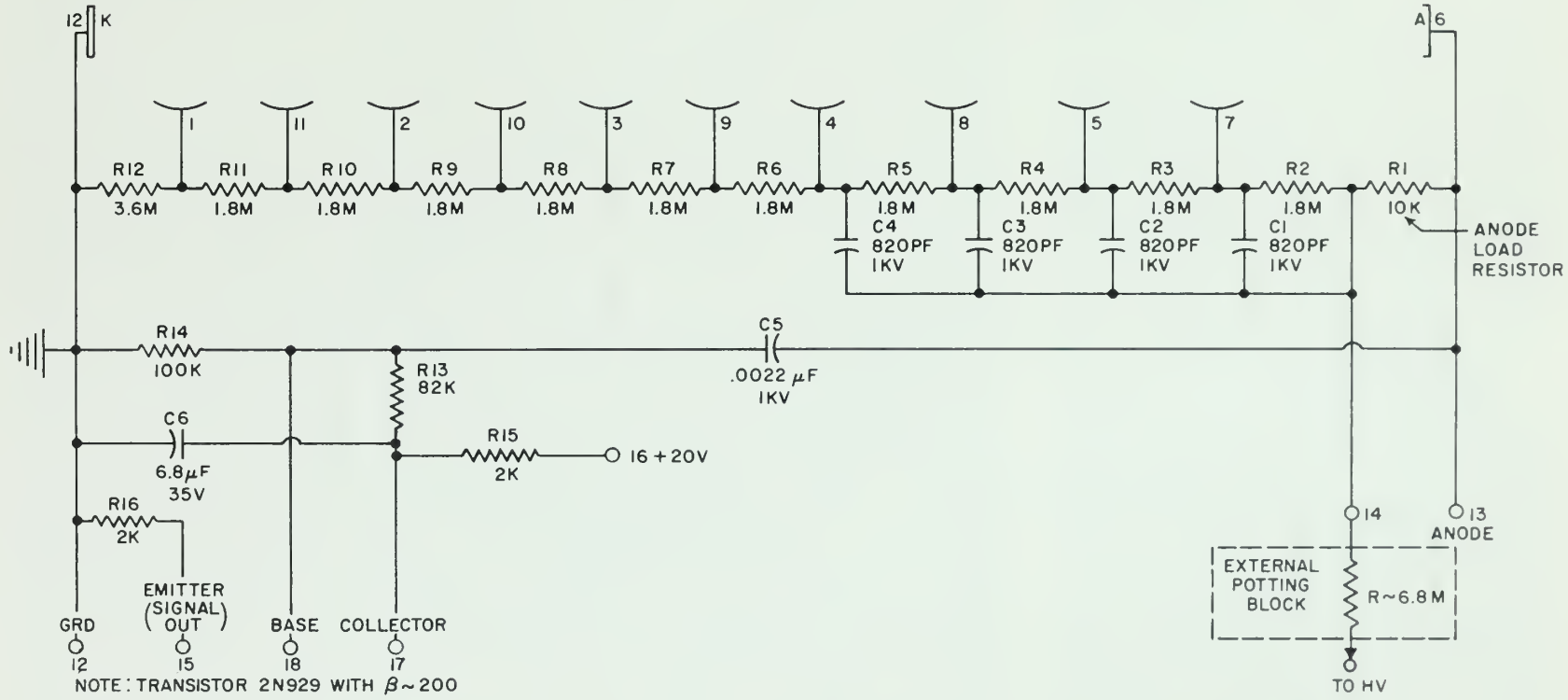

Figure 11. Photomultiplier Tube-Base Circuitry

a factor of 50 in signal strength.) The amplifier circuitry chosen for Detector 2 is shown in figure 12. The output points, A and B, of the emitter followers for each stage of amplification differ by a gain of 10. Each stage has a linear signal range of about 1 to 10 volts. Setting 2 volts as a lower threshold for signal analysis, the amplifier provides an approximate dynamic range of 1 to 5 times threshold in the higher stage, and 10 to 50 times threshold in the lower stage. These signal levels were suitable for pulse-height analysis. The same amplifier circuitry was used for Detectors 2 and 3. Only the high-gain output signal from Detector 3 was used for anticoincidence and counting circuitry.

The design features of the pulse-height analyzers which were to be used required analyzing (sorting out) signal pulses which fell within a certain voltage band, ~1 to 9 volts, and registering the pulses into separate channels. The analyzing method used must provide reliable results. This required that channel thresholds be sharply defined, and registering techniques be exact so that the incoming signal pulse would be kicked into only one well-defined output channel. The design chosen was based upon the functional concepts shown in figure 13. The incoming signal pulses were routed in parallel to the input emitter followers of tunnel-diode discriminators set at different threshold levels. Whenever the wavefront of the signal pulse exceeded the sharply defined threshold level at which tunnel-diode switchover action occurred, the discriminator triggered a monostable multivibrator. The pulse shape of the multivibrator output was a square wave of about two microseconds duration. The triggering of this pulse stretcher acted, in effect, as stored information to indicate that the signal pulse had exceeded the threshold level of that particular channel. Later in time (so as to ensure that the signal pulse was past its peak), a short square-wave "read out" pulse of about 0.5-microsecond duration was generated by a multivibrator which was delayed approximately

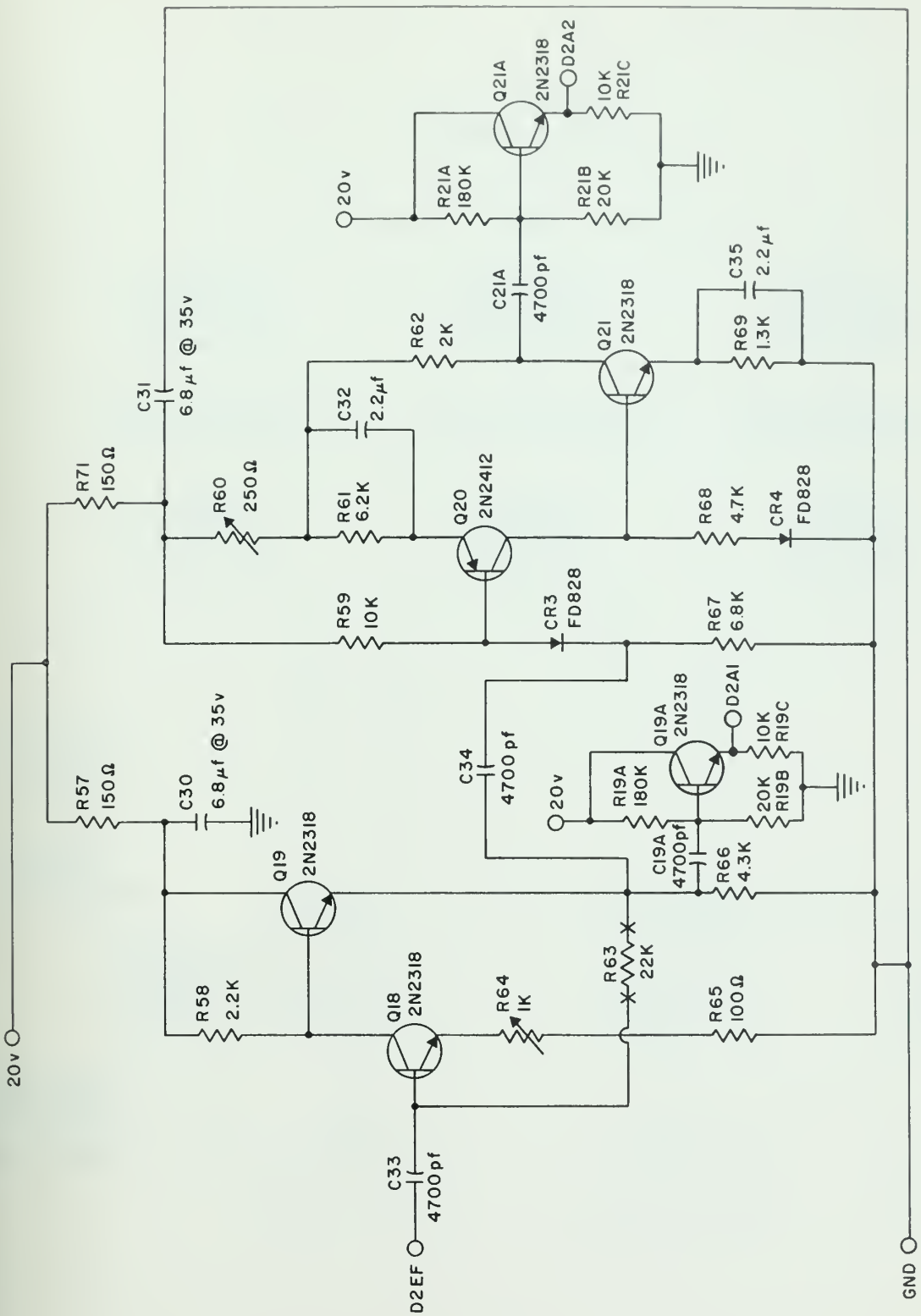

Figure 12. Amplifier for Photomultipliers

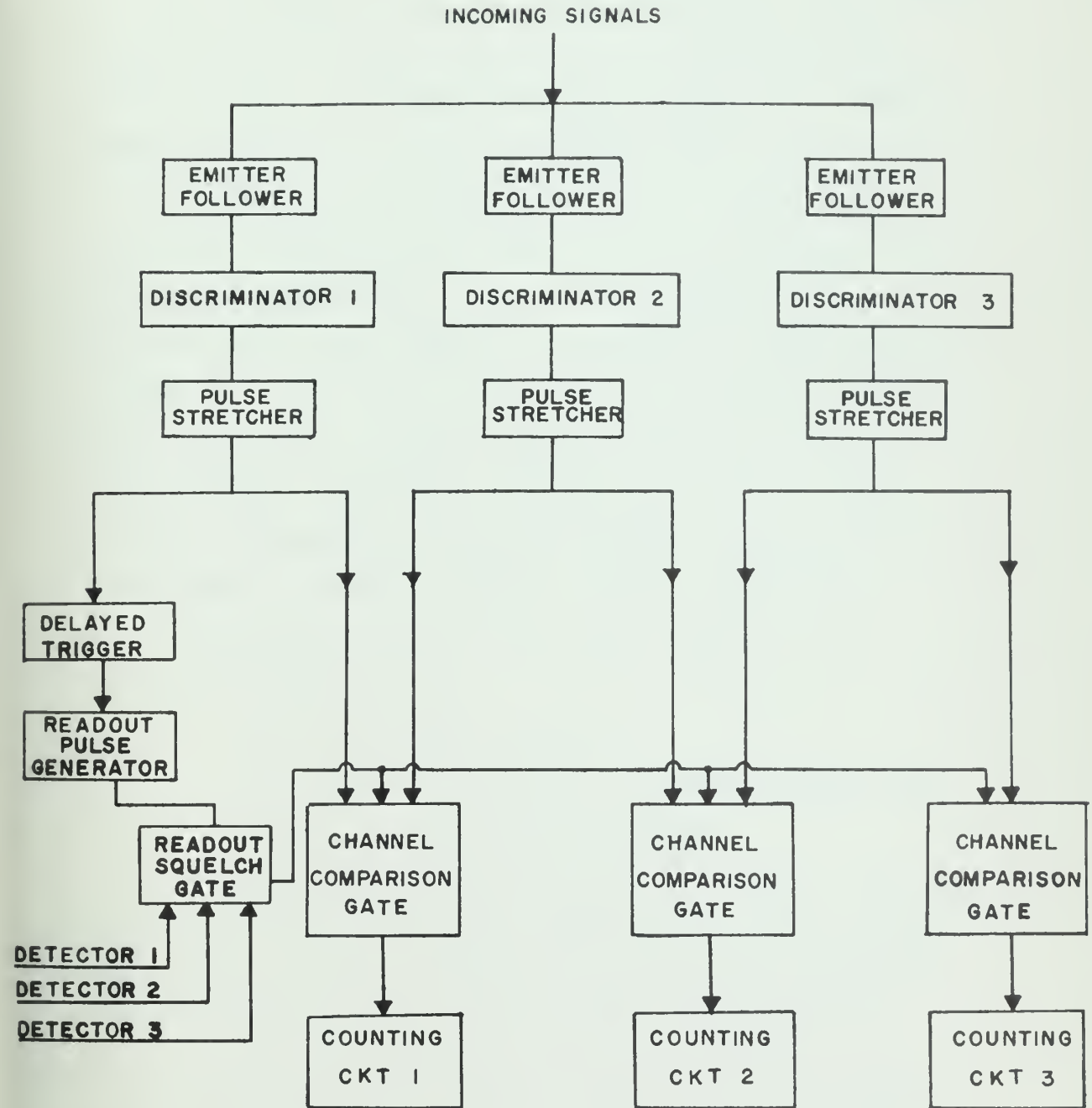

Figure 13. Pulse-Height Analyzer (Functional Concepts)

0.8 microsecond from the triggering time of the lowest level discriminator. If proper coincidence relations existed among the three detectors, the readout pulse would be sent to all channels for possible transfer to counting circuitry through a channel-comparison gate. If proper coincidence relations did not exist, the readout pulse would be squelched before reaching the channel-comparison gates. In each channel-comparison gate, if the lower of the two channels had been triggered but the one immediately above it had not, then the readout pulse would effectively be transferred to the counting circuits for the lower channel. If, however, the channel above it had also been triggered, its stretched signal, which completely overlapped the readout pulse in time, would squelch the readout pulse in the comparison-gate of the lower channel. Pulses would not, therefore, be incorrectly passed to the counting circuitry for the lower channel. Using this logic, any number of similar stages could be stacked to form a multichannel pulse-height analyzer. Circuitry for a three-channel pulse-height analyzer is shown in figure 14.

The design of the two pulse-height analyzers of the experiment differed only in

(1) the number of channels,

(2) the type of gate used to squelch readout, and

(3) the output counting circuitry.

The pulse-height analyzer designed for Detector 1 used (1) three energy channels (between ~1 and 8 Mev), (2) Readout Squelch Gate 1 shown in figure 15 which was driven by a "no" indication from both Detectors 2 and 3, and (3) three count-rate meters.

The pulse-height analyzer designed for Detector 2 used (1) five energy channels (between ~1.5 and 110 Mev), (2) Readout Squelch Gate 2 shown in figure 16 which was driven by a "yes" indication from the proton discriminator of Detector 1 and a "no" indication from Detector 3, and (3) five scalers.

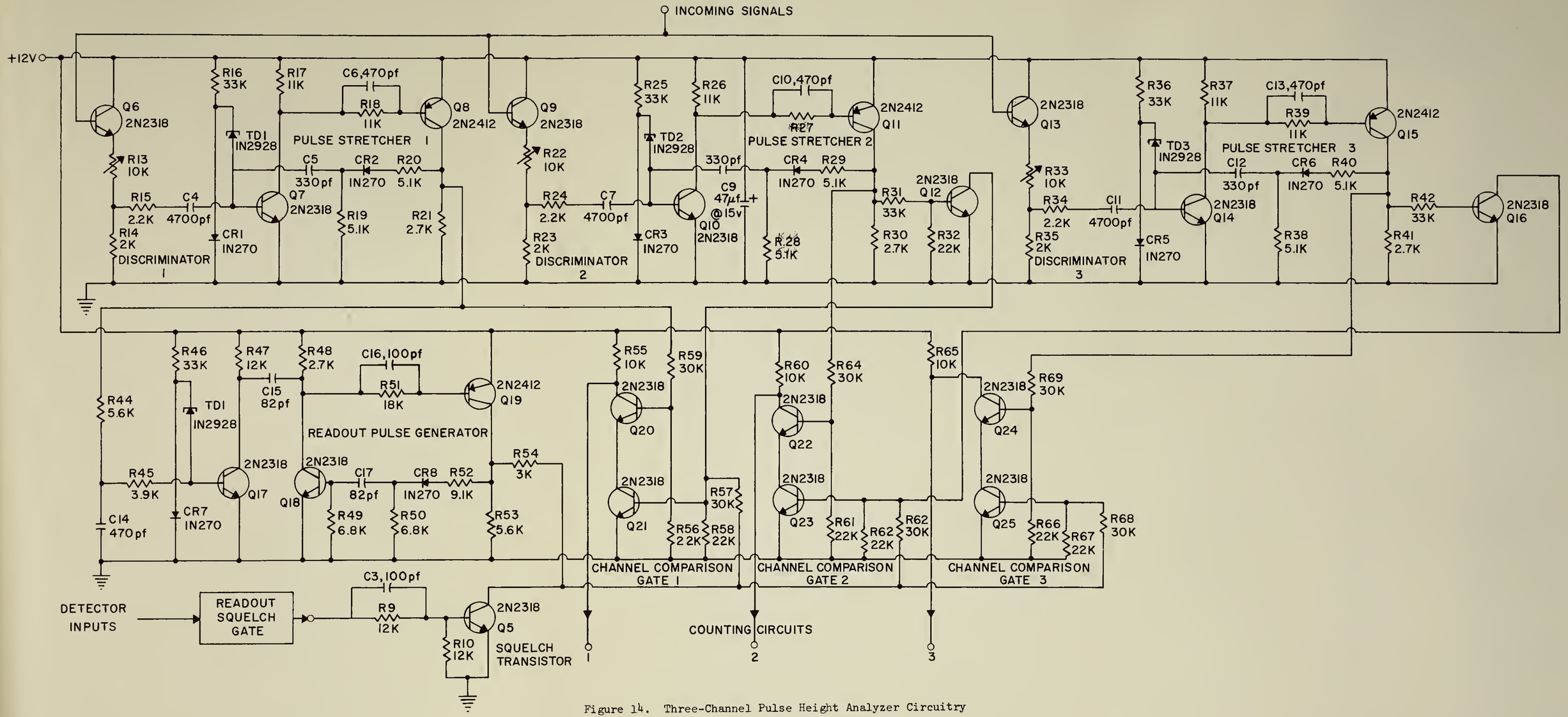

Figure 14. Three-Channel Pulse Height Analyzer Circuitry

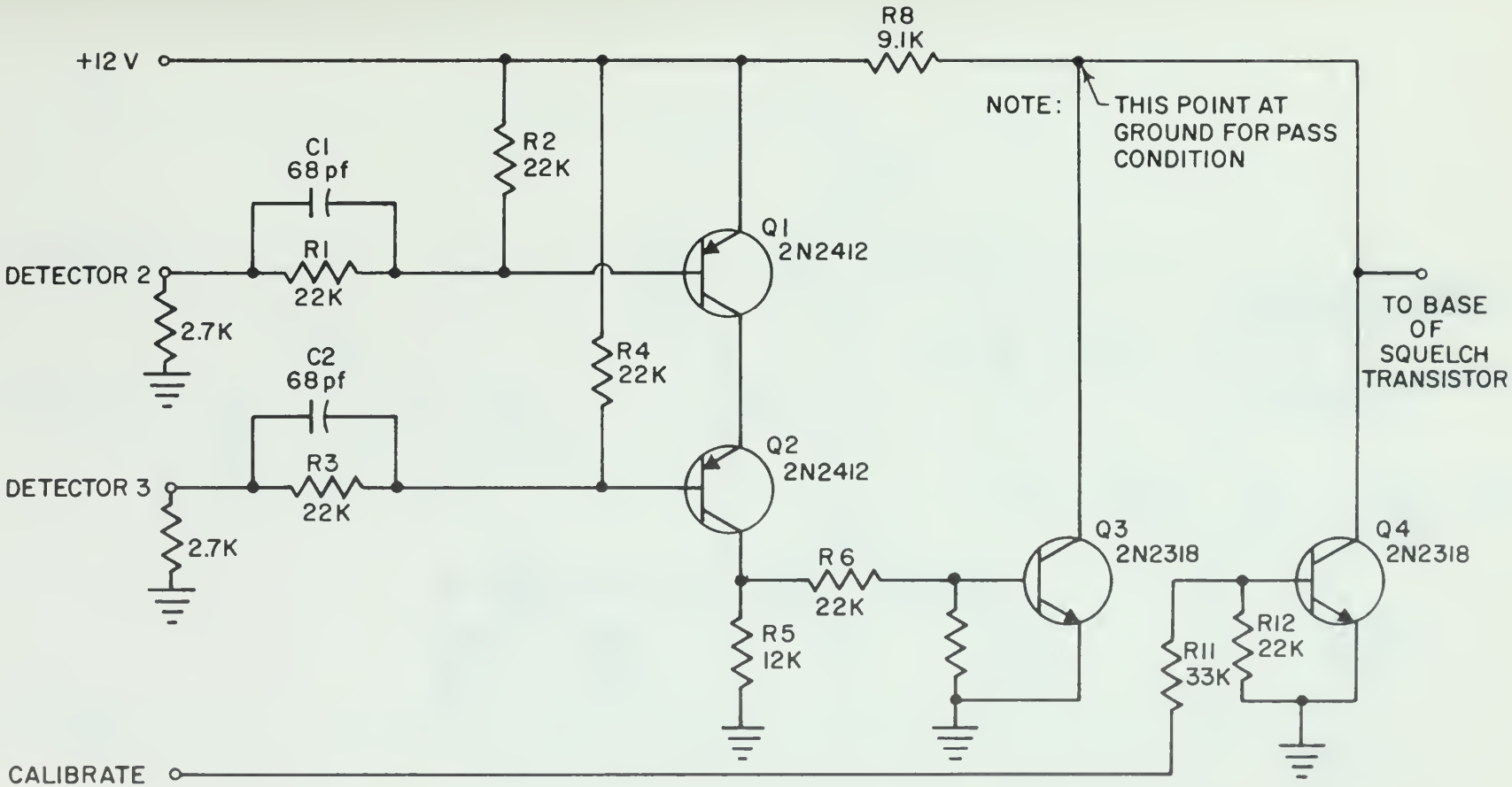

Figure 15. Readout Squelch Gate 1 Circuitry

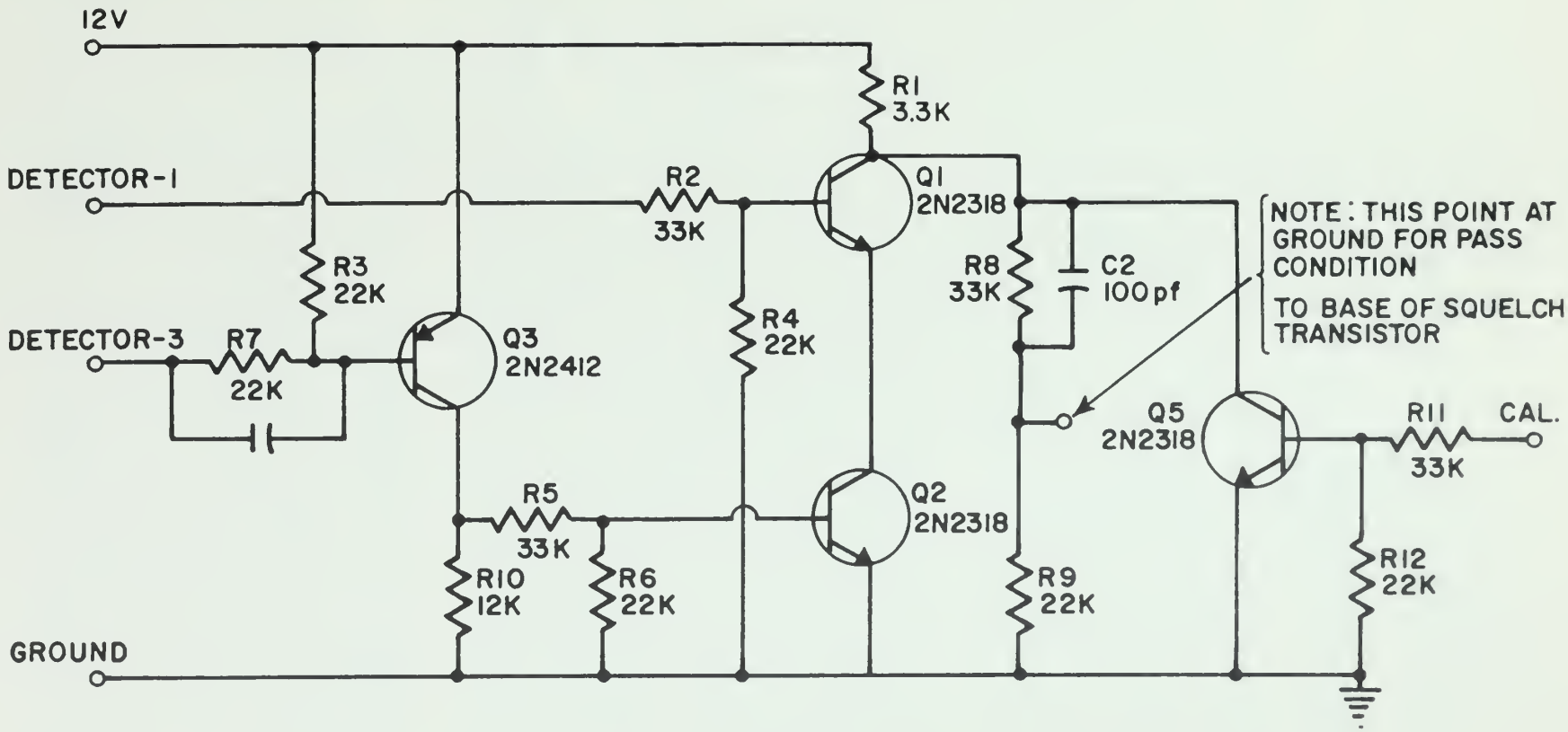

Figure 16. Readout Squelch Gate 2 Circuitry

Counting circuits used either of two techniques:

(1) Integrating circuitry for channels where high flux ($\geq$32 counts per second) was expected.

(2) Scaler "stepping" circuitry for channels where low flux (<32 counts per second) was expected.

Integrating circuitry (a count-rate meter) was designed to (1) provide a counting-rate range to 20,000 counts per second with a sensitive linear region between 100 and 1000 counts per second, and (2) be independent of environmental changes. The standardized circuitry chosen for count-rate meters is shown in figure 17. A counting-rate calibration curve for this count-rate meter circuitry is shown in figure 18.

Because of the expected low counting rates for high-energy particles, scaler stepping circuitry was designed to provide only 31 steps between recycling. The circuit is shown in figure 19. Five flip-flop multivibrator circuits were stacked in binary sequence and their current outputs proportional to the binary counts registered were combined in R68 to provide 31 "staircase steps" between zero and positive 5 volts d.c. A sixth scaler circuit was used to register the counts passed by the High-Energy Gate. The requirements for registering high-energy particles were discussed earlier and exhibited in the revised logic of figure 8. This logic is accomplished by the High-Energy Gate shown in figure 20.

For passing action, the High-Energy Gate requires (1) a signal pulse coupled through C12 from the lower-threshold discriminator (>260 kev) of Detector 1, (2) a signal pulse coupled through C13 from the highest-energy channel (>48 Mev) of Detector 2, and (3) no signal pulses either from the proton threshold discriminator (>550 kev) of Detector 1 or from Detector 3. These coincident signals would cause the High-Energy Gate to generate a negative output pulse at the collector of Q12 which would be transferred to a scaler and be registered in telemetry channel

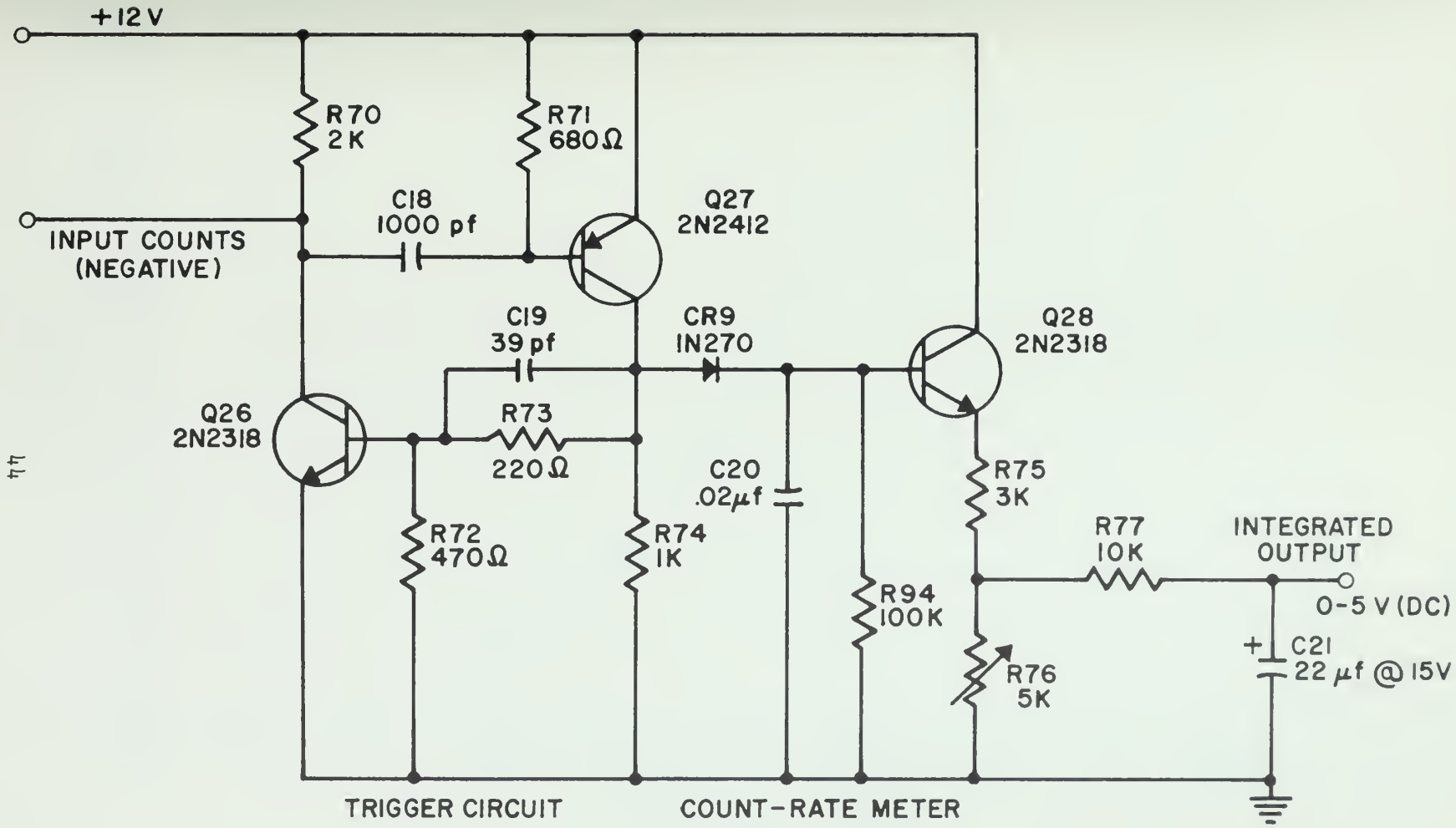

Figure 17. Count-Rate Meter Circuitry

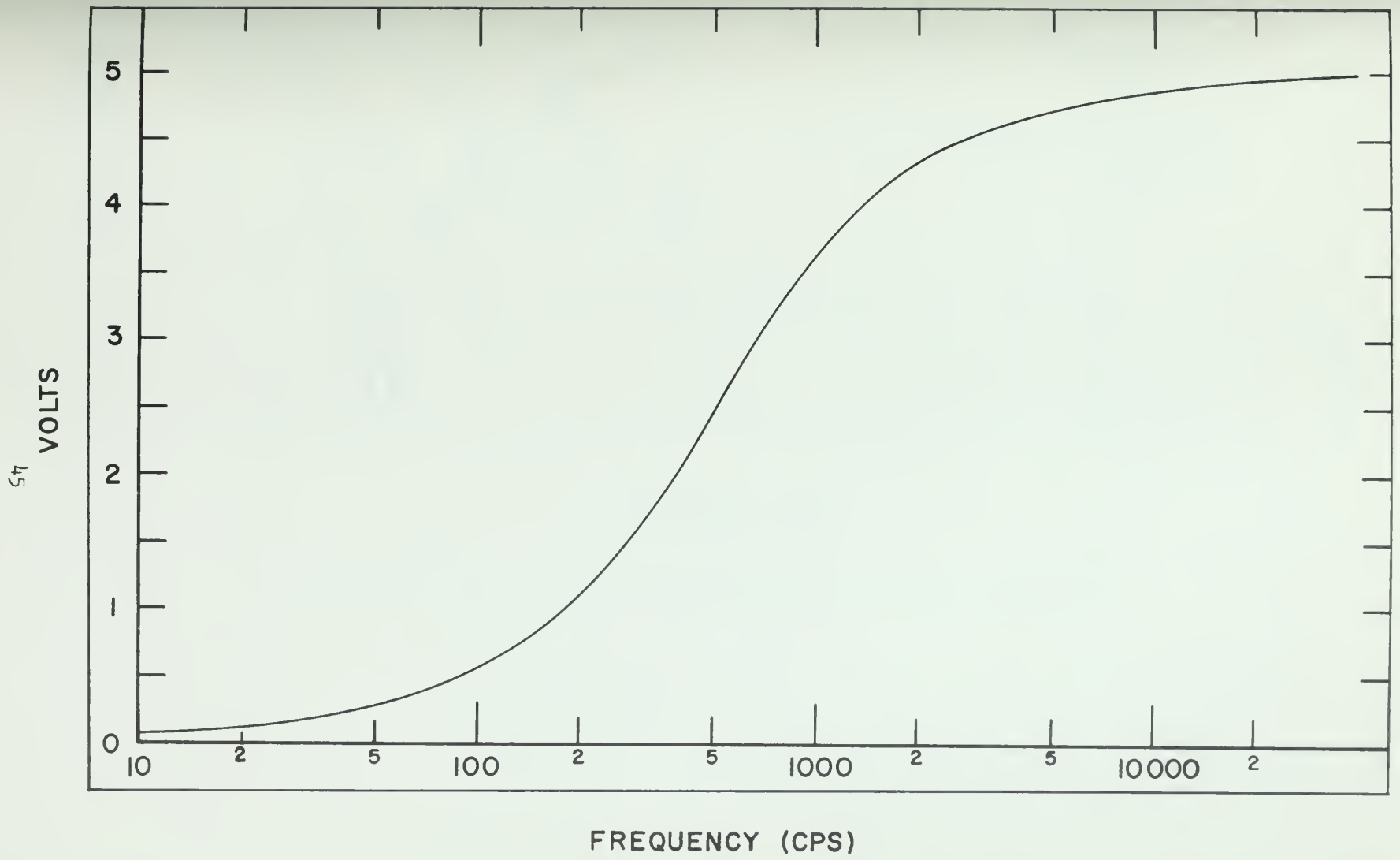

Figure 18. Typical Calibration Curve for Count-Rate Meter

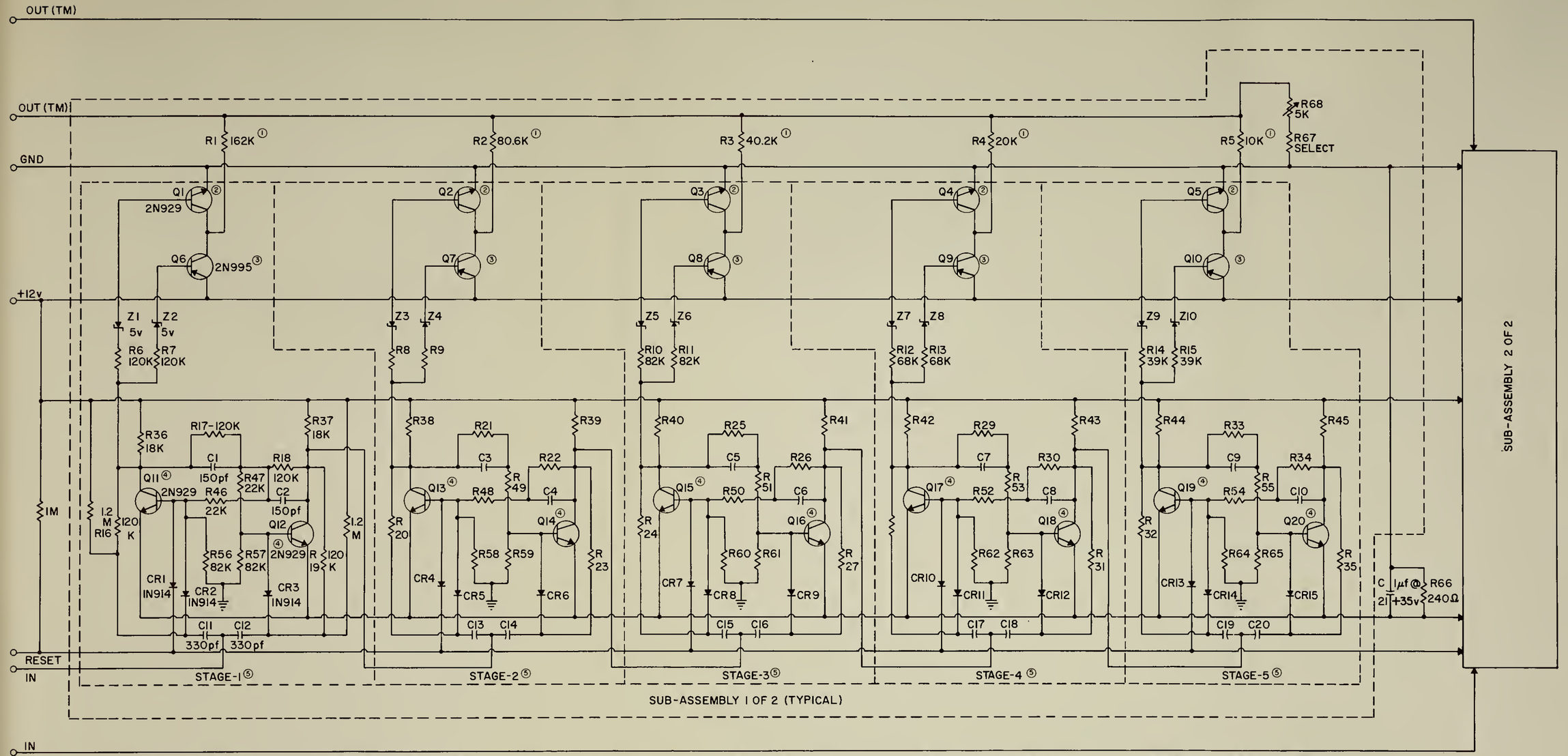

NOTES, UNLESS OTHERWISE SPECIFIED: 1.- 1/8 WATT CARBON OR METAL FILM ± 1% TOLERANCE, T.C. 25pp M/°C 2.- BETA > 50 AT 0.5 MA. Ic. 3.- BETA > 30 AT 0.5 MA. Ic. 4.- BETA > 200 AT 0.5 MA. Ic, AND MATCHED WITHIN 20 %. 5.- COMPONENT SPECIFICATIONS IN STAGE I ARE TYPICAL FOR ALL STAGES.

Figure 19. Five-Bit Binary Scaler Circuitry

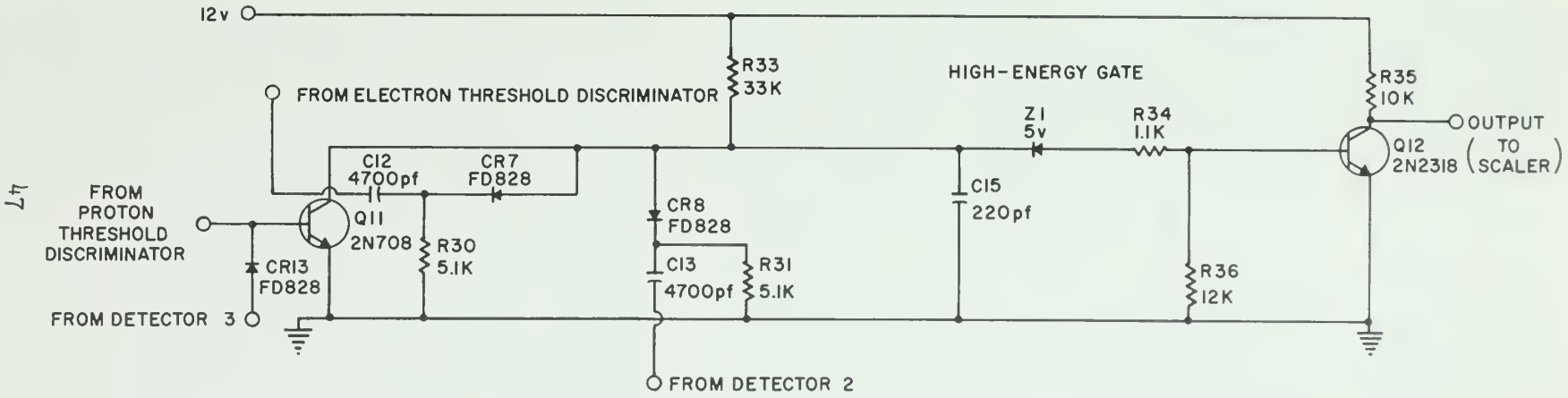

Figure 20. High-Energy Gate Circuitry

TM9. However, if a coincident pulse arrives at the gate either from Detector 3 (guard fluor) or from the proton threshold discriminator of Detector 1, then the High-Energy Gate will not generate an output pulse since it will be squelched by transistor Q11.

The final item of circuitry design to be discussed now is the low-noise, high-gain amplifier used with the solid-state Detector 1. The range of useful signal strengths at the input stage of this amplifier was equivalent to 0.3 to 10 millivolts (negative peaks of signal pulses) across a detector capacitance of about 100 micro-microfarads. Thus, contrary to the voltage gain of about 30 used in the amplifiers discussed earlier, this amplifier would require an overall gain of about 1500. Also, a dynamic range factor of about 30 times the threshold setting would be required. These characteristics, however, must be obtained without loss of linearity of signal or the introduction of noise, so that the amplified signals are satisfactory for use in pulse-height analysis. The analyzed outputs would activate count-rate meter circuits to provide counting rates of low-energy protons (~1 to 8 Mev).

Because Detector 1 responded to radiations by producing a charge, it was decided to use a charge-sensitive amplifier for the necessary amplification. This choice was dictated by the fact that, effectively, voltage amplification depends on the input capacitance of the detector and its interconnecting cables. This input capacitance is not completely stable because environmental changes, principally temperature, affect noise current, resulting in bias changes. However, the detrimental effect of these variations can be nullified by the use of a charge-sensitive amplifier which by design stabilizes its input capacitance by use of a feedback capacitance. The amplifier therefore receives a nearly constant fraction of the charge response of the solid-state detector as its input signal.

The circuitry for the charge-sensitive amplifier is shown in figure 21. Stability is obtained by use of feedback capacitance C1. A tank circuit, L1 and C12, which is critically damped for the frequency of 2 megacycles is used to shape the amplified signal pulse so that it reaches peak value before 0.5 microsecond, and is of the desired short duration (falls to 10 percent of peak in under 3 microseconds). The output points, A and B, of the emitter followers provide the desired amplified signals for use in pulse-height analysis.

Intrinsic noise of solid-state detectors with large surface area (~3 cm^2) due to their high capacity (~100 micro-microfarads), as well as transistor noise in the input stages of the amplifier, provided a lower limit on the usable threshold for particle detection in Detector 1. Undesired interactions among circuit elements introduced other noise problems. To combat these irksome problems, design of the amplifiers, and particularly the charge-sensitive amplifier, included:

(1) Use of electromagnetic shielding for the amplifiers. A grounded shielding plane was placed between amplifiers and other circuitry.

(2) Use of shielded wire for all interconnections. In addition, Microdot coaxial cable was used for leads carrying signals before pulse-height analysis.

(3) Use of decoupling circuits and special grounds wherever beneficial.

(4) Use of separate voltage regulators to provide circuit isolation. These provided independent, filtered operating voltages to the charge-sensitive amplifier, the amplifiers for the photomultipliers, the analyzing circuitry, and the high-voltage power supply.

Nevertheless, the noise level present at the high-gain stage of the charge-sensitive amplifier was the limiting factor on setting the lower threshold for identifying particle flux that

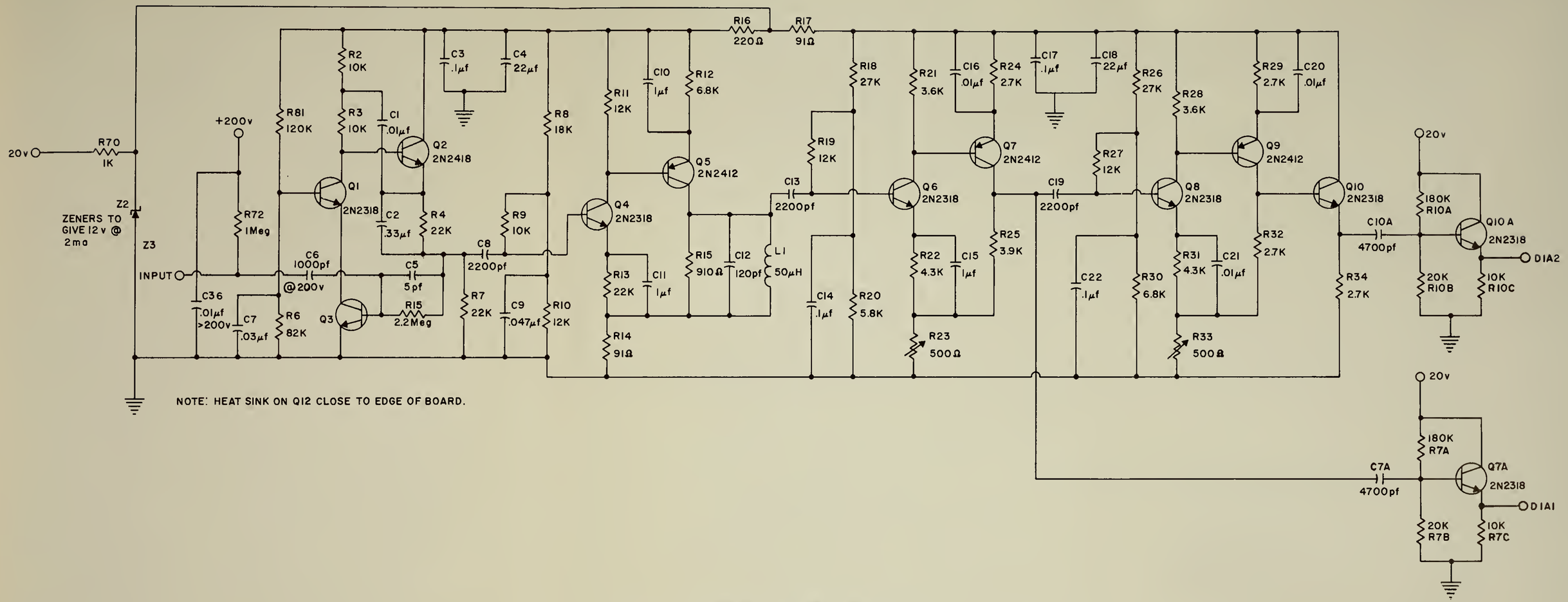

Figure 21. Charge-Sensitive Amplifier Circuitry

entered Detector 1. The noise level present was equivalent to energies of about 200 kev being deposited in Detector 1. The effective detection threshold for Detector 1 was therefore set to discriminate at the equivalent of 260 kev of energy being deposited in the solid-state detector.

To recapitulate, the major points discussed in this subsection on electronic circuitry included the design considerations used in selecting:

(1) The two photomultiplier systems using

(a) two RCA type 6649 photomultiplier tubes,

(b) tube-base circuitry with suitable pulse-shaping characteristics.

(2) The two pulse-amplifier systems.

(3) The two pulse-height analyzer systems using

(a) tunnel-diode discriminators,

(b) monostable multivibrators, and

(c) channel-comparison gates for readouts.

(4) The gate circuitry.

(5) The counting circuitry using

(a) integrating circuits (count-rate meters) and

(b) stepping circuits (scalers).

(6) The charge-sensitive amplifier.

For simplicity in fabrication, standardized circuitry was used wherever practicable to perform similar functions.

c. Power Supply and Voltage Regulation

The primary goal in the design of the power supply and voltage regulation circuitry was to convert battery voltage (positive 24$\pm$4 volts d.c.) to other regulated d.c. voltages for the proper operation of the circuitry in the experiment. In

addition, because of possible interactions among circuits, isolation and filtering circuitry was extensively used to minimize noise. These design considerations led to the use of

(1) An input isolation filter;

(2) A high-voltage DC/DC converter (for photomultiplier anode voltage and solid-state detector bias);

(3) A 28 to 21 v d.c. voltage regulator (for video-amplifier circuitry);

(4) A 21 to 12 v d.c. voltage regulator (for the charge-sensitive amplifier);

(5) A 28 to 12 v d.c. voltage regulator (for analyzing circuitry other than amplifier systems).

The functional relationships among these subsystems are shown in figure 22.

An input isolation filter protected the experiment against surge currents during turn-on and against the reverse surge currents which might occur at normal turn-off or when the input is grounded inadvertently by circuit failure. The isolation filter effectively decoupled the experiment from interacting with circuitry of the space vehicle.

A DC/DC converter provided the positive high voltage (~1 kv) used as anode voltage supply for the photomultiplier tubes. This power supply was fabricated in a module placed close to the photomultiplier tubes which minimized the length of the high-voltage leads. The circuitry is shown in figure 23. Voltage regulation was provided in the connecter primary by the 28 to 20 v d.c. regulator and in the secondary by the 1000 v d.c. Corona Tube. The high-voltage output was filtered in the module. Provisions for additional filtering, if needed, were made at the dropping-resistor potting blocks near the photomultiplier tubes. The DC/DC converter also provided a positive 200 volts d.c. for bias in Detector 1. As shown in figure 23, this voltage was obtained

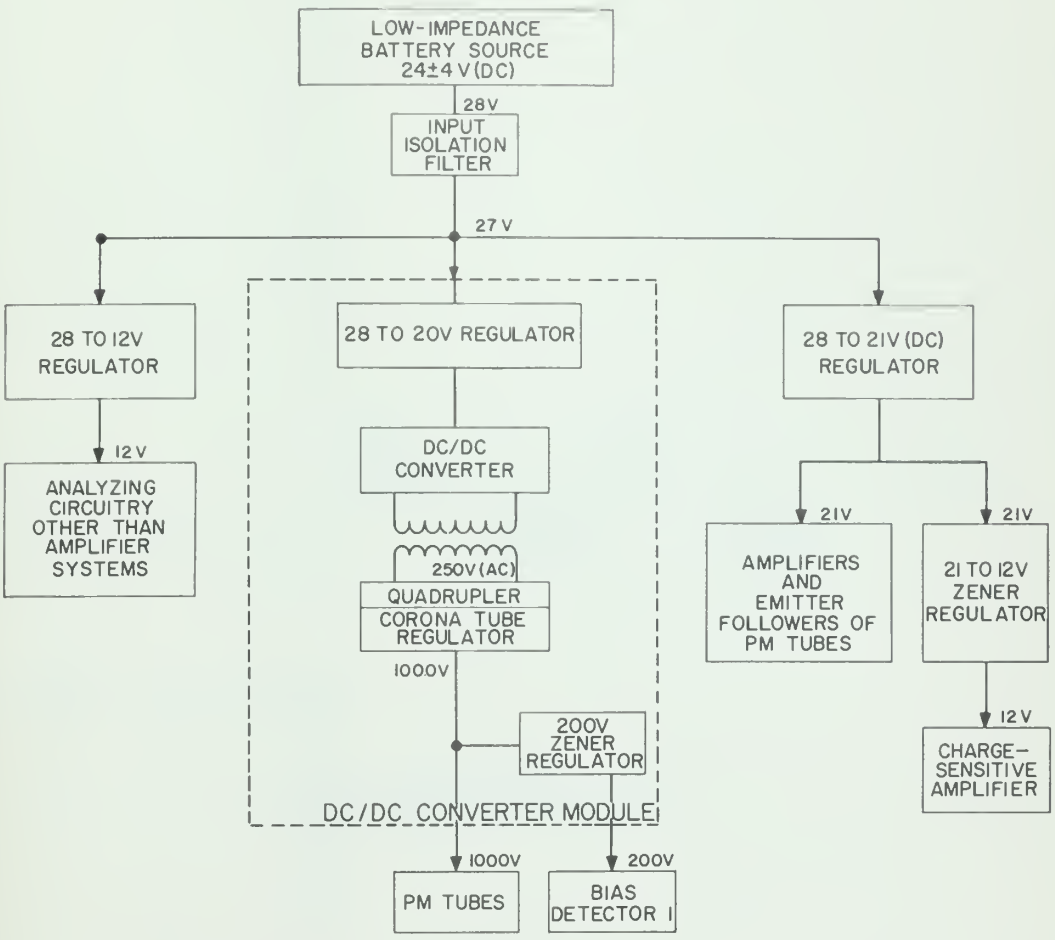

Figure 22. Power Supply and Voltage Regulation System

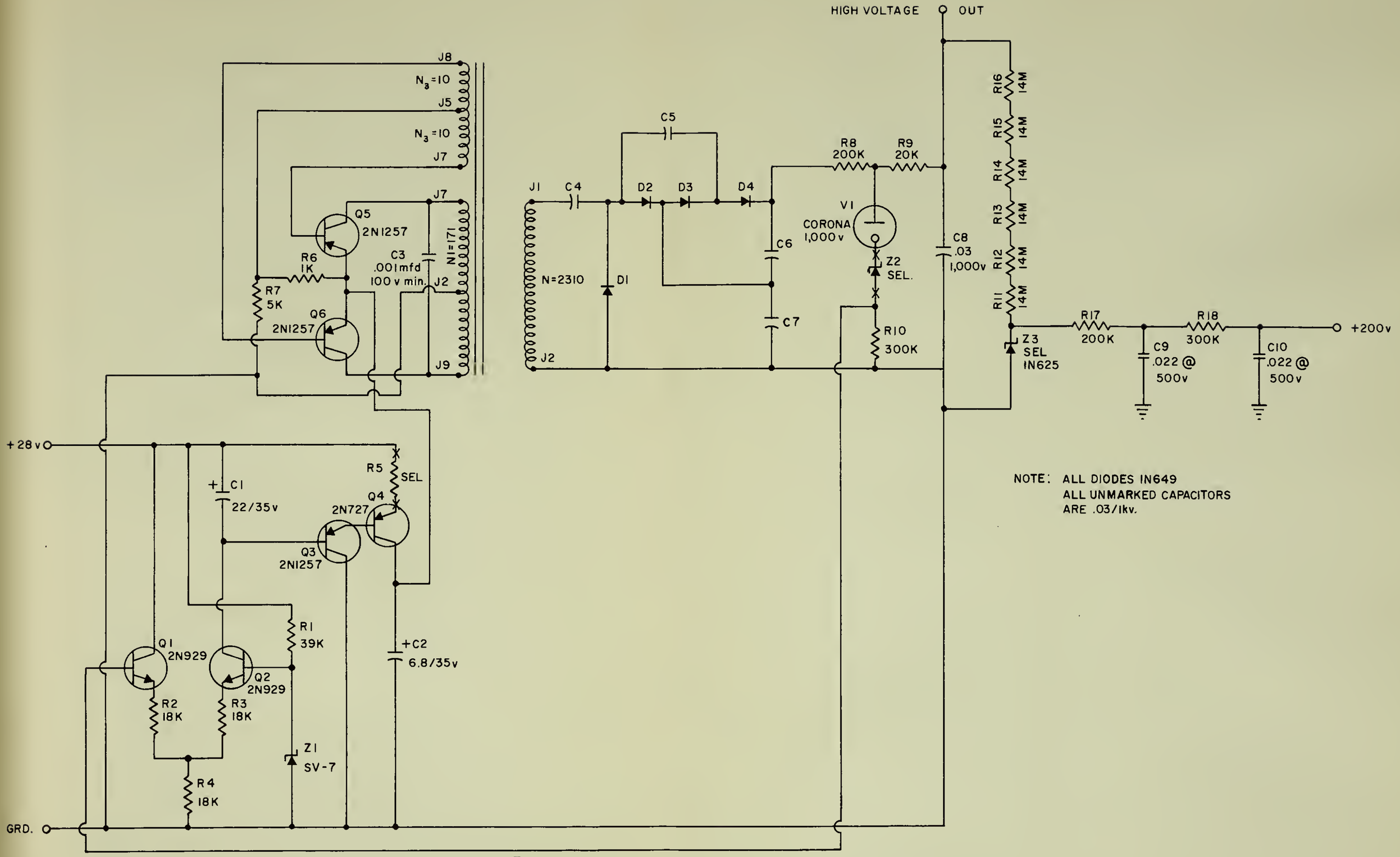

NOTE: ALL DIODES IN649
ALL UNMARKED CAPACITORS
ARE .03/1kv.

Figure 23. DC/DC Converter Circuitry (High Voltage Power Supply)

by a bleeder-resistor network across the high-voltage supply. A Zener diode (200 volts) was used to regulate this bias voltage, which was filtered through two stages within the module. Another stage of filtering was provided at the connector junction on the amplifier printed-circuit board. The current drain on the bias supply was expected to be very low (<10 microamperes). Bias regulation should not therefore be influenced noticeably by small fluctuations in the regulated high-voltage supply. These efforts at reduction of noise fluctuations were especially important since the bias voltage was applied on the same lead of the Microdot coaxial cable that would carry the signal responses of Detector 1.

The two stepdown voltage regulators of standard design provided ~50 milliamperes of load current at their respective output voltages of positive 21 and 12 volts d.c. The charge-sensitive amplifier obtained its operating voltage, positive 12 volts d.c., by a bleeder-stepdown arrangement on the 21-volt regulator used for the other amplifiers. This voltage was regulated by a 12-volt Zener diode. Since the current of the charge-sensitive amplifier was small (~6 milliamperes), no interaction of voltage regulators was expected. The circuitry chosen for the power supply and voltage regulators is shown in figure 24.

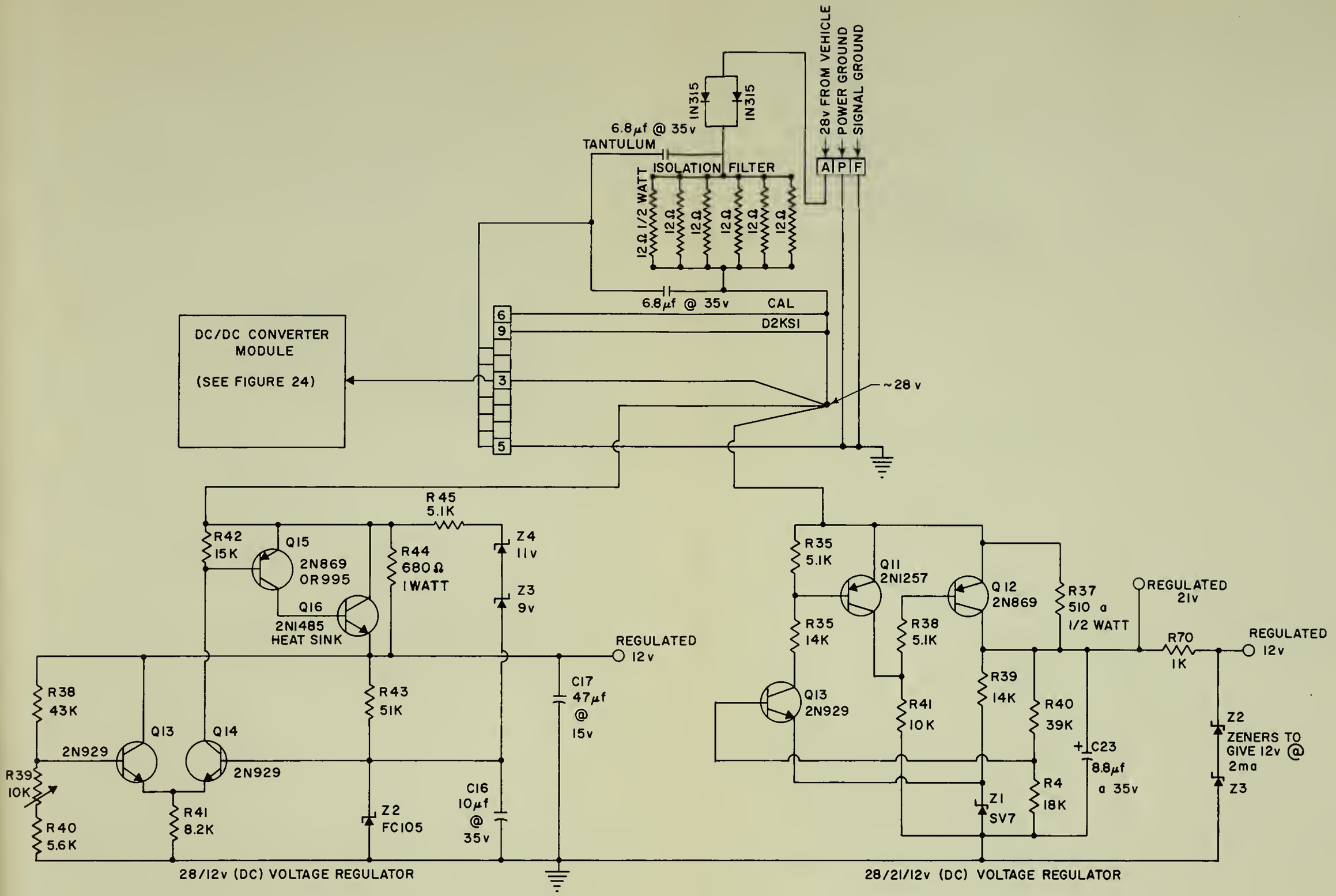

Figure 24. Voltage Regulation Circuitry

SECTION III

THE INSTRUMENT

The experiment consisted basically of three detectors arranged to form a radiation telescope, and electronic circuitry to process detector signals so as to provide information on the composition, flux, and energy spectra of the radiations that activated the telescope. The instrument is shown in figure 25. The physical characteristics of this assembly were the following:

1. Weight 9.45 pounds
2. Size within a volume 11 in. x 7 in. x 7 in.
3. Power 3.5 watts (at positive 28 volts d.c.)
4. Telemetry eleven channels (analog 0 to 5 volts)

The functional and design concepts of the experiment were discussed in section II. A diagram of the final logic which implemented these concepts is shown in figure 26. This diagram outlines the interrelationships among component parts of the instrument. The physical description of the instrument follows.

1. The Telescope

The arrangement and construction details of the telescope are shown in figures 10, 25, and 27. The telescope was housed in an 0.25-inch-thick aluminum casing. It was mounted by means of its pedestal base onto the roof of the 0.085-inch-thick magnesium electronics can.

Information on the three detectors used to form the telescope follows:

a. Detector 1, obtained commercially from Oak Ridge Technical Enterprises (ORTEC), was a very thin (426 microns depletion layer) p-n junction diode suspended as a wafer in a transmission mounting. The physical appearance of the detector is shown in figure 28.

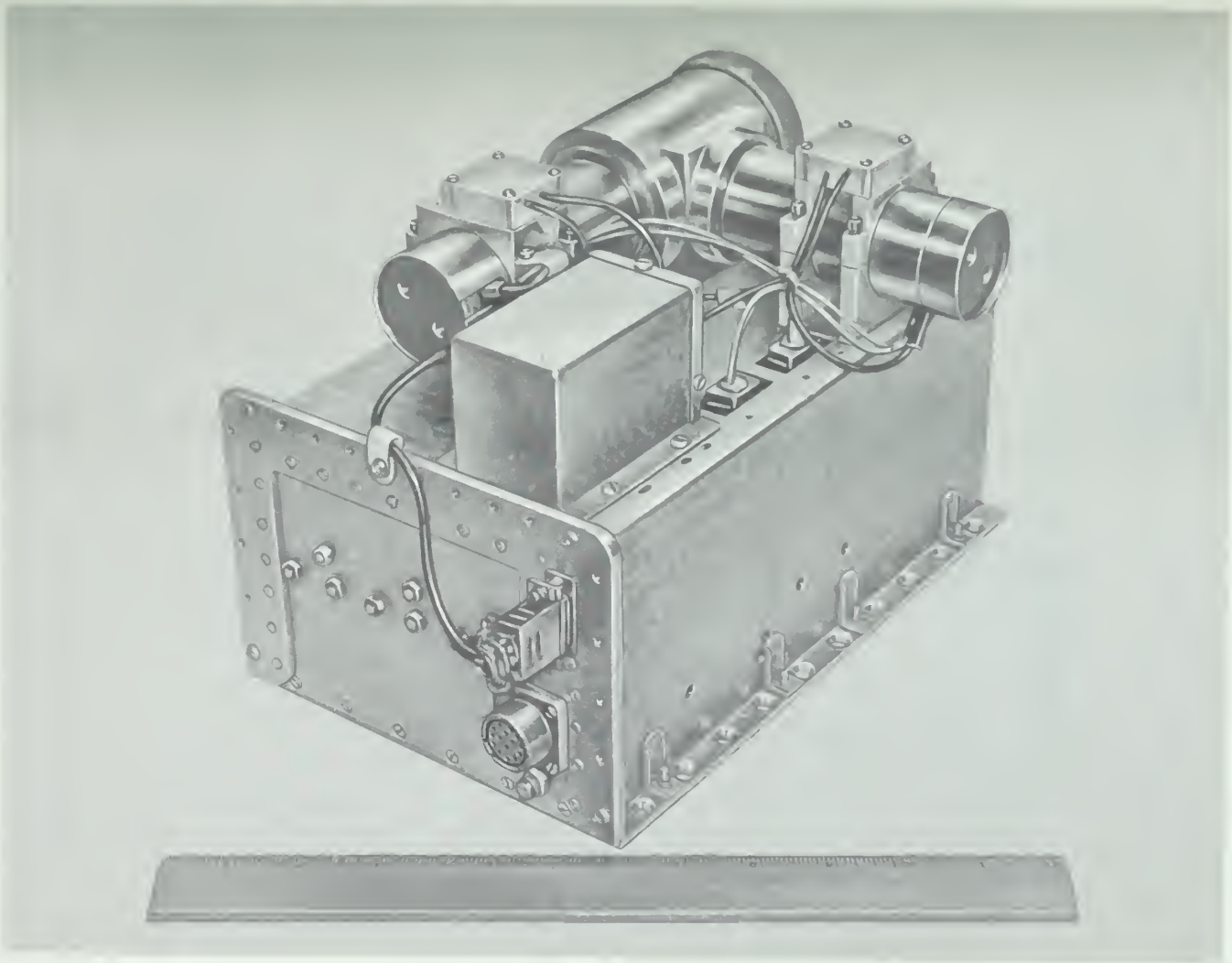

Figure 25. The Instrument (Rear View)

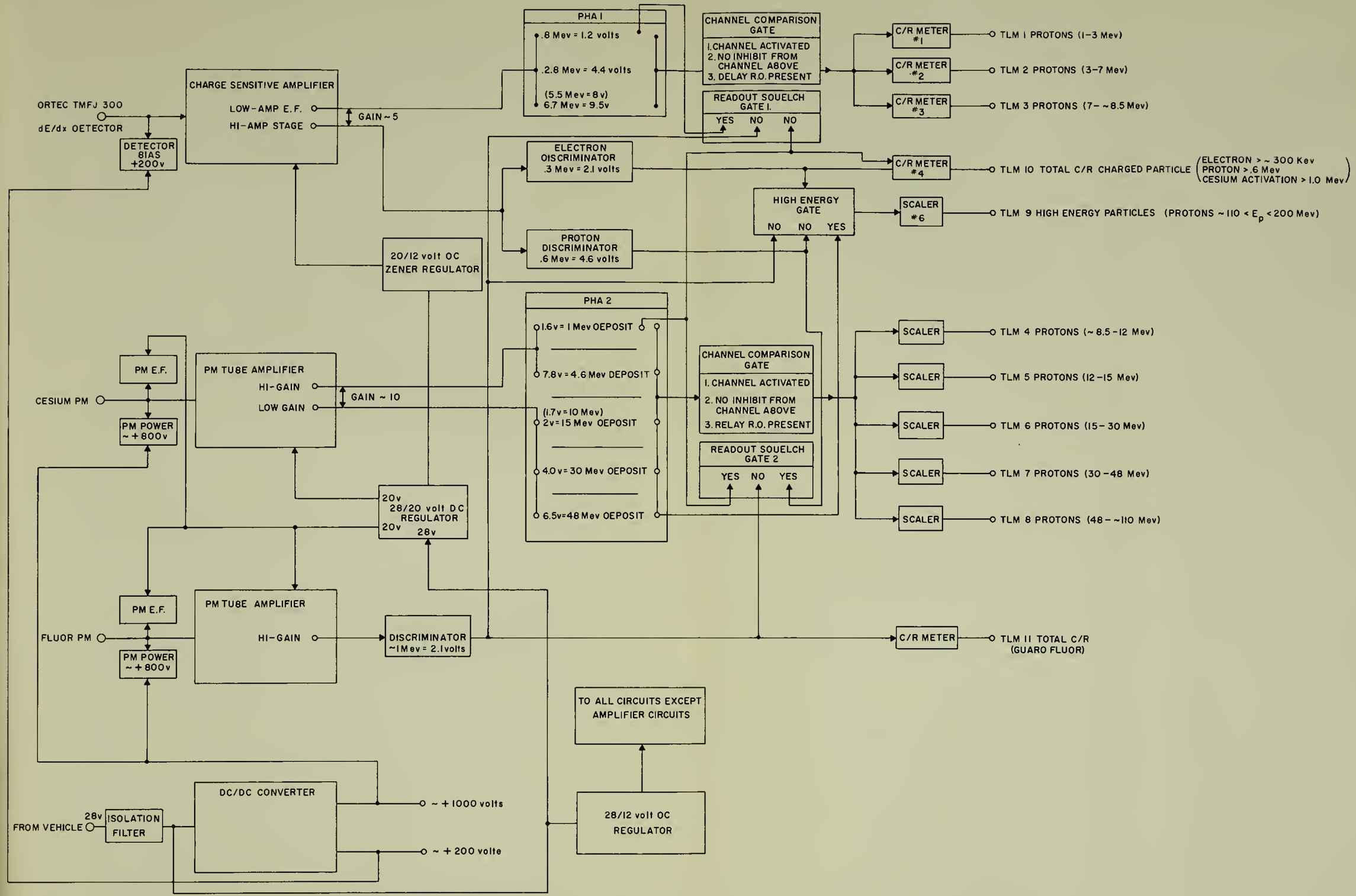

Figure 26. Final Logic of the Experiment

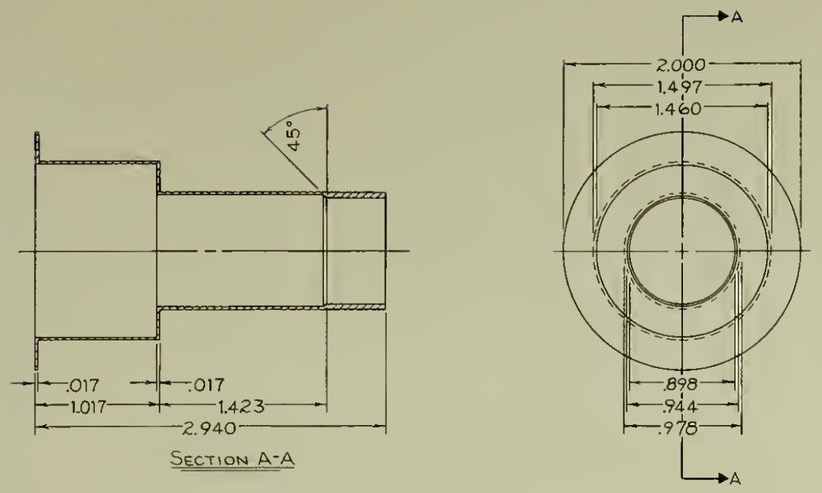

TELESCOPE INSERT LINER
SCALE: 2 : 1
MATL. 2024 ALUMINUM ALLOY

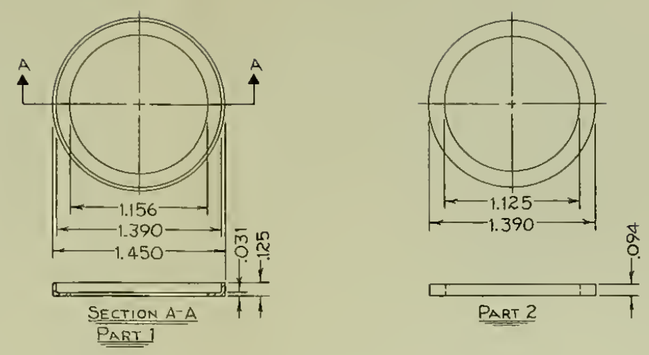

MYLAR HOLDER
SCALE: 2:1
MATL. LUCITE

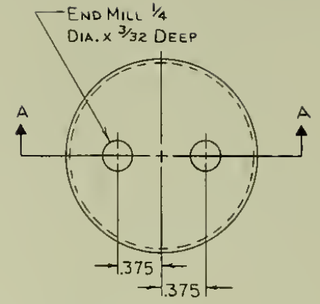

P.M. TUBE CASING CAP
SCALE: 2 : 1
MATL. C.R. STEEL

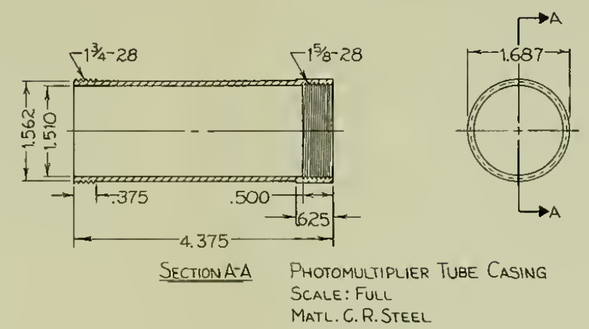

PHOTOMULTIPLIER TUBE CASING
SCALE: FULL
MATL. C.R. STEEL

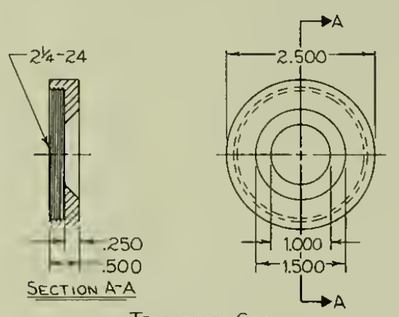

TELESCOPE CAP
SCALE: FULL
MATL. 2024 ALUMINUM ALLOY

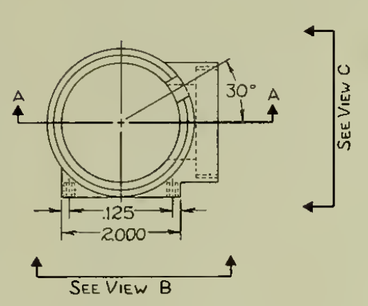

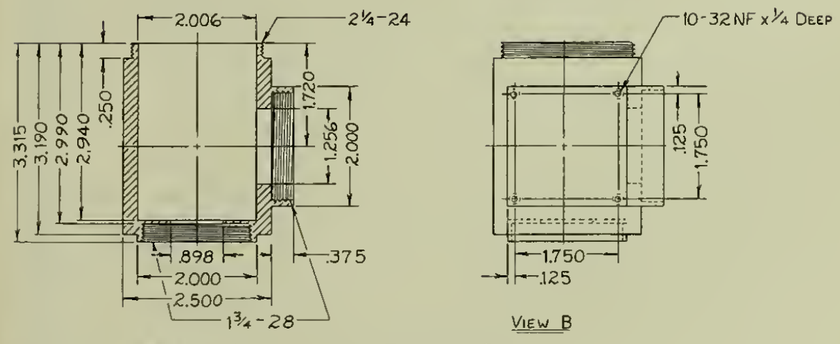

TELESCOPE BODY
SCALE: FULL
MATL. 2024 ALUMINUM ALLOY

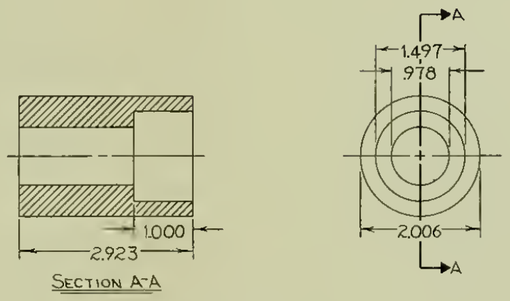

TELESCOPE PLASTIC FLUOR
SCALE: FULL
MATL. PLASTIC

Figure 27. Telescope Construction Details

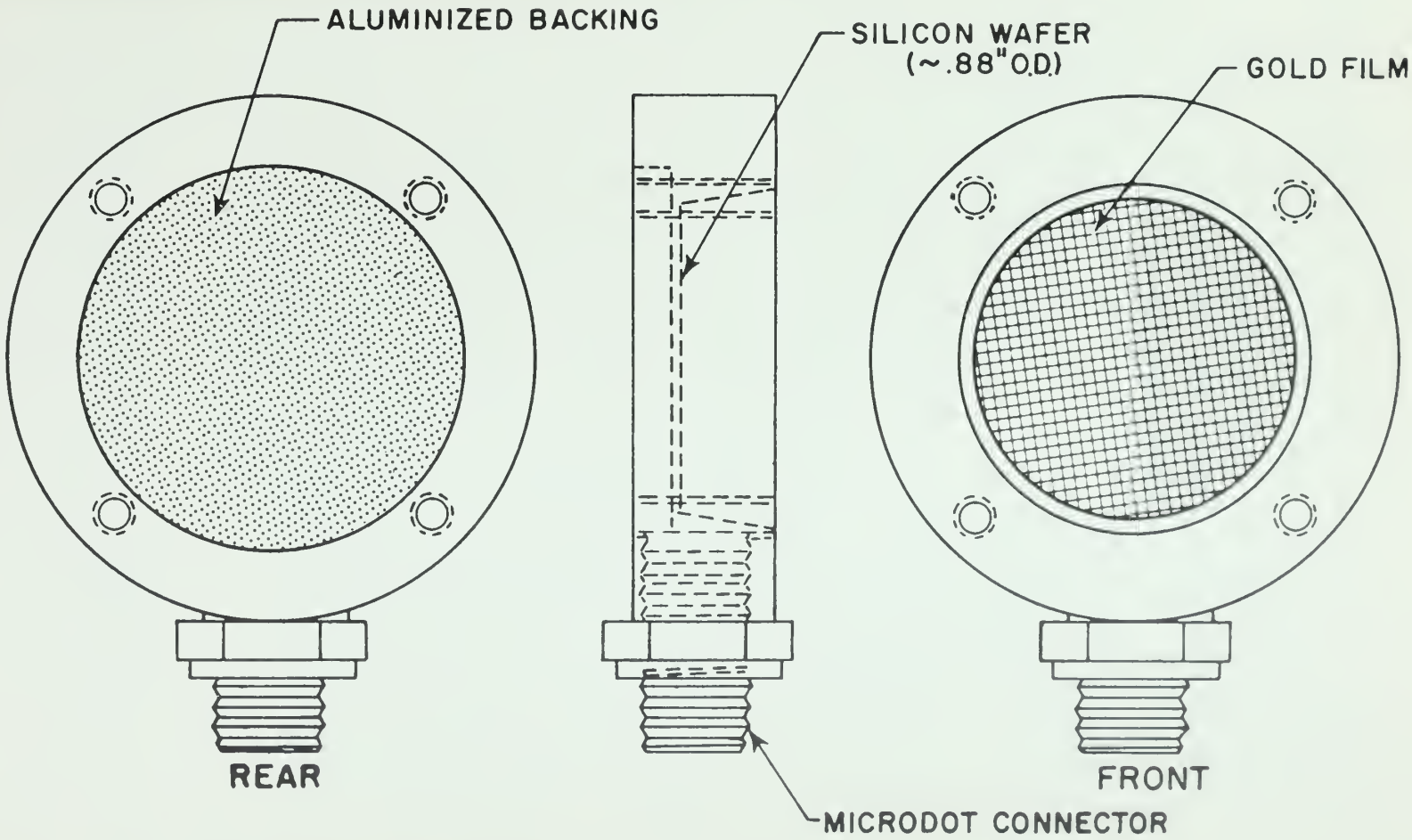

Figure 28. Detector 1

The quality assurance data for Detector 1 are shown in figure 29.

b. Detector 2 was a crystal of cesium iodide (thallium activated), CsI(Tℓ), which was machined into a cylinder 1.44 inches long x 0.986 inch in diameter. The crystal stock was obtained commercially from Crystals Division, ISOTOPES, Inc. The side surface of Detector 2 was painted to improve internal reflectivity with a highly reflective white paint composed of a titanium-dioxide whitener in xylene with B7 acrylic cement. Both top and bottom faces of the cesium iodide crystal were machined clean.

c. Detector 3 was a rod of plastic phosphor material which was machined to surround Detectors 1 and 2 except along the axis of the telescope. It was pierced axially by a front aperture for Detector 1 and by a rear aperture for the lightpipe of Detector 2. The plastic stock was of type SC-700 scintillation material obtained commercially from Crystals Division, ISOTOPES, Inc. Properties of SC-700 are shown in figure 30. All surfaces, except the side lightpipe junction area of Detector 3, were painted to improve internal reflectivity with the same highly reflective white paint used for Detector 2. To provide structural strength and protection from extraneous light, the two photomultiplier tubes were mounted in thin cold-rolled steel tube casings, as shown in figures 10 and 31. When these casings were closed, sponge rubber compression discs backed by teflon inserts to prevent binding, exerted pressure against the tubes. This pressure held the tubes in place against their lightpipes where a layer of Dow-Corning silicone grease provided optical coupling.

2. Electronics

The electronics in the instrument can be conveniently catalogued into subsystems according to their location either on printed-circuit boards (PCB) in the electronics can or in external modules. Table I catalogs these subsystems.

QUALITY ASSURANCE DATA

SEMICONDUCTOR RADIATION DETECTORS

WARRANTY BASIS

Dote of shipment 9-30-64

Model No. TMHJ300-400

Seriol No. 4-30C

Active Areo 300 sq mm

Worronted Alpho Resolution

no more thon 80.0 Kev FWHM[1]

*(Meosured resolution 29.4 Kev FWHM)

Noise Width 22.9 Kev FWHM[2]

Depletion Depth 426 microns

Obtoined ot 130 volts bios

Above depletion depth will totolly

obsorb α porticles up to 30.25 Mev

β porticles up to .367 Mev

protons up to 7.75 Mev

Nominol Resistivity 25,000 ohm-cm

SUBSIDIARY ELECTRICAL MEASUREMENTS

BIAS VOLTAGE VOLTS	REVERSE CURRENT μa	NOISE WIDTH KEV FWHM
0	0	
200	.73	22.9

Detector performonce under conditions, other than that of the warranty basis con be inferred from the obove doto.

NOTES:

* 1. Alpho Resolution is the full-width ot half-moximum (FWHM) of o 5.5 Mev thin Am^{241} olpho source spectrum line, measured with detector ond source in vocuum, with stoted bios voltoge, ond includes the noise contribution of on ORTEC Model 101-201 Amplifier System.
2. Noise Width is the FWHM of o precision pulse generotor line spectrum (from ORTEC Model 204) with detector connected os o noise source to input of ORTEC Model 101-201 Amplifier System, ond ot stoted bios voltoge. Noise width is generolly somewhot less thon olpho resolution, ond is very nearly equol to beto or proton resolution for totolly obsorbed porticles.

WARRANTY TERMS

Detectors ore guoronteed to meet the minimum specificotions of the worronty bosis doto obove for o period of 12 months from dote of shipment if used in coreful loboratory conditions os outlined in the ORTEC Detector Instruction Manuol. Foulty detectors will be repoired or reploced ot ORTEC option. No consequentiol liobility for molfunction beyond soid repoir or replocement con be ossumed.

GENERAL SPECIFICATIONS

1. All detectors ore operoted in excess of 12 hours in vocuum of 10^{-6} mm of Hg before toking doto shown.
2. Surfoce borrier type detectors hove o front surfoce dead loyer no greoter thon thot corresponding to 20 Kev energy loss from o 5.5 Mev olpho.

Special Test Data:

Front deadlayer

Back deadlayer

Bias Thru Out at 130 V

Doto certified by J. Carden

Oak Ridge Technical Enterprises Corporation

P.O. BOX C, OAK RIDGE, TENN. PHONE 483-8451

FORM M-04262

Figure 29. ORTEC Quality Assurance Data for Detector 1

PULSE HEIGHT	90% OF STILBENE
DECAY CONSTANT	4×10^{-9} SEC.
WAVELENGTH MAXIMUM EMISSION	4165 Å
DENSITY	1.04 G/CC
COLD FLOW TEMP.	70° C
BASE	POLYSTYRENE
COLOR	WATER CLEAR
TRANSMISSION AT MAX. WAVELENGTH	99.5 % PER INCH
SOLUBILITY	INSOLUBLE IN WATER AND LOWER ALCOHOLS
DAYLIGHT FLUORESCENCE	BLUE

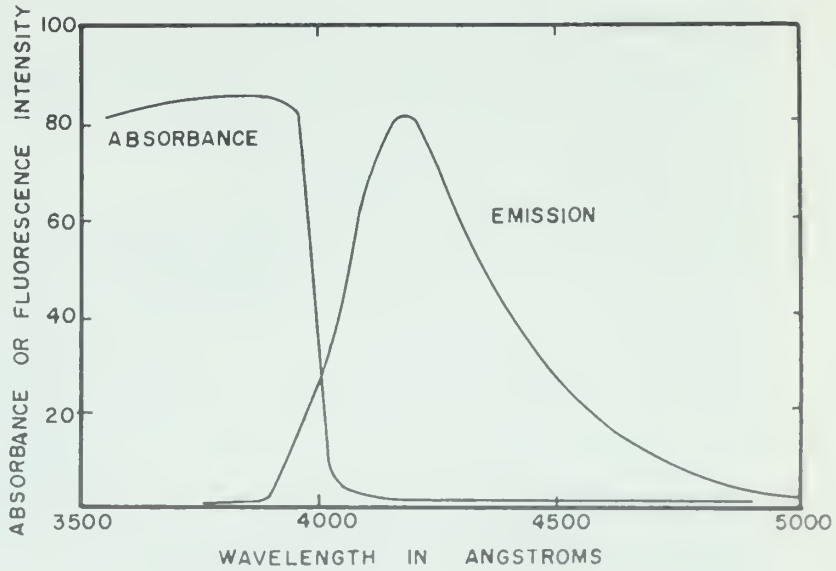

Figure 30. Properties of SC-700

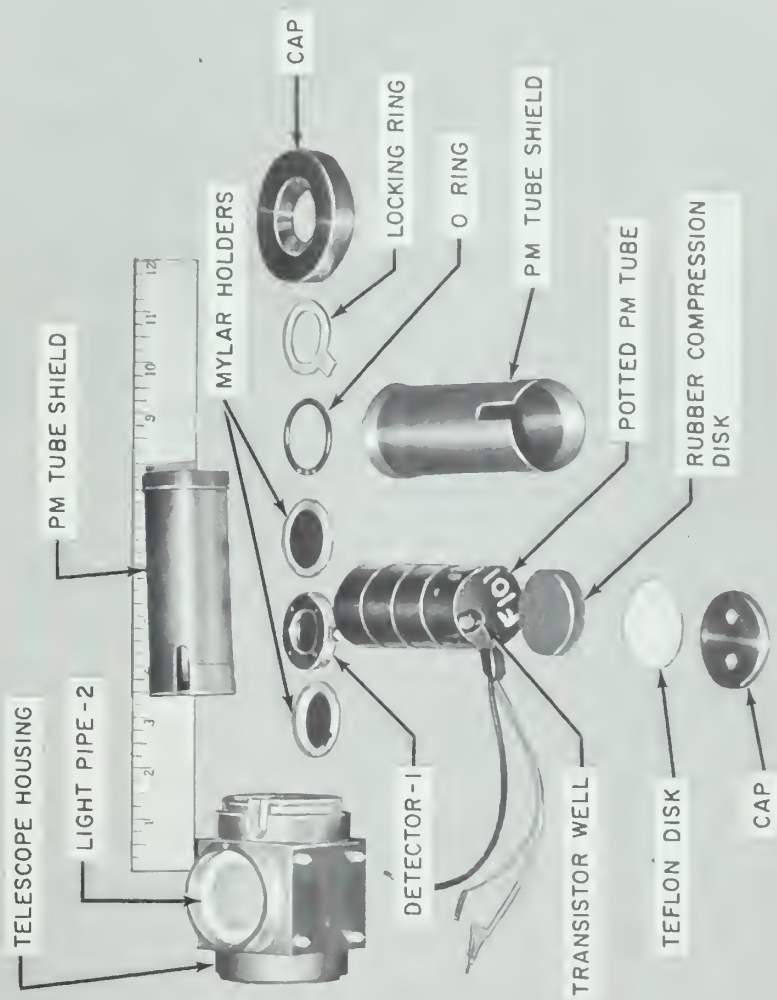

Figure 31. Telescope Components

Table I

CATALOG OF ELECTRONIC SUBSYSTEMS

Subsystem	Functional label	Location
1	Particle Identification Gates	PCB 1
2, 4, 6	Scalers	PCB 2, 4, 6
3	Pulse-Height Analyzer (5 channels)	PCB 3
5	Pulse-Height Analyzer (3 channels)	PCB 5
7	Amplifier Isolation Shield	PCB 7
8	Amplifiers	PCB 8
9	High-Voltage Supply	Module
10, 11	Photomultiplier Subsystems	Modules

The first eight subsystems were mounted on fiberglass printed-circuit boards of dimensions ~9-1/2 in. x 3-3/4 in. x 1/16 in. These boards, shown vertically in figure 32, were held in grooves under compression exerted by sponge-rubber backing on the filigreed plastic sheets which formed the floor and roof liners for the electronics can. The technique of assembly is shown in figure 33. In this figure, the numbering of the printed-circuit boards, and hence the subsystem numbers, start on the left. The numbering increases from left to right. The last three subsystems were located in modules external to the electronics can.

All subsystems will now be described in detail. For clarity they will be discussed in the order most convenient for following the flow of signal information.

a. Subsystems 10 and 11 were photomultiplier subsystems. Each modular system consisted of an RCA type 6649 photomultiplier tube, its tube-base circuitry (figure 11), and a protective tube casing. The layout of the components for the printed-circuit boards which were attached to the tube base is shown in figure 34. To prevent corona or high-voltage breakdown, the tube bases were potted.

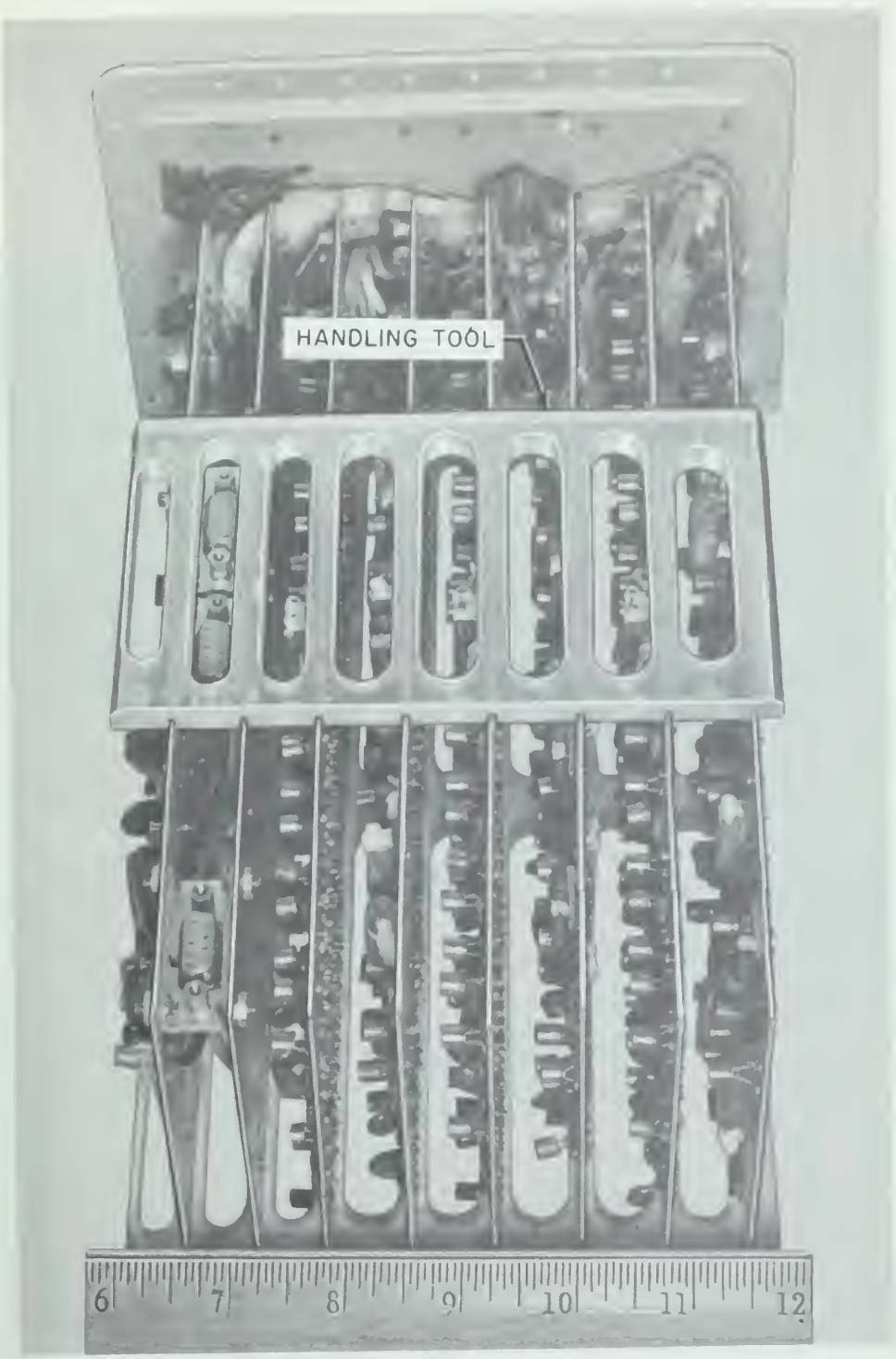

Figure 32. The Electronics Drawer (Top View)

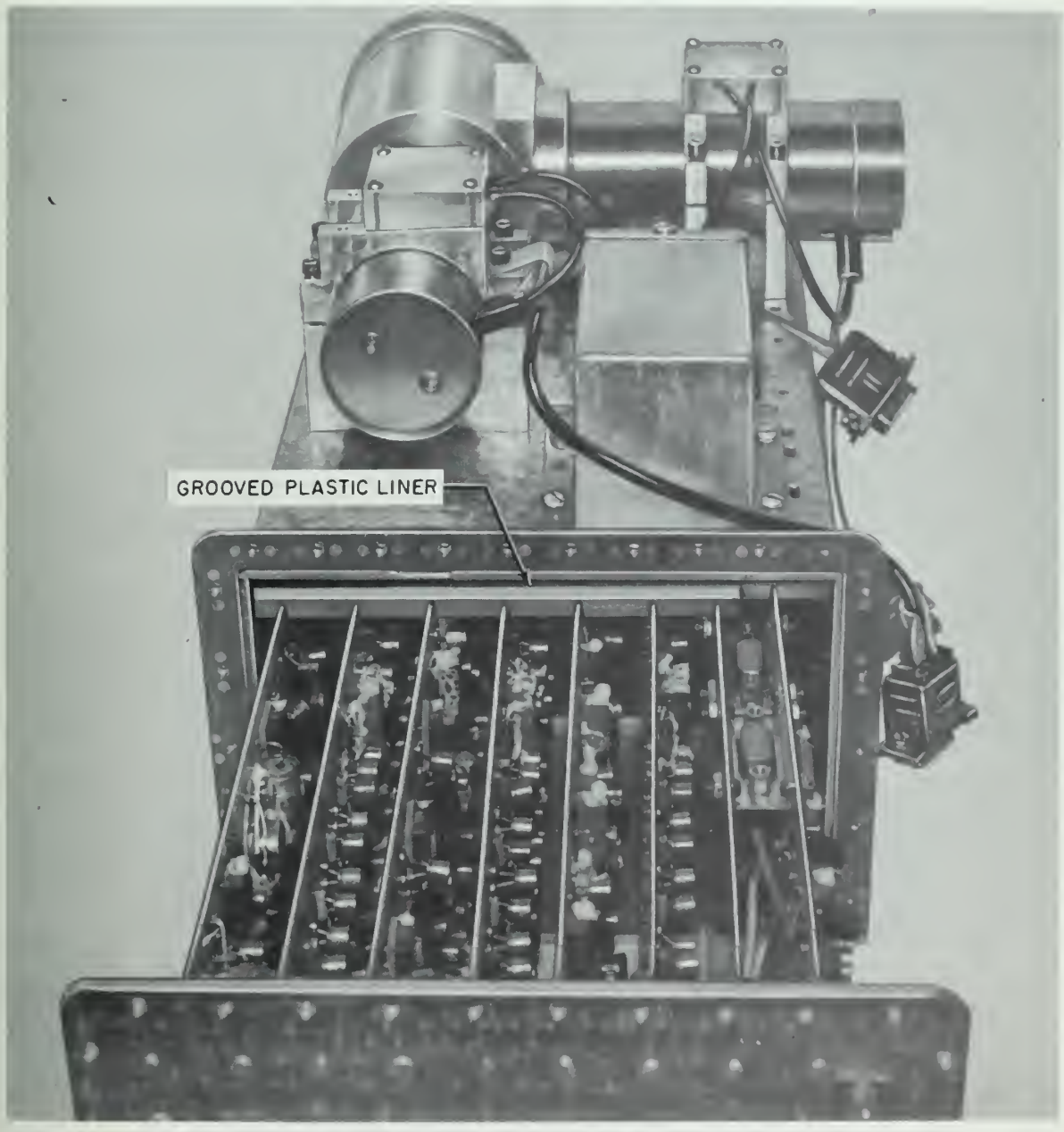

Figure 33. Instrument During Assembly

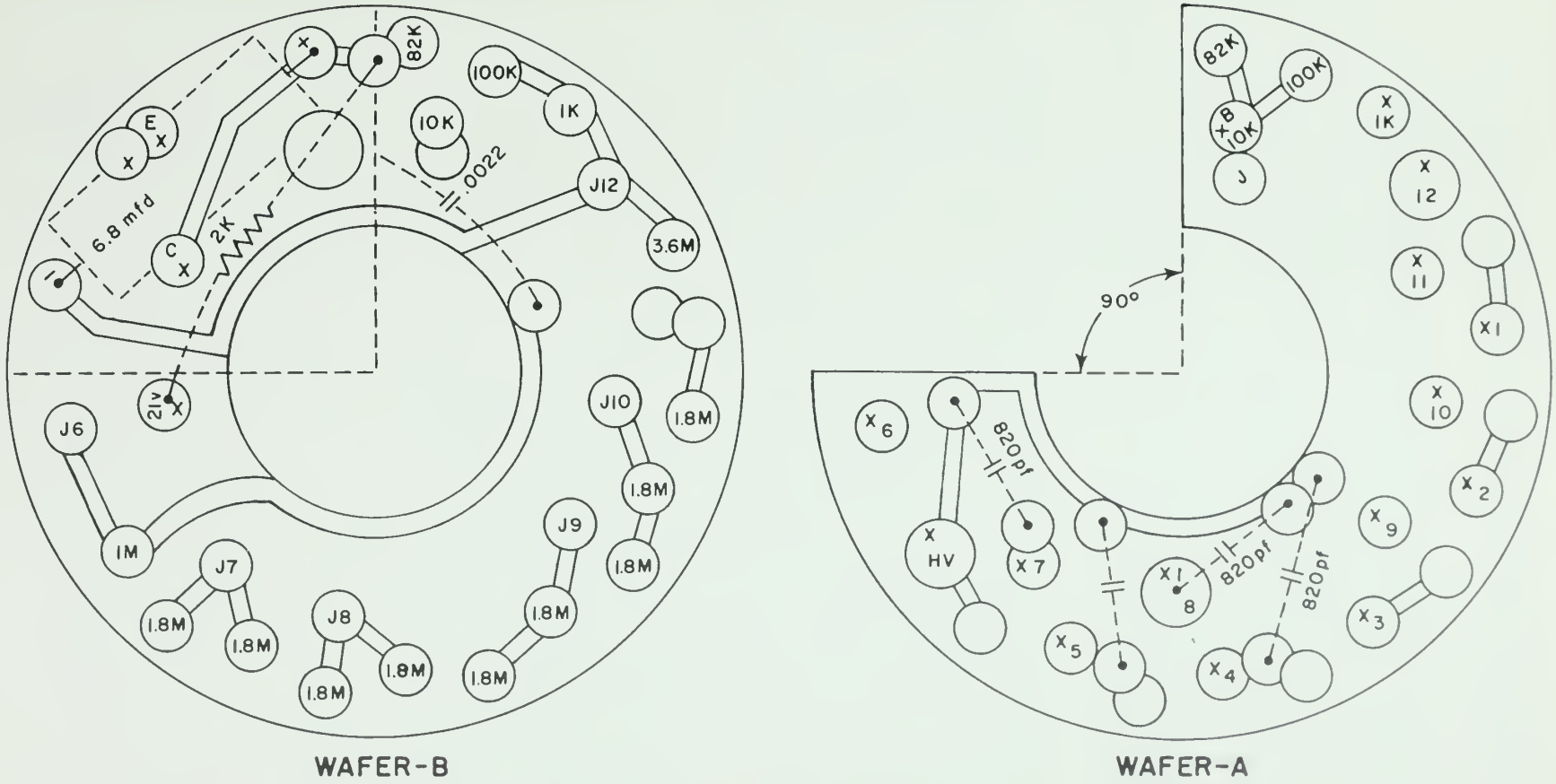

Figure 34. Photomultiplier PCB Layout

A completely potted tube with its casing and inserts is shown in figure 31.

b. Subsystem 9 was a modular box-like can which housed the high-voltage power supply. The circuitry is shown in figure 24. The layout of the components on the printed-circuit boards in the module is shown in figure 35. Figure 36 is a view of the circuitry during insertion into the aluminum can prior to potting.

To prevent corona or high-voltage breakdown, the high-voltage module was completely potted with Epocast 502 with 951 hardener (Furane Plastics, Inc.).

c. Subsystem 8 consisted of a charge-sensitive amplifier, two other amplifiers, and their regulated power supplies. For ease of reference, these circuits, which were discussed separately in section II, have been combined as a complete subsystem in figure 37. This subsystem was mounted on PCB 8. The physical appearance of PCB 8 and its associated copperclad isolation shield PCB 7 is illustrated in figure 38 where they are the two foremost boards. The layout of components on PCB 8 is shown in figure 39.

d. Subsystem 5 consisted of a three-channel pulse-height analyzer (PHA 1), Readout Squelch Gate 1, and the three count-rate meters which registered in telemetry channels TM1, TM2, and TM3. PHA 1 was driven by the low-gain stage of the charge-sensitive amplifier of Detector 1. The complete subsystem is shown in figure 40. This entire subsystem was mounted on PCB 5 as illustrated in figure 41. The layout of components on PCB 5 is shown in figure 42.

e. Subsystem 3 consisted of a five-channel pulse-height analyzer (PHA 2) and Readout Squelch Gate 2. PHA 2 was driven by both stages of the amplifier for Detector 2. (PHA 2 furnished negative signals as outputs to drive five scaling circuits.) Subsystem 3 circuits, which were discussed separately in section II, are combined as a complete subsystem in figure 43. This subsystem was mounted on PCB 3. Its physical appearance is illustrated in figure 44. The layout of components on PCB 3 is shown

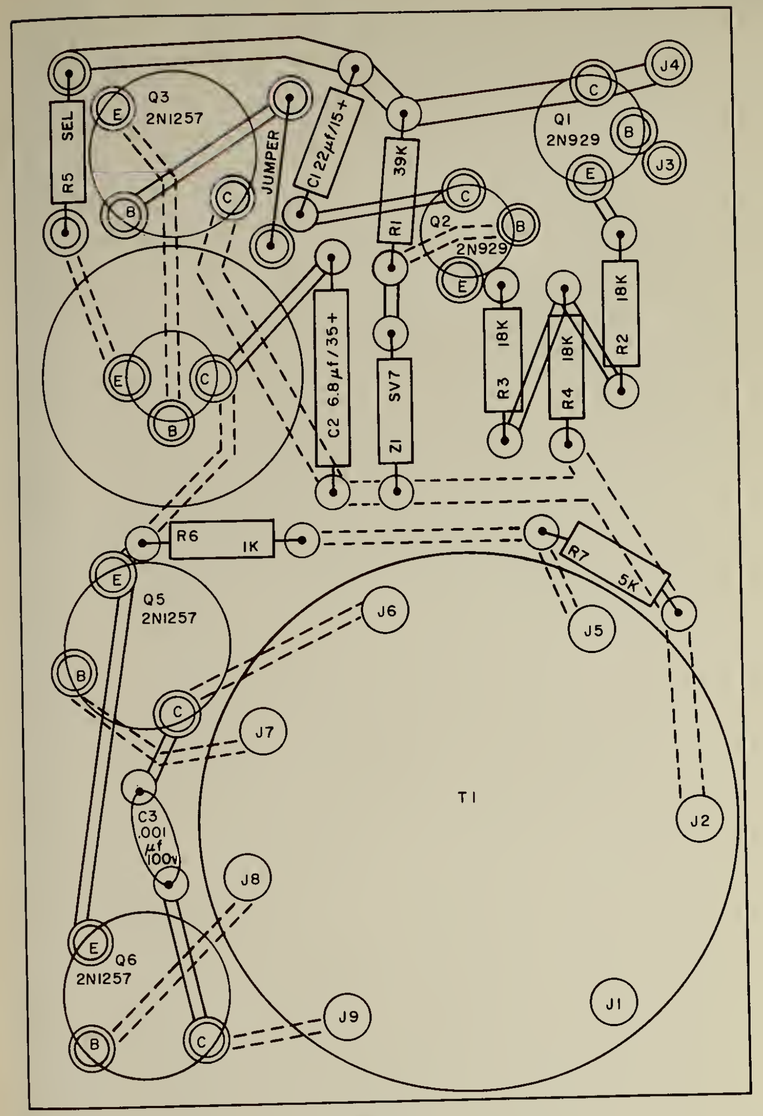

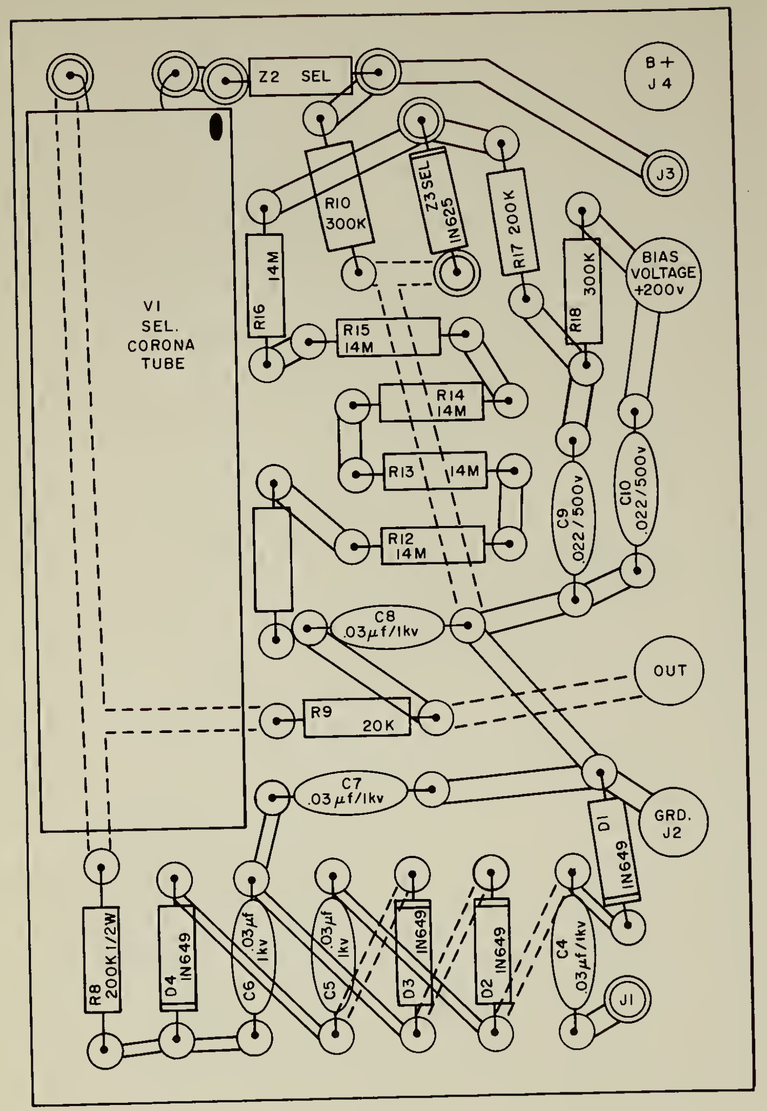

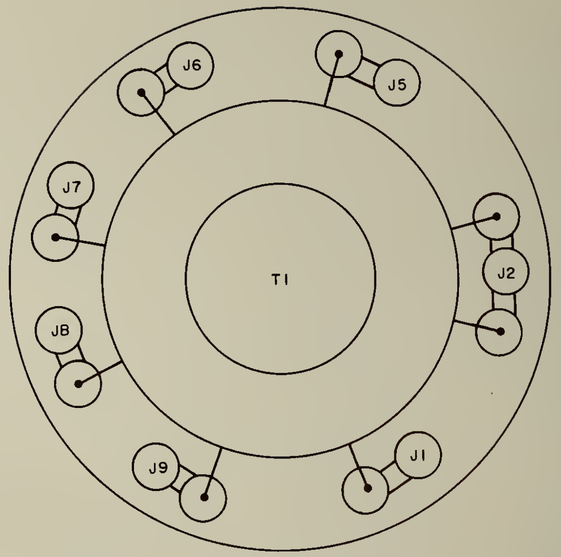

Figure 35. DC/DC Converter PCB Layouts

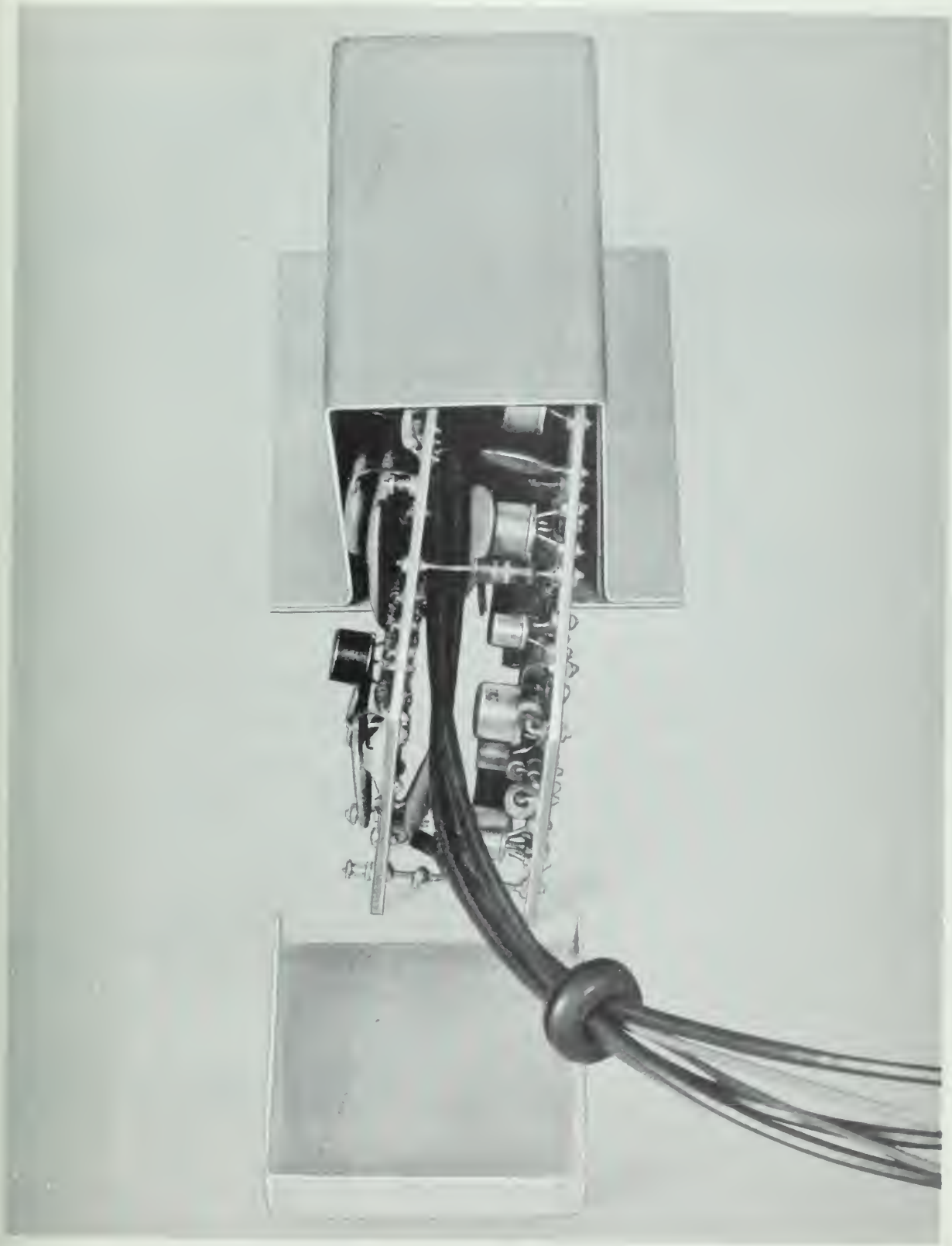

Figure 36. DC/DC Converter Module (Before Potting)

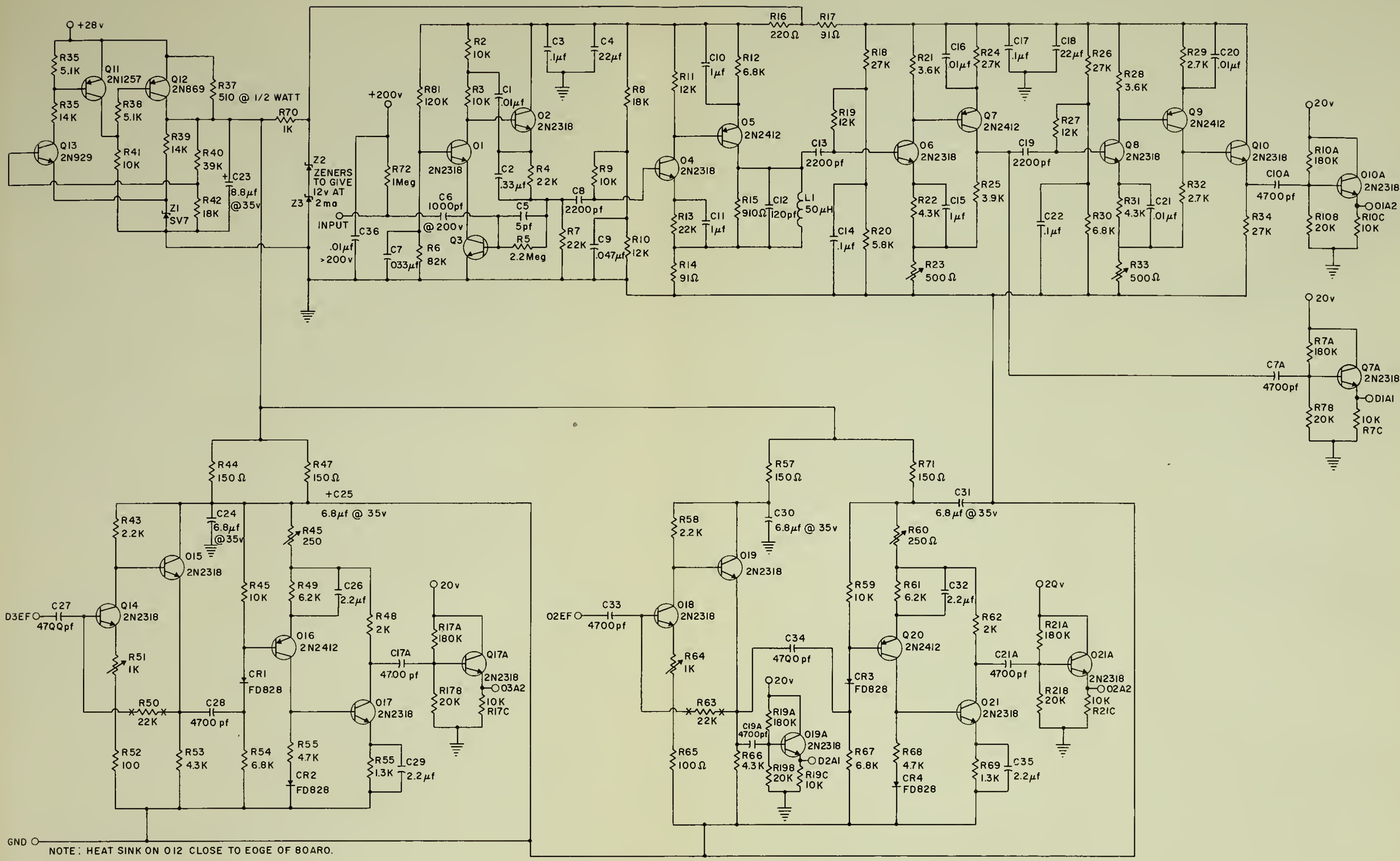

Figure 37. Subsystem 8 Circuitry

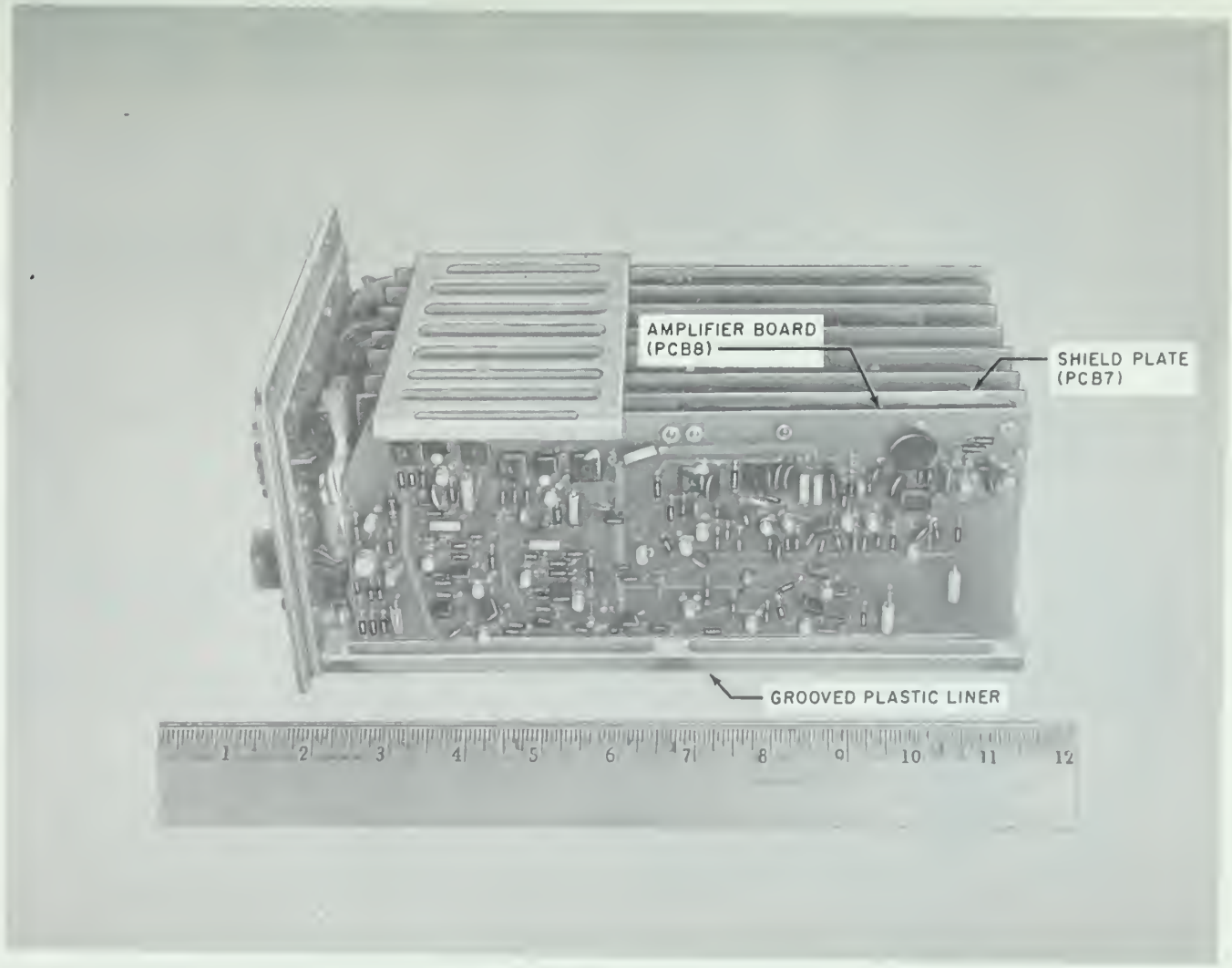

Figure 38. The Electronics Drawer (Side View)

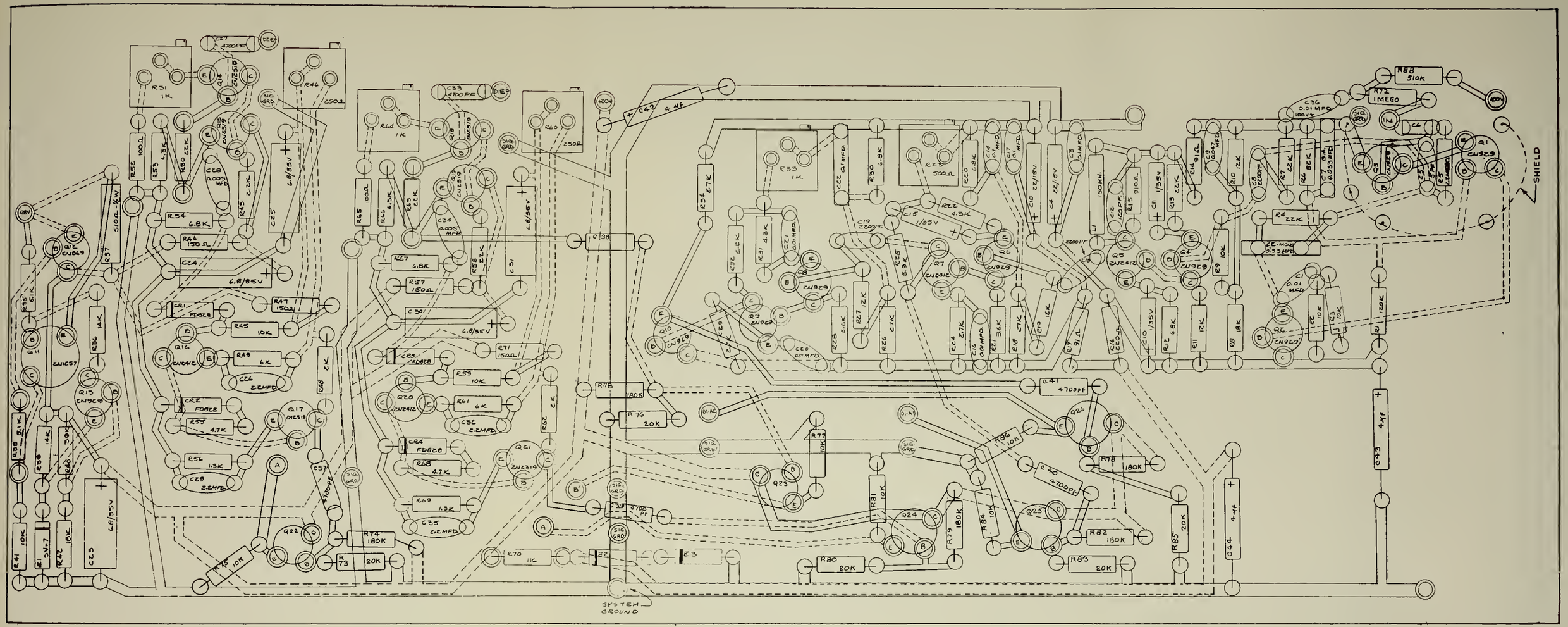

Figure 39. PCB 8 Layout

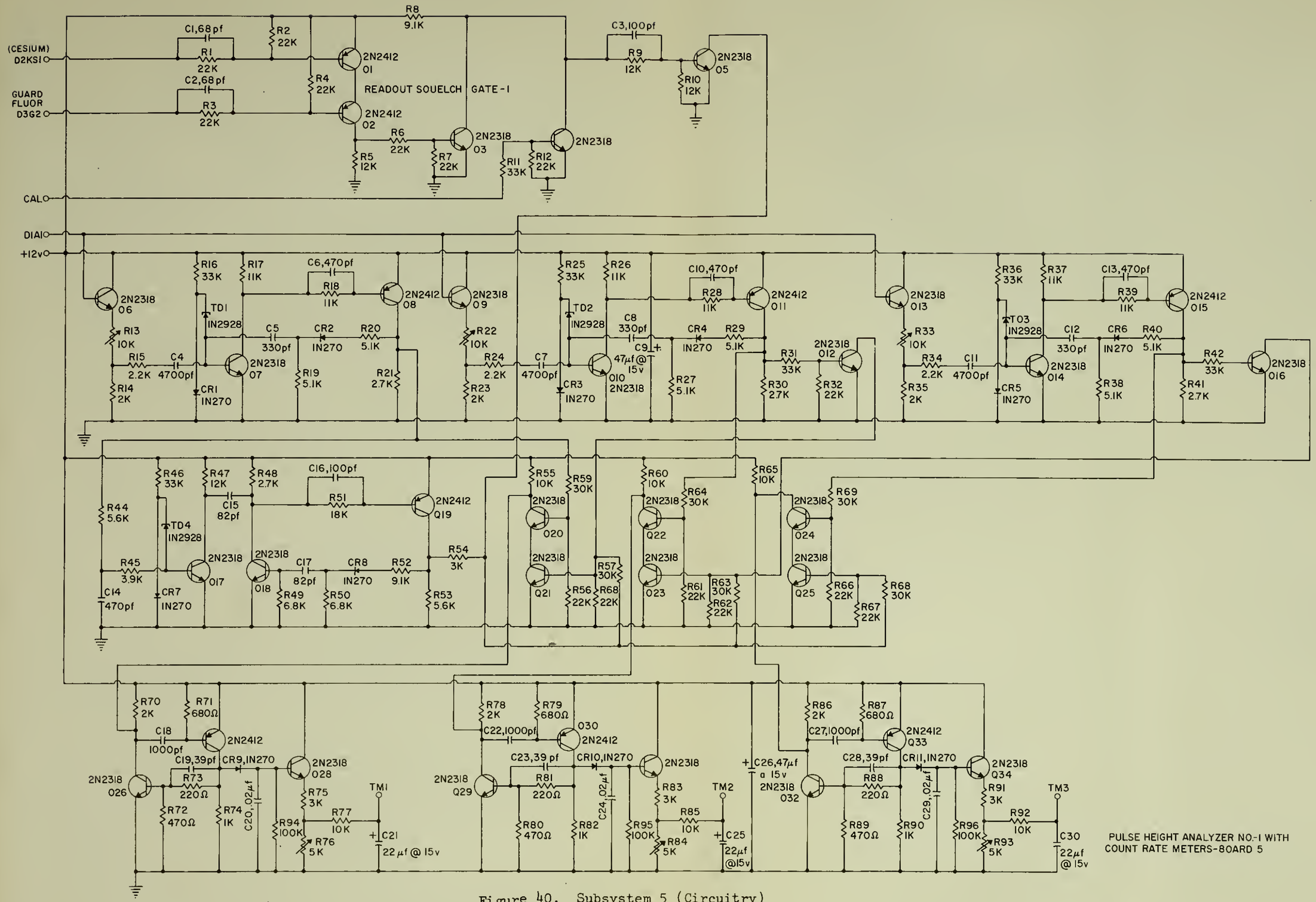

Figure 40. Subsystem 5 (Circuitry)

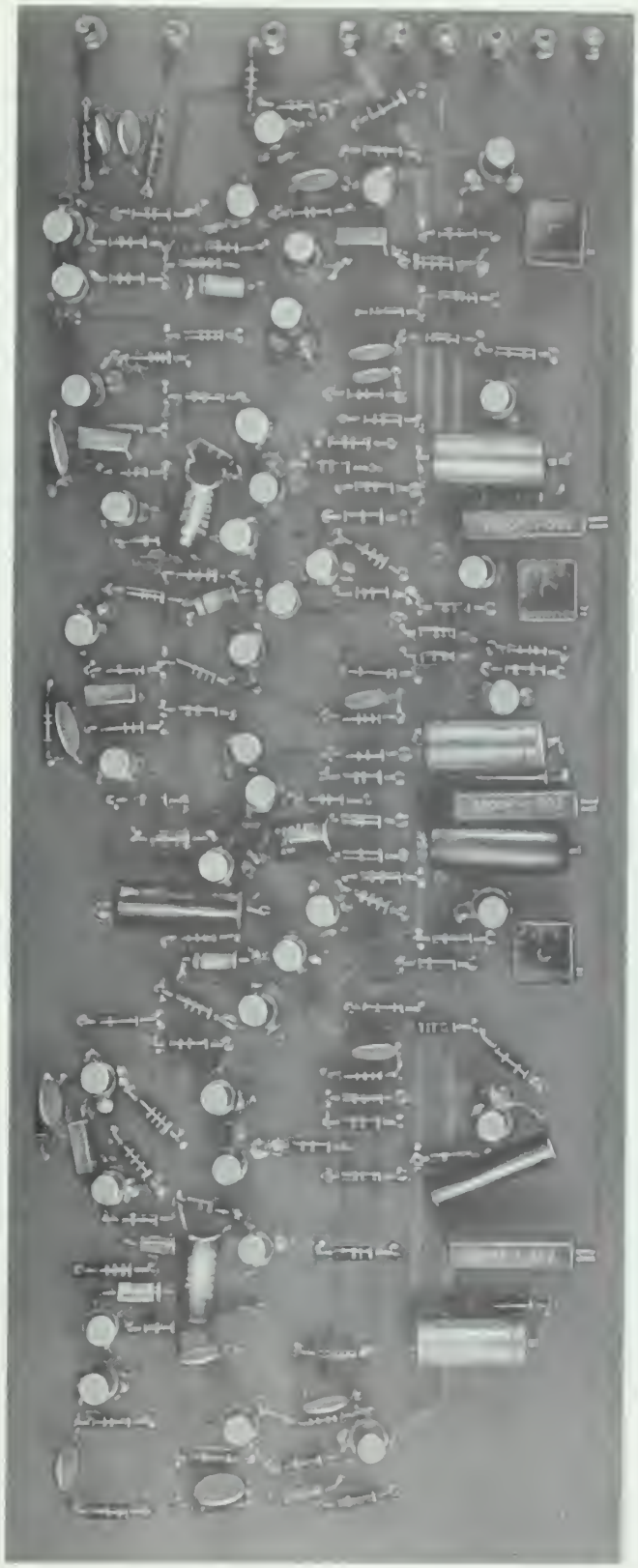

Figure 41. PCB 5

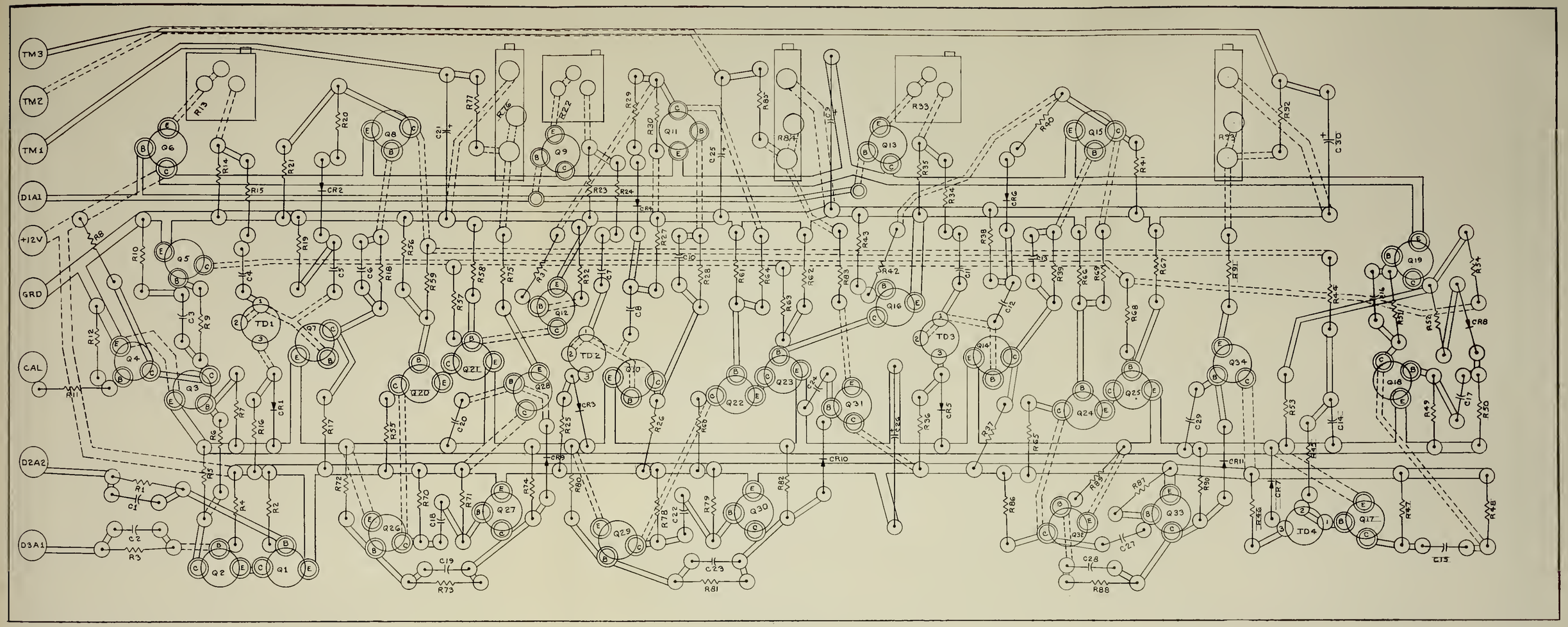

Figure 42. PCB 5 Layout

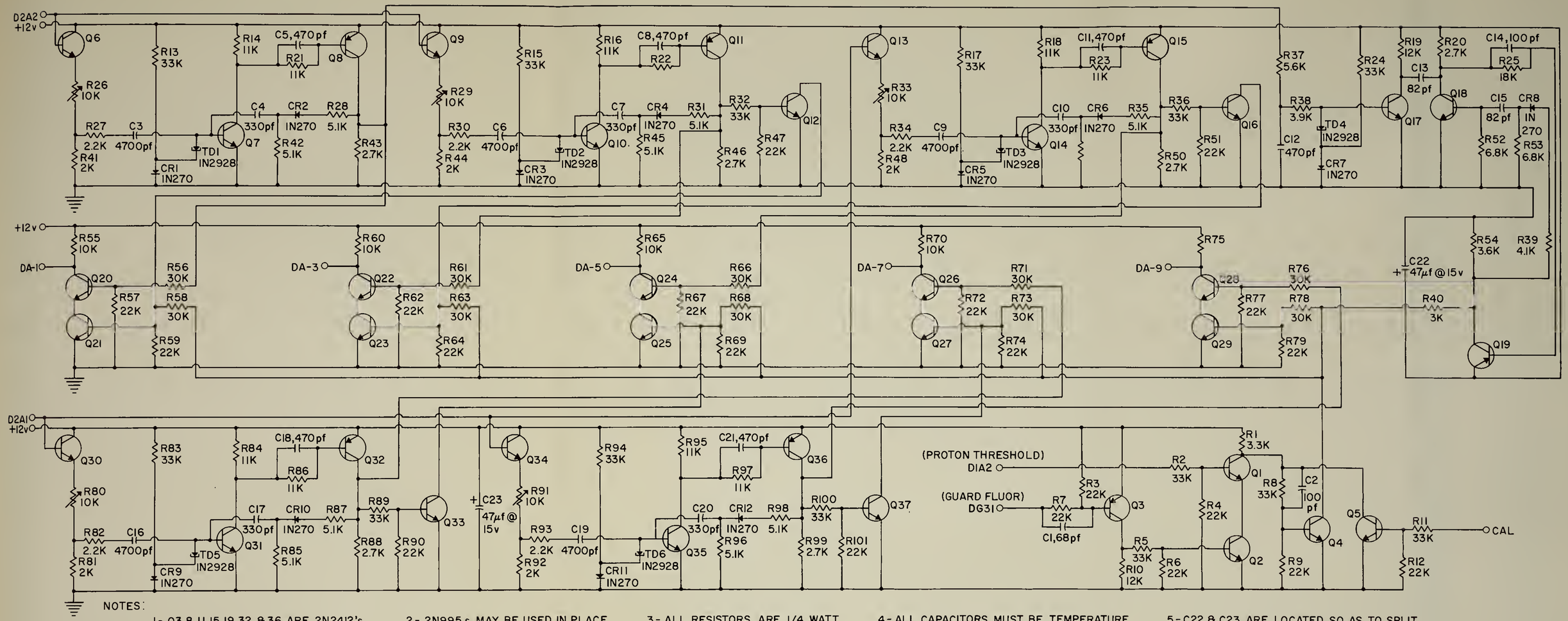

NOTES:

1- Q3,8,11,15,19,32,& 36 ARE 2N2412's, ALL OTHERS ARE 2N2318's.

2.- 2N995's MAY BE USED IN PLACE OF 2N2412's.

3.- ALL RESISTORS ARE 1/4 WATT.

4.- ALL CAPACITORS MUST BE TEMPERATURE STABLE WITHIN 10% FROM -15C TO +85C.

5.- C22 & C23 ARE LOCATED SO AS TO SPLIT THE B+ LINE INTO 3 EQUAL PARTS.

Figure 43. Subsystem 3 Circuitry

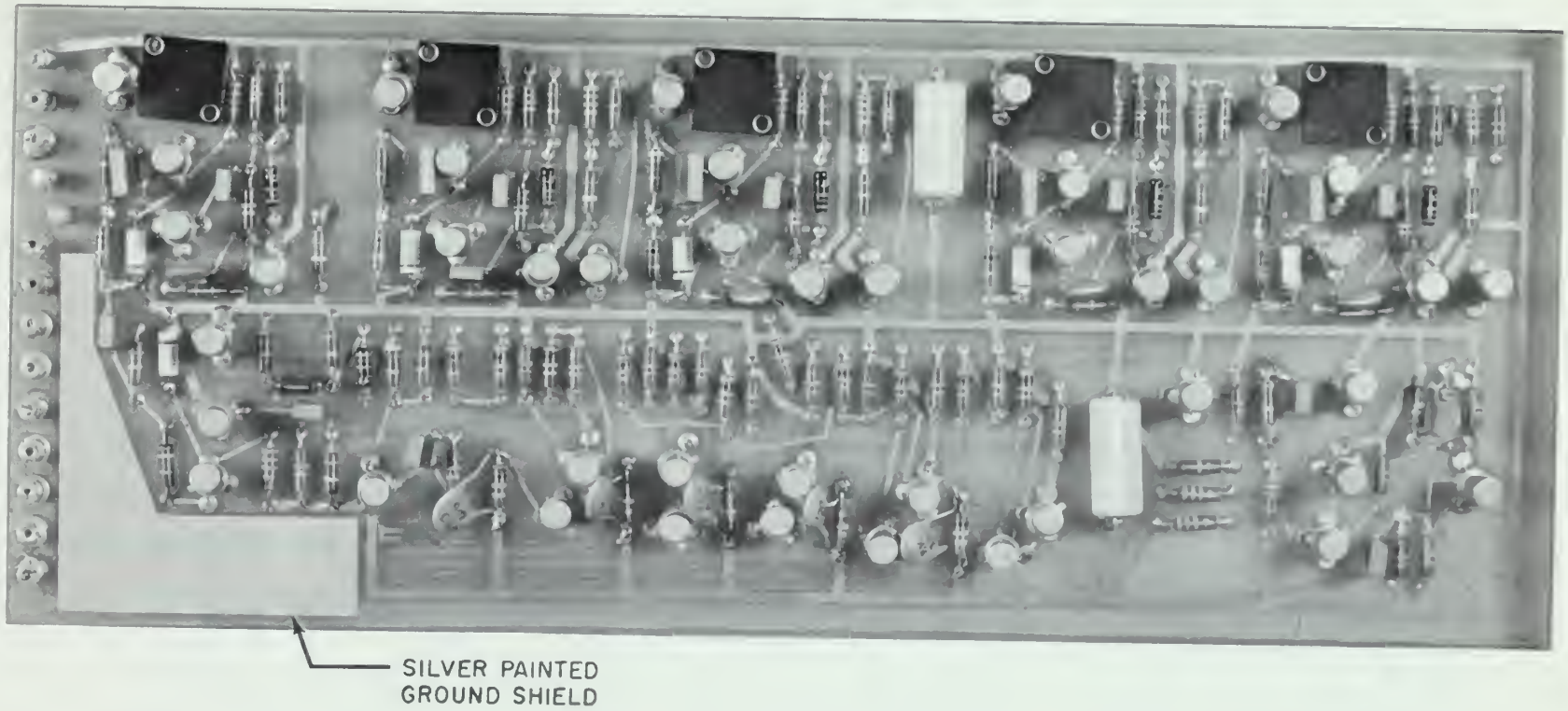

Figure 44. PCB 3

in figure 45.

f. Subsystems 2, 4, and 6 were dual-channel 5-bit flip-flop binary scalers. This typical scaler circuit was discussed in section II (figure 19). Five of the six scaling circuits received negative inputs from PHA 2. They registered their outputs in telemetry channels TM4 through TM8. These scaling circuits were mounted, two circuits on a board, to form three subsystems. The physical appearance of one such typical board is shown in figure 46. The layout of components on such a typical board is shown in figure 47.

g. Subsystem 1 was composed of particle-identification circuitry, the High-Energy Gate, two count-rate meters, and a voltage regulator to provide an operating voltage of 12 volts d.c. for analyzing circuitry other than amplifiers. The electrical diagram of this subsystem is shown in figure 48. The particle-identification circuitry consisted of two standardized tunnel-diode discriminators set to thresholds that formed a response band 260 kev wide. Because of detector characteristics, if a particle deposits more than 550 kev in Detector 1, it can be assumed to be a proton. Likewise, an energy deposit of less than 550 kev may be assumed to be a very low-energy proton or conversely an energetic electron (above 400 kev) or an energetic proton (above 110 Mev). These particle-identification discriminators act upon the High-Energy Gate (Q11/Q12) in the manner discussed in section II. The negative output of this High-Energy Gate is sent to the remaining sixth scaling circuit and thence registered in telemetry channel TM9. The two count-rate meters (Q7 and Q24), respectively, register the composite counting rates of Detectors 1 and 2 in telemetry channel TM10 and the counting rate of Detector 3 in telemetry channel TM11. The physical appearance of PCB 1 is shown in figure 49. The layout of components on PCB 1 is shown in figure 50.

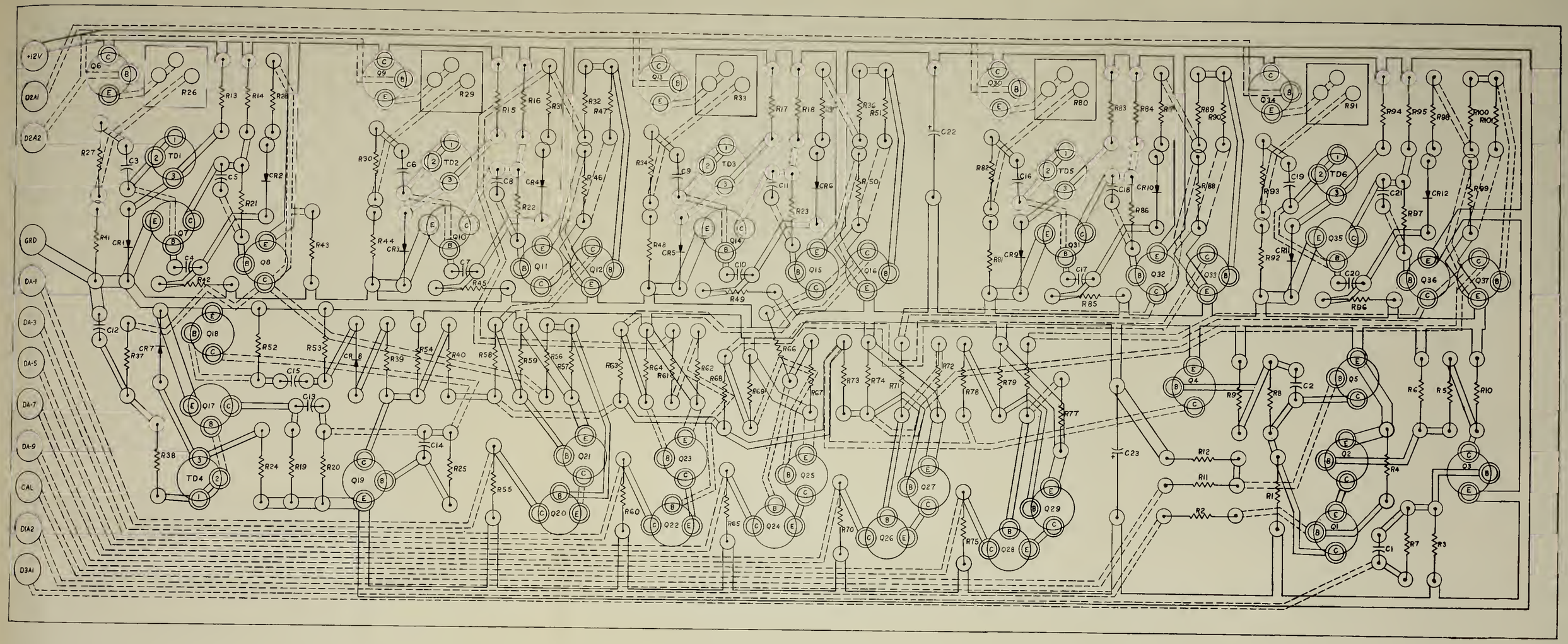

Figure 45. PCB 3 Layout

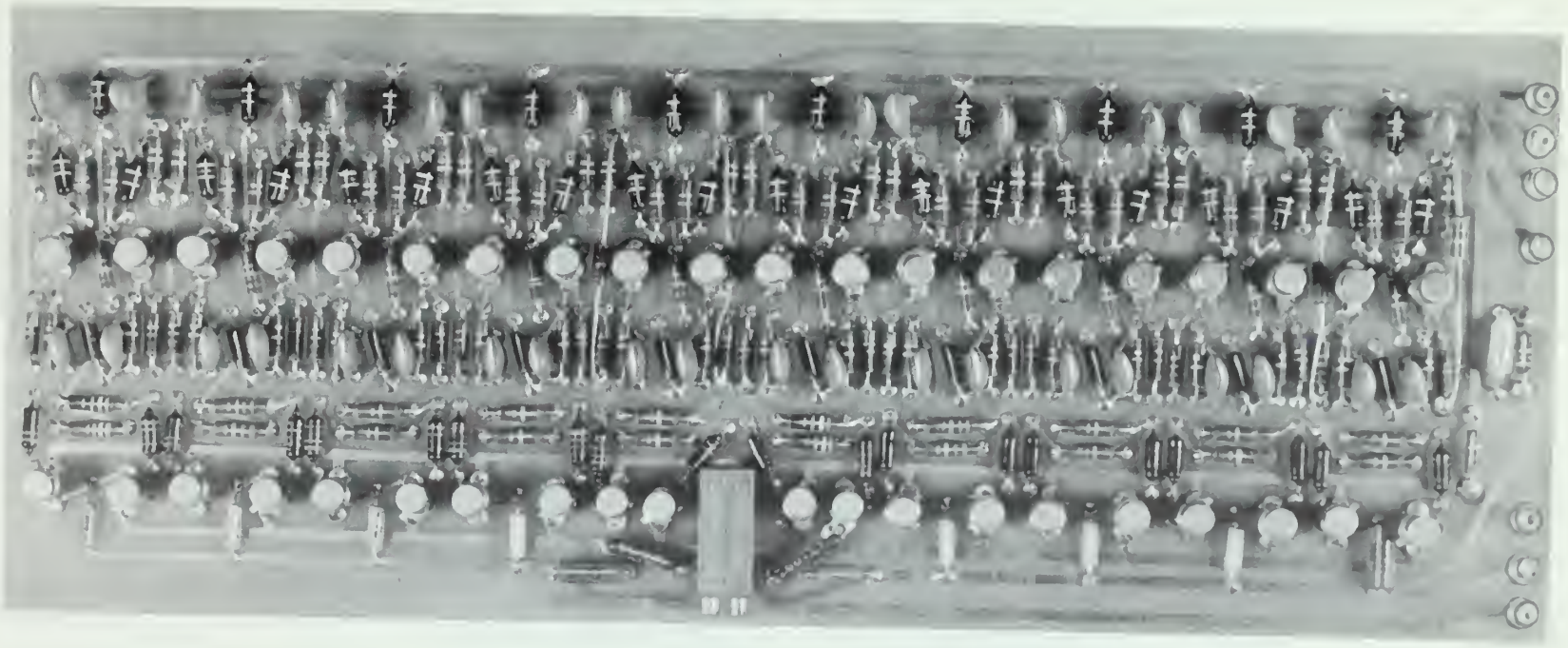

Figure 46. Typical Scaler PCB (PCB 2, 4, and 6)

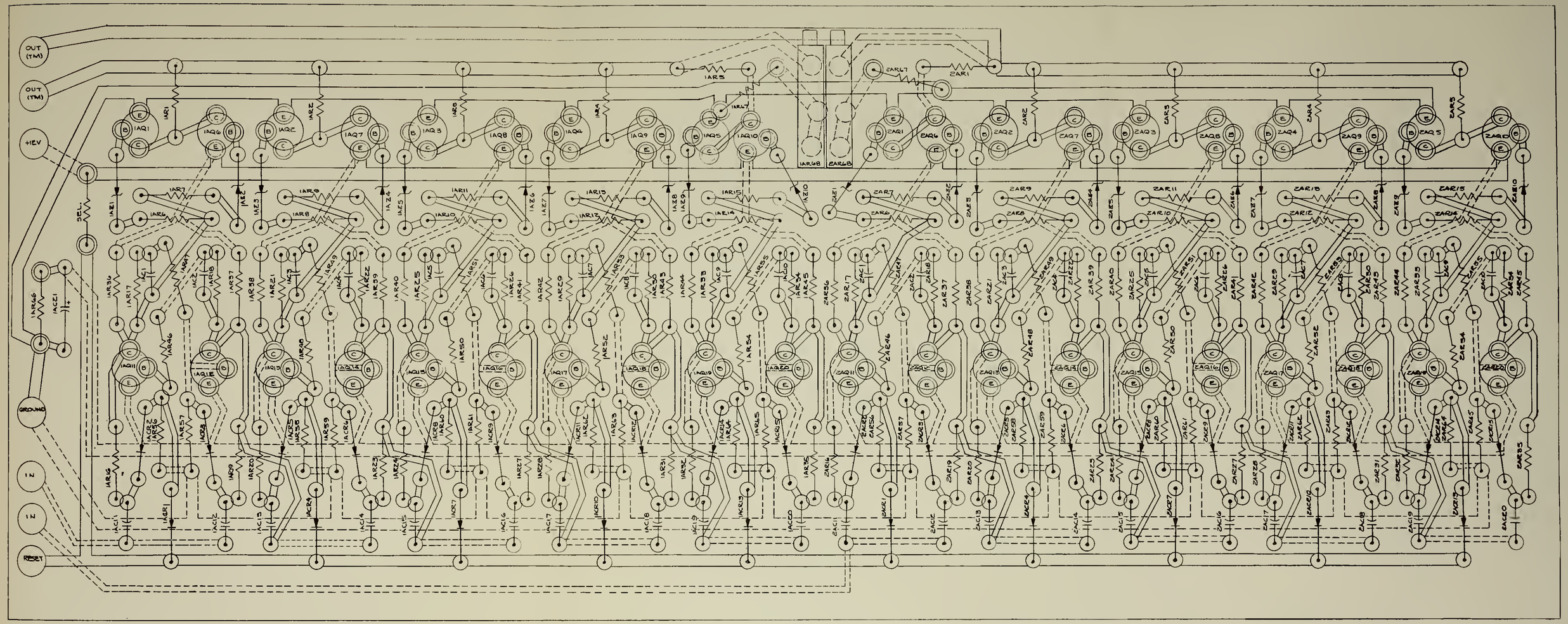

Figure 47. Typical Scaler PCB Layout (PCB 2, 4, and 6)

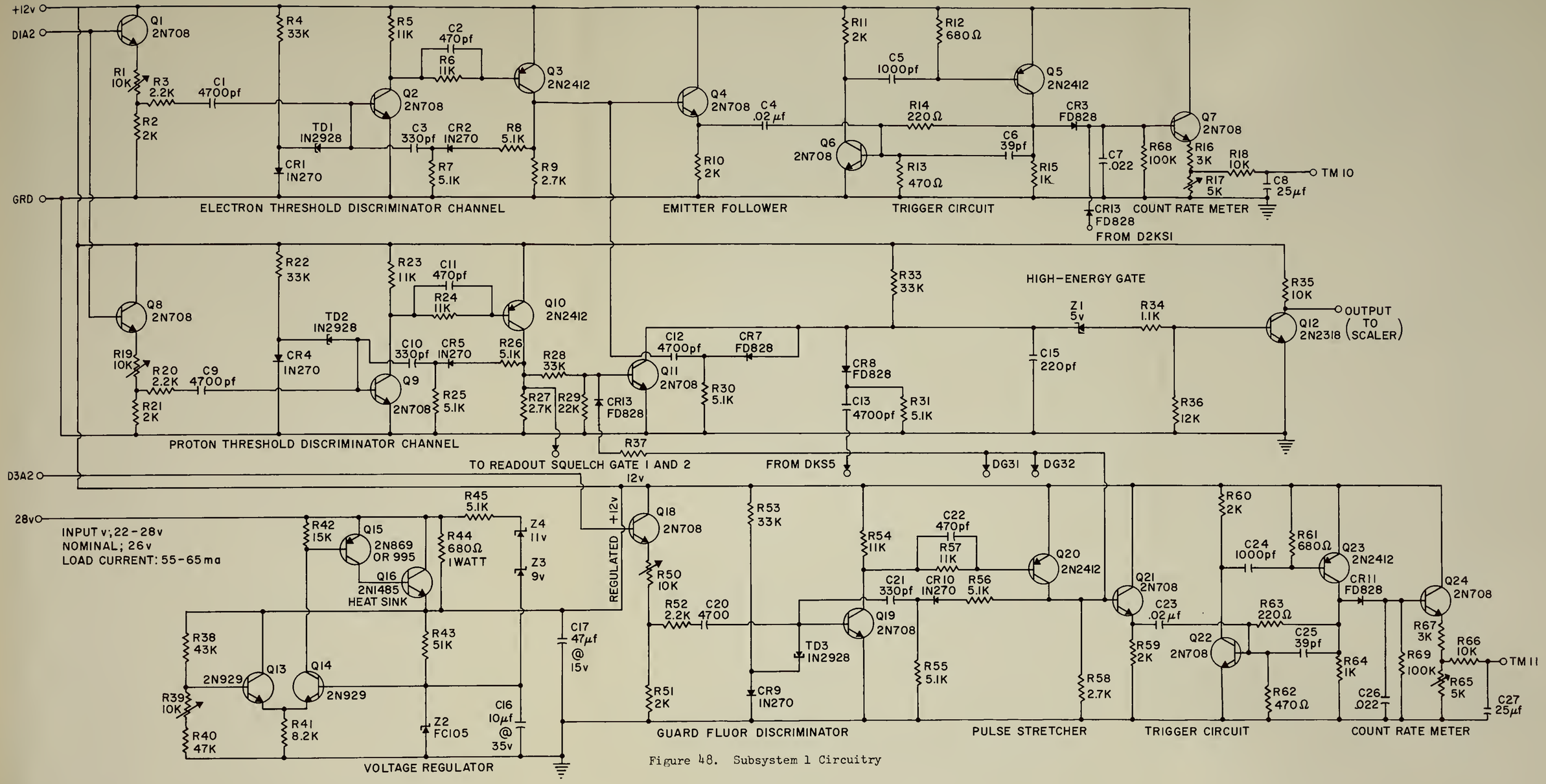

Figure 48. Subsystem 1 Circuitry

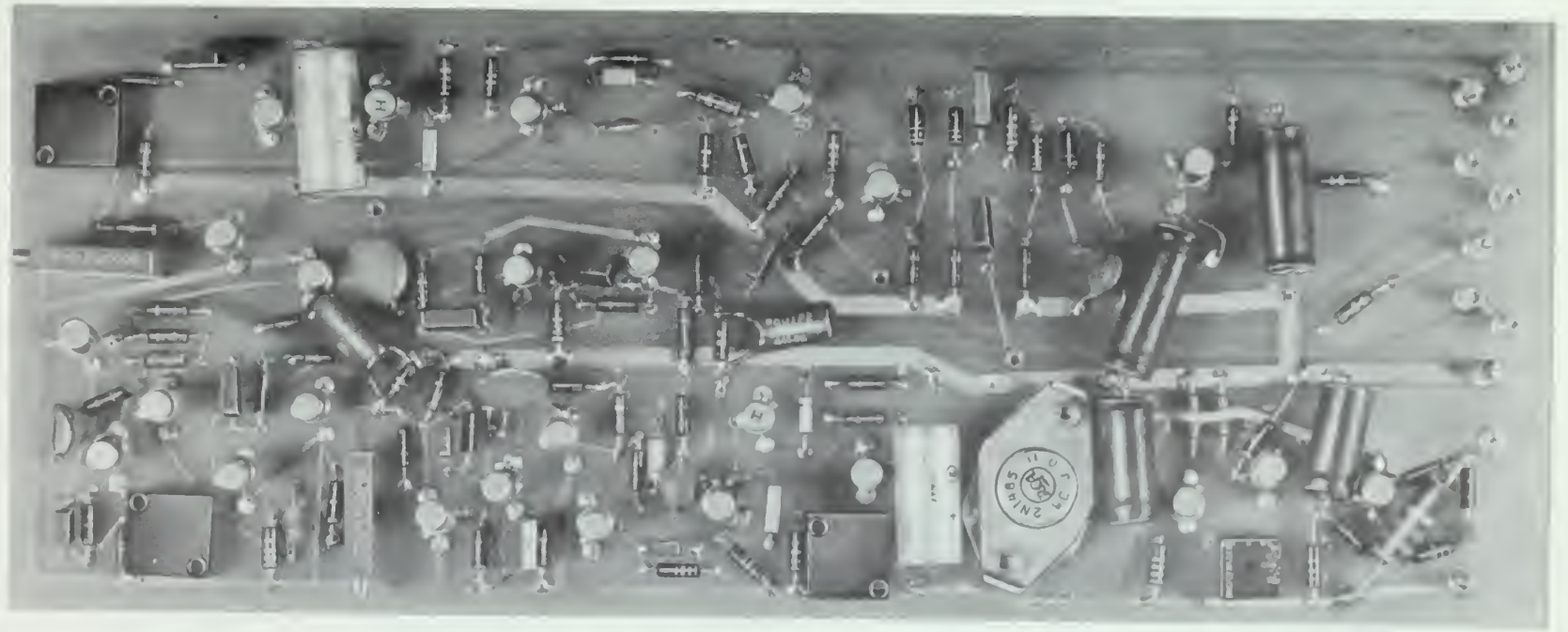

Figure 49. PCB 1

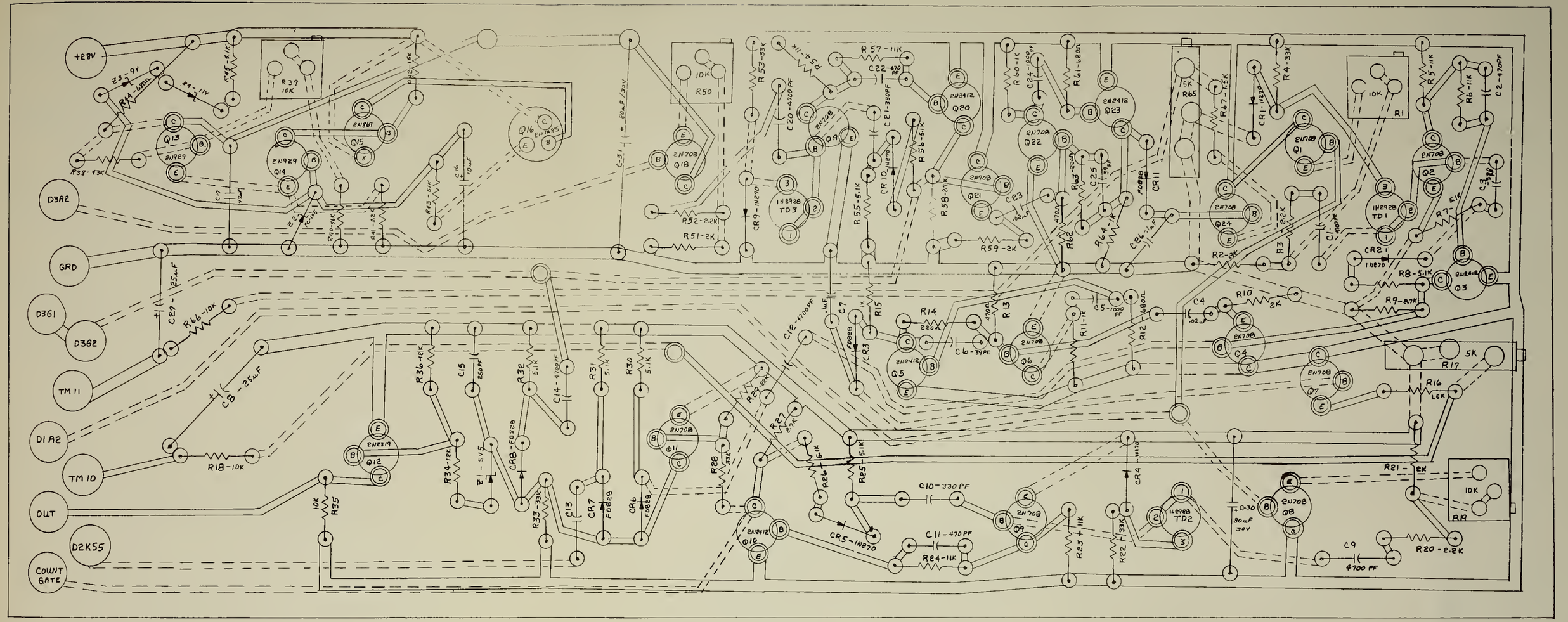

Figure 50. PCB 1 Layout

3. Electrical Interconnections

The electrical interconnections between subsystems are shown in figure 51. The following generalizations apply to this wiring diagram:

a. Microdot cables were used for all interconnections carrying signals before pulse-height discrimination. All cable shields were grounded at a point close to the origin of the signal.

b. Shielded wires were used for all interconnections carrying other information, e.g., inputs to the scaling circuits and 12-volt operating voltages. All wire shields were grounded to the case at a point close to the origin of the information.

c. Insulated, but unshielded, high-voltage cables were used for short high-voltage runs. They were used for leads (less than four inches) from the high-voltage supply to the photomultiplier tubes and to the bias-supply junction on PCB 8. The final four inches of the bias-supply run to Detector 1 used Microdot coaxial shielded cable since it also carried signal responses.

The physical appearance and routing of these interconnections can be seen in figures 32 and 38. Three Cannon 9-pin connectors can also be seen cradled between PCB 7 and PCB 8. These connectors facilitated disassembly of the flight package for system checkouts, tests, and calibrations before flight.

4. Mechanical Interconnections

The mechanical interconnections discussed in this section can be seen in figures 10, 32, 33, and 52. For ease in considering these mechanical interconnections, the instrument can be divided into the following structural subunits:

a. The electronics can

b. The electronics drawer

c. The high-voltage supply module

d. The telescope

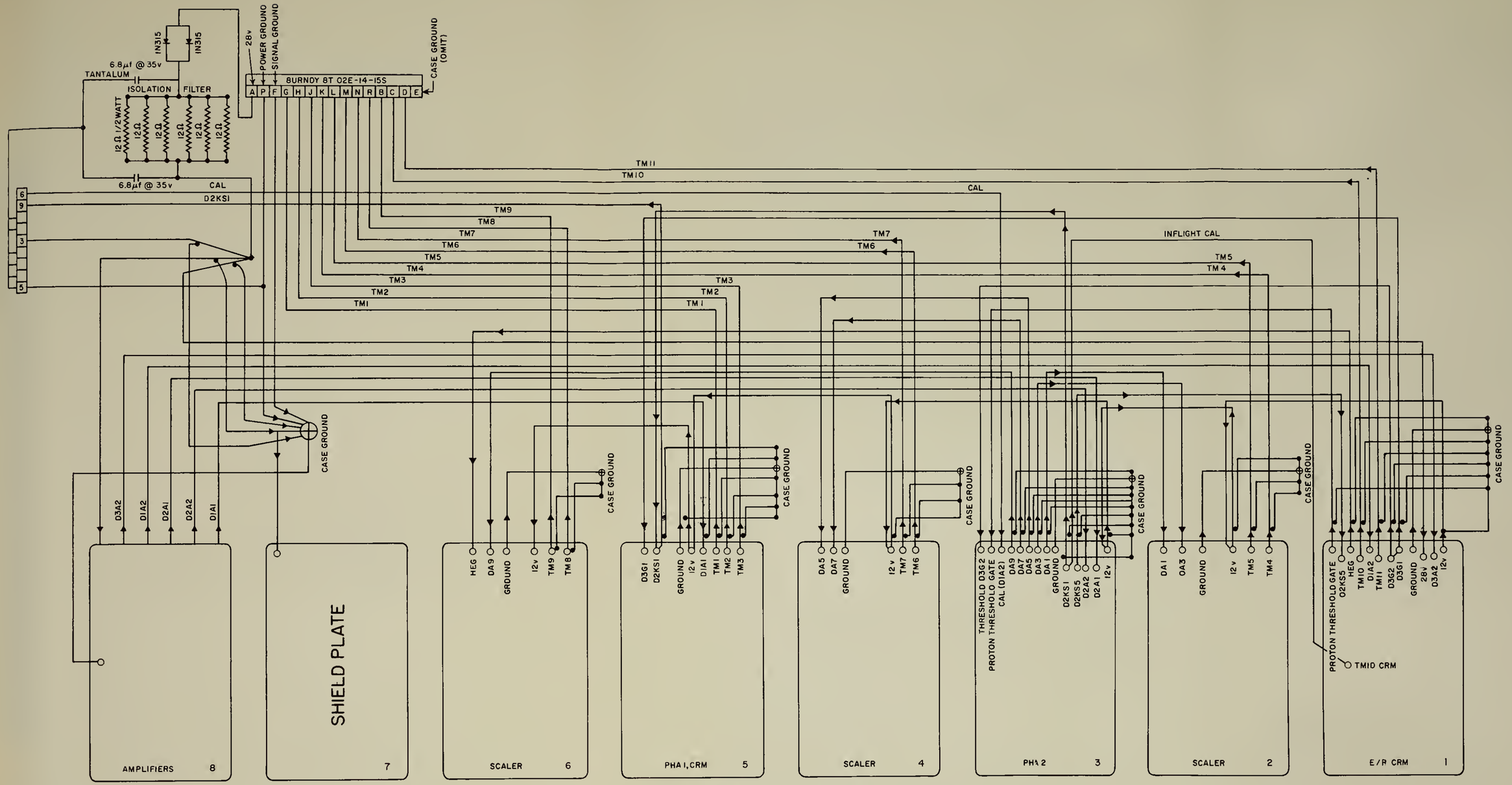

Figure 51. Wiring Diagram (Subsystem Interconnections)

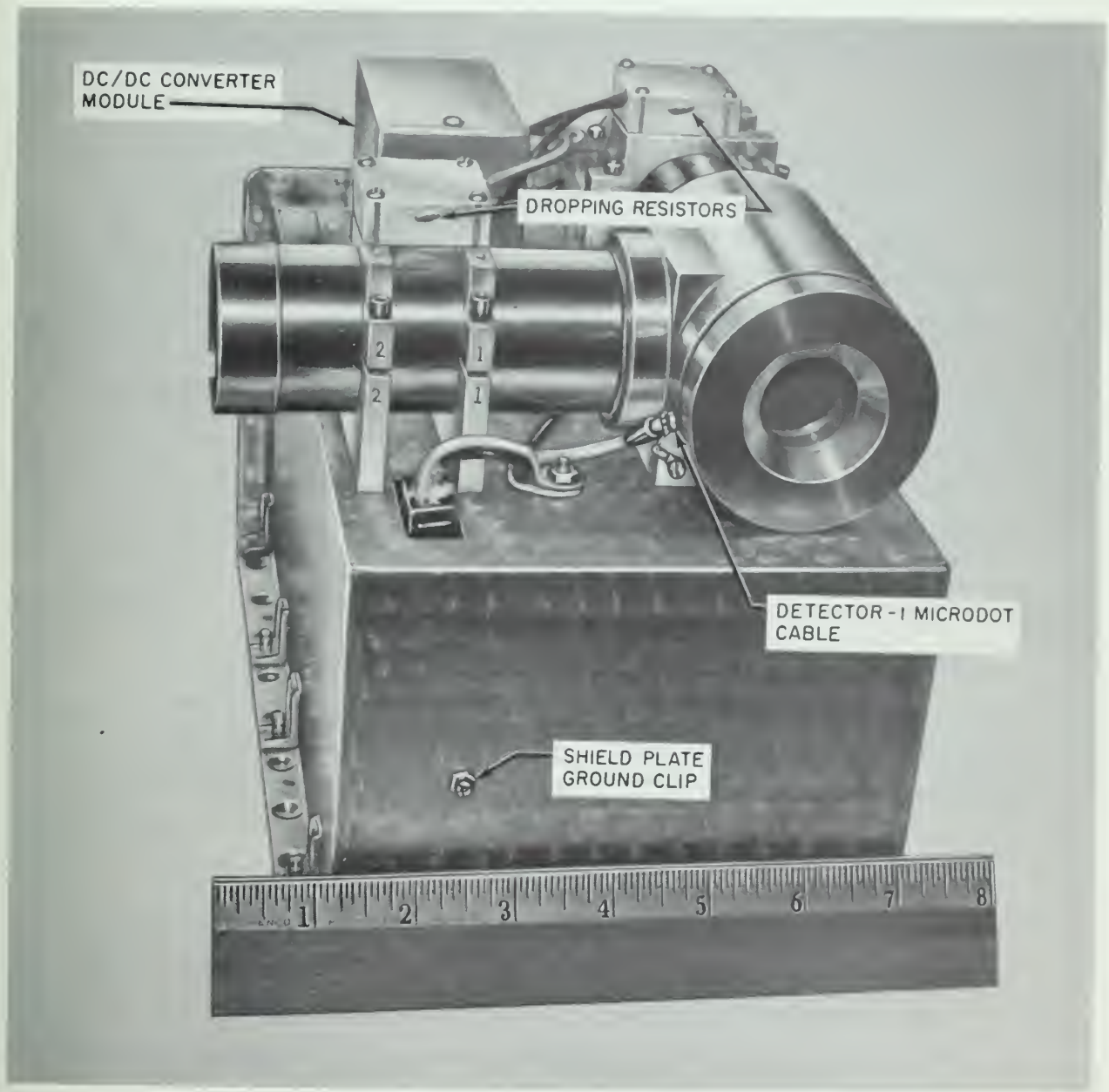

Figure 52. The Instrument (Front View)

The electronics can provided the structural frame to the instrument. It consisted of an open-faced, rectangular box formed by seam-welding 0.085-inch-thick magnesium plate for the roof and three sides, and then riveting this superstructure to a floor plate of 0.125-inch-thick magnesium. A filigreed plastic liner, backed with sponge rubber, was suspended by a floating screw from the roof of the electronics can. This roof liner was grooved to receive the printed-circuit boards and to hold them under compression.

The electronics drawer (figures 32 and 38) consisted of the eight printed-circuit boards held by grooves in a filigreed plastic floor liner, and a 0.125-inch-thick magnesium end plate which supported the floor liner by six 4-40 screws. The wire and cable connections between printed-circuit boards were routed along and fastened with clamps and ground straps to the end plate. For assembly (figure 33), the electronics drawer was inserted carefully into the electronics can so that the printed-circuit boards properly engaged the grooves of the roof liner. When completely seated, the electronics drawer was fastened both electrically and mechanically to the face flange of the electronics can by twenty 4-40 screws.

The high-voltage power supply module consisted of the DC/DC converter circuits which were potted in a thin-walled (50-mil) aluminum can (figure 36). The base flange of this can was fastened to the roof plate of the electronics can by four 0.25-inch machine screws.

The telescope consisted of three detectors encased in a 0.25-inch-thick aluminum housing with a pedestal, and two photomultiplier subsystems. The telescope pedestal was bolted firmly onto the roof of the electronics can by four screws with nuts. The housing of the telescope was threaded to receive the protective steel casings for the photomultiplier tubes. The inserted end face of these steel casings pressed on the outer edge of the face of the lightpipe windows. This pressure, along with the

sponge-rubber compression on the photomultiplier tube, kept the lightpipes, detectors, and tubes in contact to preserve optical coupling. Each steel casing was anchored to the roof of the electronics can near its far end by use of double-strut cradles. These cradles supported lucite potting blocks for dropping resistors which were attached to the cradle tops with 4-40 screws. See figure 52.

5. Tests, Calibrations, and Measurements

Tests to qualify the instrument for satellite flight are detailed in appendix I. The instrument was calibrated according to procedures discussed in appendix II. Limitations on measurements made with the instrument, including a discussion of energy resolution and resolving time for the instrument, are explained in appendix III.

SECTION IV

THE FLIGHT

1. Flight Package

The flight package is pictured in figure 53. Three magnetometers were mounted in the most forward section of the payload to determine its orientation relative to the magnetic field. A solar cell was used to determine orientation relative to the sun which was at 097°T (115° Mag). The solar cell (positioned 180° relative to the spectrometer telescope) had an acceptance angle of about 30°. Its signal was superimposed onto a magnetometer trace which thereby measured the spin rate at 2.55 rps. The flight vehicle was a two-stage HYDRA/IRIS rocket whose specifications are detailed by Holmquist (reference 19) in a report covering the development of water-launch techniques for scientific probes by personnel of the U. S. Naval Missile Center.

2. Flight

The flight profile is shown in figure 54. Radar track of the payload was maintained by the Atlantic Test Range ship Twin Falls Victory to an altitude of 203 km. Reconstruction of the actual flight trajectory was accomplished by inserting payload weight (125 lb) and launch angle (90° based upon visual observation) into a computer program generated from vehicle performance in earlier test firings of the HYDRA/IRIS rocket. This computed trajectory was then compared with the actual radar track and found to be in excellent agreement. Analysis of magnetometer data indicates that a slow precession of the payload did occur about a precession axis at 83° to the local horizontal with a conical apex angle of 26° and a period of about 45 seconds. For stabilization, the payload was spun about its axis. These payload motions introduced changes in the detection plane and pointing direction of the spectrometer telescope relative to the magnetic field. The changes are discernible as superimposed

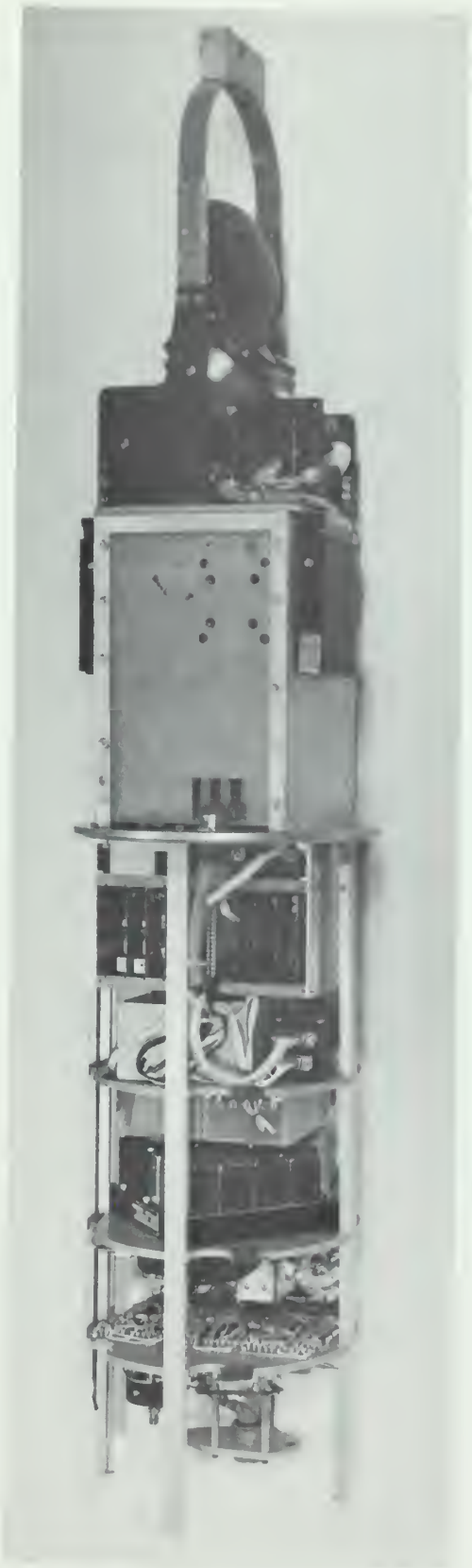

Figure 53. The Flight Package

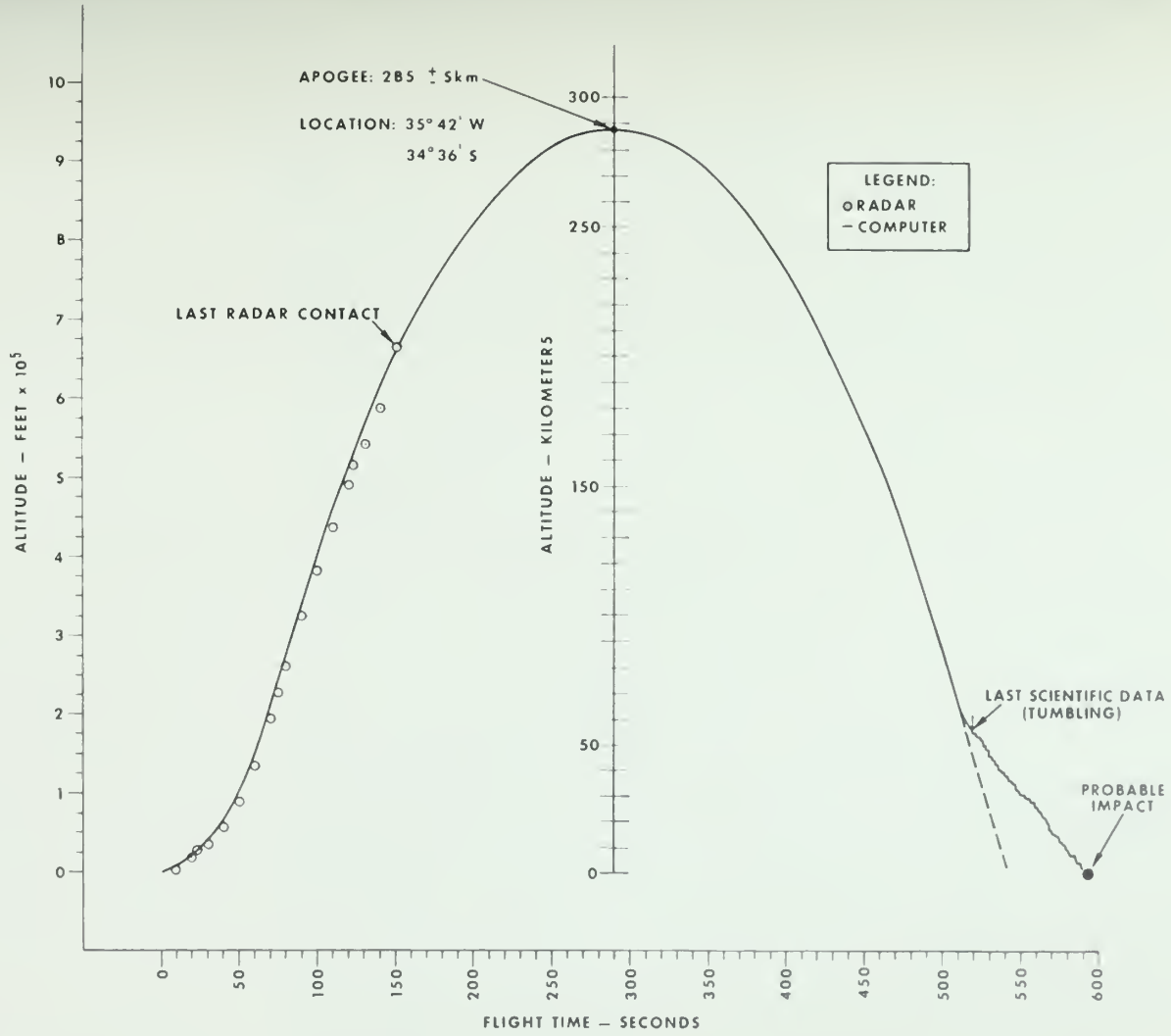

Figure 54. The Flight Profile (NMC)

systematic variations in output counting rates indicating the presence of a directional flux. Even without full compensation for these explainable variations in counting rates, proton measurements reached their maximum counting rates in the vicinity of 288-300 sec flight time (FT). This is considered in excellent agreement with the predicted apogee time of 289 sec (FT) since computed near-apogee altitudes (285±2 km) extend over 40 seconds. The agreement of radar track, predicted trajectory, and experimental counting rates establishes payload apogee at 285±5 km at a projected ground position of longitude 35°42'W and latitude 34°36'S occurring at GMT $09^h45^m15^s$ on January 26, 1965. Correlation of the predicted time of reentry was also evident in the experimental data of the flight record. The telemetry record (from magnetometers and pressure monitors, etc.) indicated that abnormalities were present at about 500 sec (FT) and that the payload underwent reentry tumbling and loss of experimental data at about 518 sec (FT). This interpretation of reentry time at 500 to 518 sec (FT) agrees quite well with predicted altitudes of 90 to 40 kilometers where significant atmospheric drag would be built up to cause tumbling during these 18 seconds. The computed trajectory of figure 54 was used unaltered for altitude determinations before reentry. After reentry the trajectory is in doubt although telemetry records indicate probable impact at about 590 sec (FT).

SECTION V

RESULTS

1. General

The flight record for the commutated telemetry channel associated with the proton spectrometer possessed 355 frames (about 400 seconds) of data from experiment turn-on, 118 sec (FT), through apogee, 289 sec (FT), and continuing until the instrument was destroyed upon reentry at 518 sec (FT). Each commutated frame of the spectrometer channel contained 0-5 volt d.c. measurements of 30 sample points including the 11 proton spectrometer output points, TM1 through TM11. Information on the counting rate versus flight altitude for the guard fluor, TM11, is shown in figure 55. The inverse atmospheric density ($1/\rho$) calculated from the U. S. Standard Atmosphere, 1962 (reference 20) is plotted for comparison. The direct correlation of the scale height of the atmosphere between 280 and 150 km substantiates that atmospheric interactions are the primary cause for counting rate decreases for radiations that activated the guard fluor in this region. The anomalous counting rates below 150 km, which were also observed in different energy channels well into the atmosphere will be analyzed in the future.

2. Specifics

a. Proton Spectrum Near Apogee

Based upon preliminary analysis of this experiment, the proton spectrum for the observed proton flux near apogee (285 ± 5 km) is shown in figure 56, which incorporates the data from table II. The counting rates for each data point were obtained by using the counting rates of the channels at apogee after minor curve-smoothing techniques were applied. Maximum counting rates occurred in most channels in the vicinity of 290 sec (FT). The altitude of this spectrum (285 ± 5 km) is the mean altitude of this time period, 288 ± 20 sec (FT). Channel TM4 data were omitted

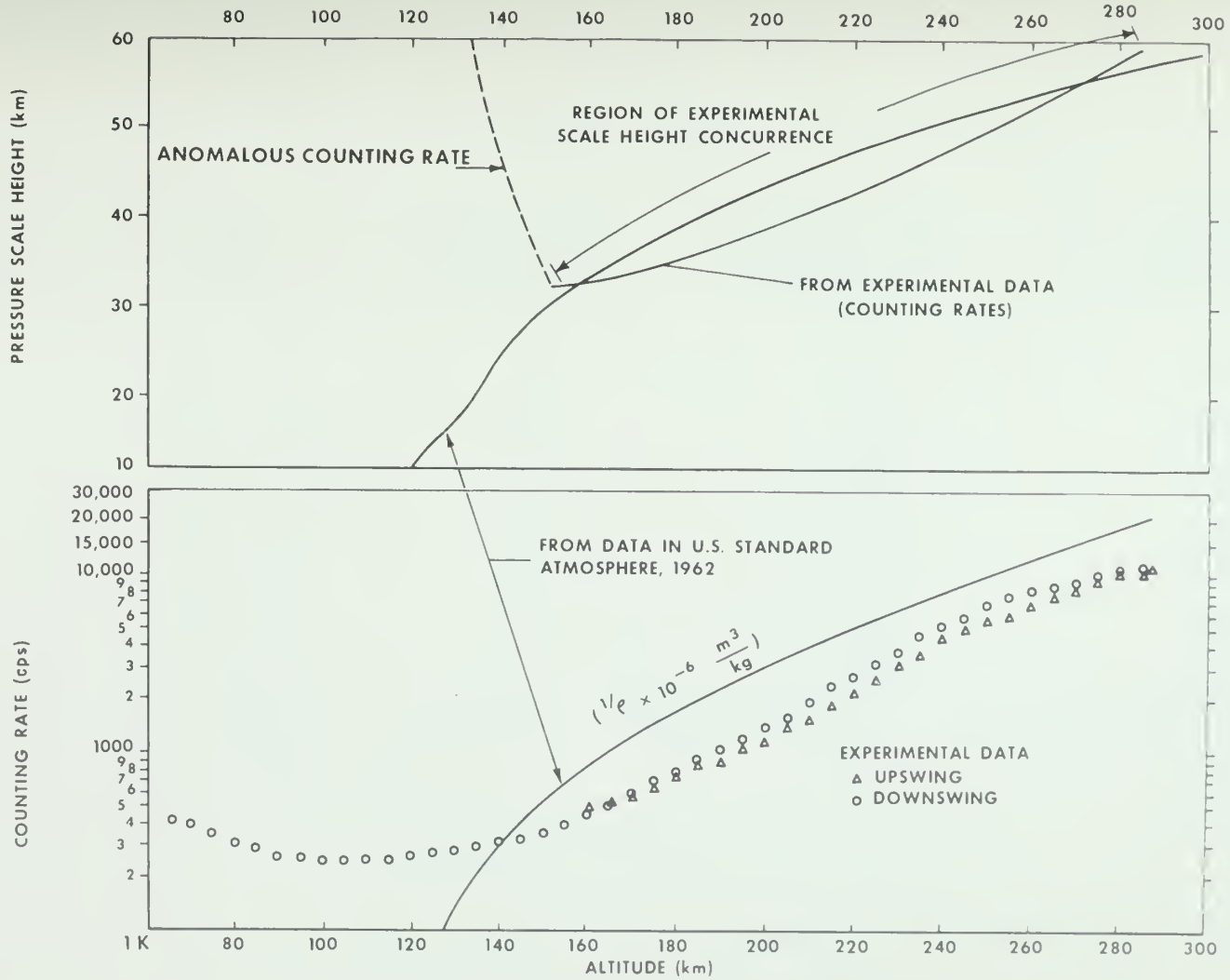

Figure 55. Counting Rates Versus Altitude

Table II

TELEMETRY CHANNELS

Channel	E Spread (Mev)	Median Energy* (Mev)	Mean Solid Angle (Steradian)	Apogee Counting Rate, j_d** Protons (cm^2-sec-Mev)
TM1	1 -- 3.6	2.2	1.6	710/1240
TM2	3.6-- 6.1	4.4	1.6	547/580
TM3	6.1-- 7.3 7.3-- 7.8	6.8	1.6 0.48	33.3/74
TM4	7.8-- 10.1	8.7	0.475	(7.4)***
TM5	10.1-- 16.3	11.7	0.468	3.3
TM6	16.3-- 29.5	21.2	0.440	0.76
TM7	29.5-- 50	39.0	0.380	0.47
TM8	50 --110	68.0	0.280	0.37
TM9	110 --200	Unreliable (probable failure of coincidence gate)		
TM10	Above 260 kev	---	1.6	---
TM11	Above 1 Mev	---	---	---

*Median Energy, $\bar{E}$, derived from the definition $\int_{E_1}^{\bar{E}} F(E)dE = \int_{\bar{E}}^{E_2} F(E)dE$

where F(E) is the local experimental spectrum between E_1 and E_2.

**$j_o = 1.27\ j_d$.

***See text.

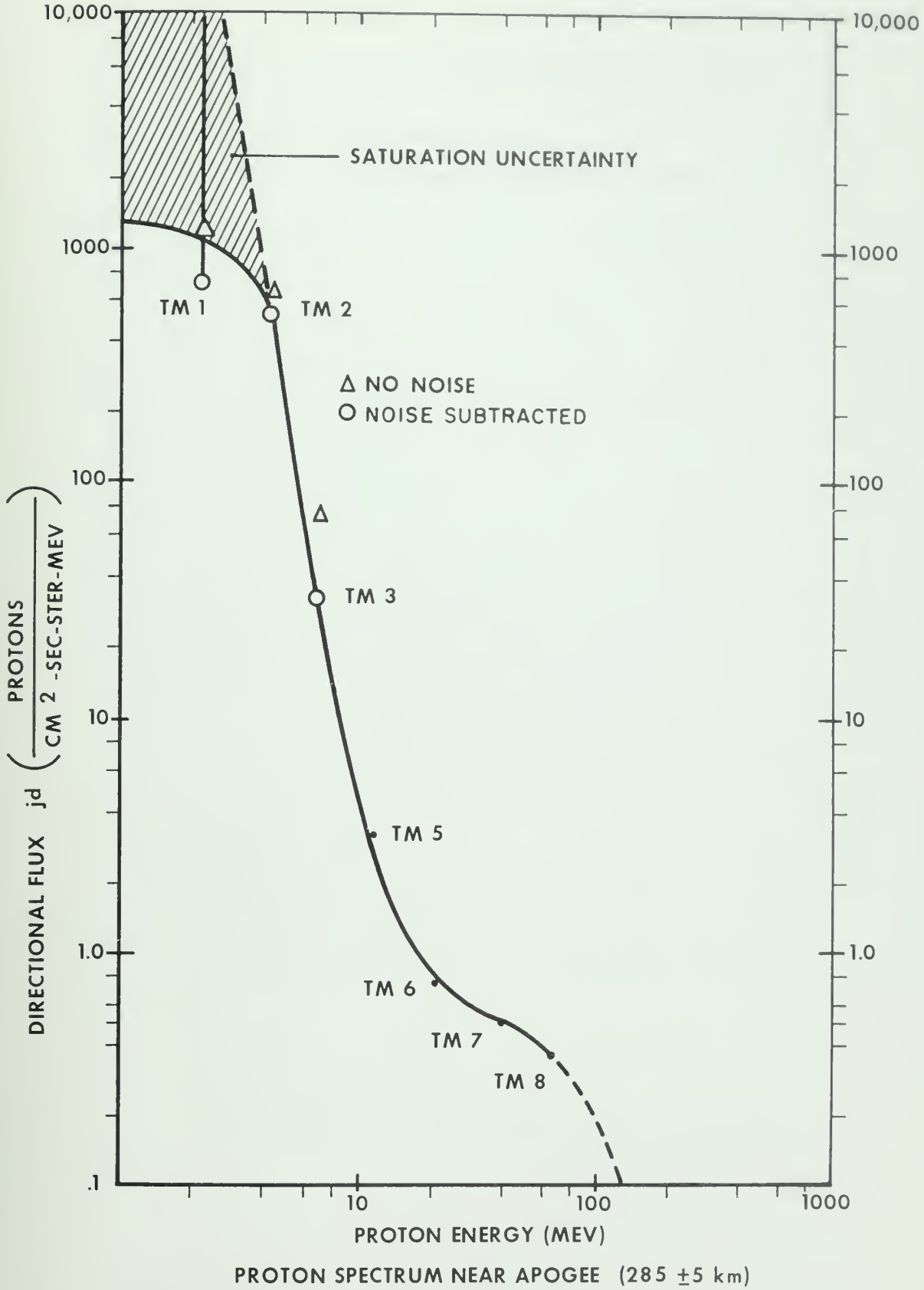

PROTON SPECTRUM NEAR APOGEE (285 ±5 km)

Figure 56. Proton Spectrum Near Apogee

from the spectrum because of difficulty in preliminary data reduction. The uncertainties of the points TM1, 2, and 3 arise primarily because of the probable presence of telemetry pickup noise due to last-minute payload integration problems. This interference was observed in analysis of the preflight check which indicated output noise counts of the following magnitudes: TM1--6500 cps; TM2--450 cps; TM3--150 cps. This high noise level (if it persisted in flight) somewhat degrades the count-rate measurements of TM1, 2, and 3. In TM1, actual proton counts would be registered at or near the insensitive and nonlinear saturation region of the count-rate meter. In TM2, however, the output counts were in a nonsaturated portion of its response curve throughout the flight. Its counting rate was such that at apogee the preflight noise would only be 5 percent of the observed count rate. In TM3, the preflight noise counts are of the same magnitude as its proton counts at apogee. If the noise pickup persisted at the preflight level, the data points should be plotted as shown by the circles in figure 56. However, it is probable that inflight noise was appreciably less due to the jettison of the nosecone and other improvements in the electromagnetic environment. If the noise pickup during flight decreased appreciably, say by a factor of 100, then the data points should be plotted approximately as shown by the triangles in figure 56. The measured spectrum below 10 Mev should be good to within a factor of 3. The turnover in the spectrum appears to persist despite known sources of error. Above 10 Mev the spectrum is more certain.

b. Directional Properties of Flux

The TM4 channel, 8-10 Mev protons, was counting at a high rate so that its 32-count scaler circuit frequently cycled within the sample period (0.038 sec). Fortuitously, this high counting rate permits analyzing of the directionality of protons in the 8-10 Mev range from the variations of flux measurements at calculable pointing directions of the telescope. The directional

flux based upon 172 frames (194 seconds) centered on apogee (altitudes above 250 km) is presented in figure 57. The large angular acceptance of the telescope (90°) coupled with the complicated motions of the payload undoubtedly have spread out the incident directional flux. Preliminary analysis of such data as figure 57 does indicate that these 8-10 Mev protons are probably aligned nearly at right angles to the magnetic field as observed by Heckman and Nakano (reference 7). This is expected of protons near their mirror points. The converging dipole-like magnetic field of the earth, even in the relatively low magnetic fields of the South Atlantic Radiation Anomaly, does create mirror points for the particles traveling along its field. The various conjectured envelopes based upon the flux variations shown in figure 57 indicate a strongly enhanced response in the East-West directions. To the first order, the appearance and variations in the envelopes are ascribed to the precession of the payload which brings the detection plane closer to the plane of trapped particles. Although analysis is not complete at this time, it is concluded that an East-West asymmetry of about 1.15 has been measured as a lower limit for 8-10 Mev protons. More complete analysis is necessary to unfold the complex payload motions and determine the absolute flux pattern.

c. Comparison With Other Measurements

A comparison of this experimental spectrum with the spectra of other investigators (references 16 and 17) is displayed in figure 58. The omnidirectional flux, j_o, was determined to first order on the assumption that the flux was isotropic in a plane and in all planes parallel to that plane (cylindrical symmetry). This situation exists for particles near their mirror points. With this assumption

$$j_o \cos\alpha = \int_o^{2\pi} d\phi \int_{\theta_1}^{\theta_2} j_d \sin\theta \, d\theta$$

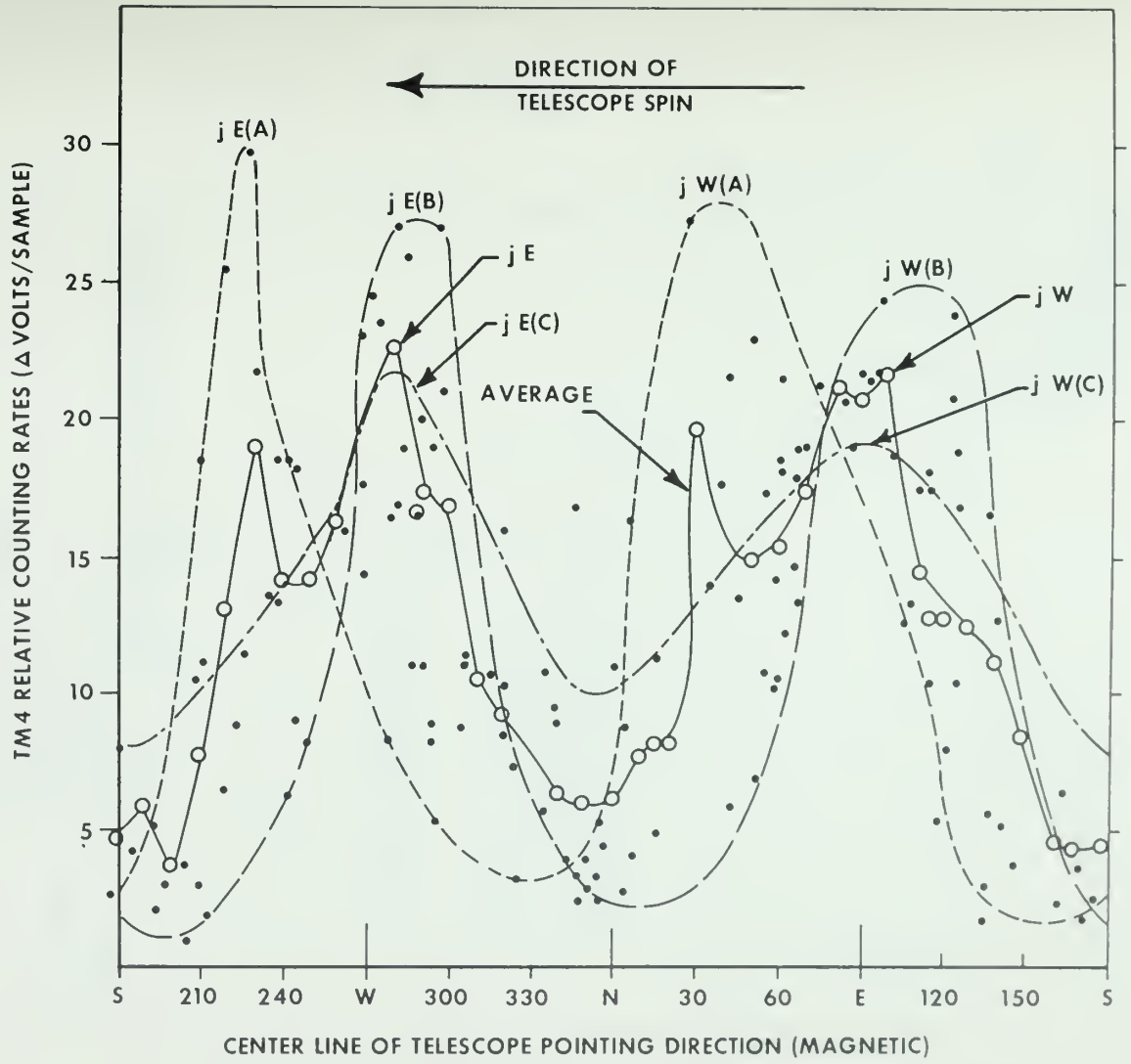

Figure 57. Directionality of 8-10 Mev Proton Flux

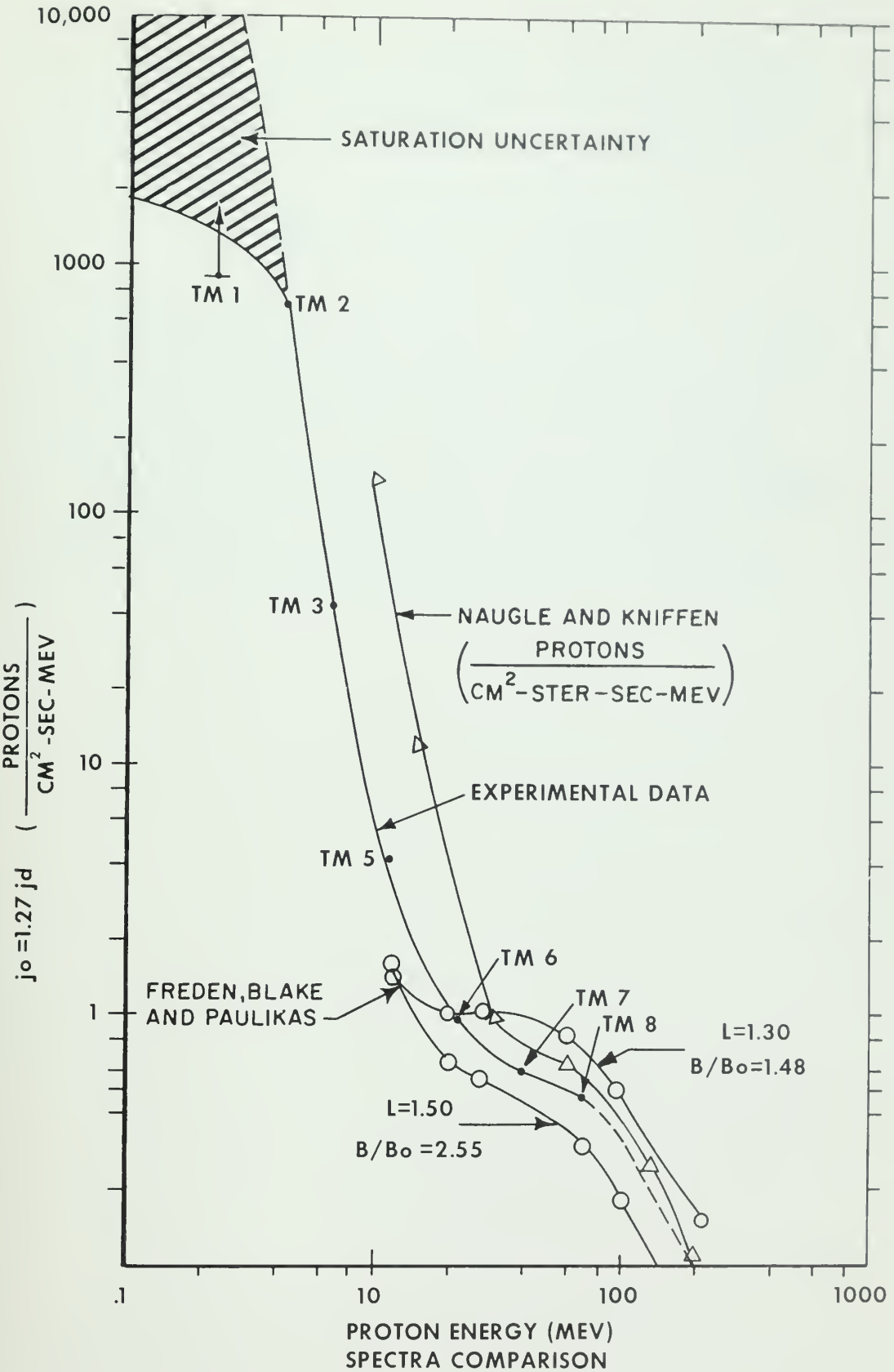

Figure 58. Comparison of Proton Spectra

where α is the angle between the magnetic field and the normal to the plane of detector rotation (~38°), and θ_1 and θ_2 define the divergence of the flux, beamwidth (assumed constant at j_d for $\pm$50).

$$j_o = \frac{j_d}{\cos\alpha}\,(\sim 1) = 1.27\, j_d \ \frac{\text{protons}}{\text{cm}^2\text{-sec-Mev}}$$

Certain similarities with other spectra are apparent. Therefore, preliminary analysis of the data from this experiment confirms that the proton spectrum within the South Atlantic Radiation Anomaly is comparable to other spectra of the Inner Radiation Zone. Furthermore, the South Atlantic Radiation Anomaly, because it dips so deeply into the atmosphere, must be considered a significant loss mechanism for protons of the Inner Radiation Zone.

APPENDIX I

QUALIFICATION TESTS

Qualification tests to establish the adequacy of the instrument for space flight were conducted using facilities of the Test Directorate, AFSWC. These tests will be discussed under the following categories:

1. Structural tests
2. Environmental tests
3. Reliability tests

1. Structural Tests

The structural tests consisted of vibration, shock, and acceleration tests of the instrument.

a. Vibration Tests

These tests were performed on a Calidyne Model 177A shock table using automatic frequency-control equipment. Sinusoidal sweep vibrations were applied to the instrument along each of three mutually perpendicular axes. Each test consisted of a single sweep starting at ~5 cycles per second and proceeding at a constant octave sweep-rate up to 2000 cycles per second for about forty-five minutes. Input levels to the equipment as measured at the shaker head were programmed in accordance with the following table:

Frequency (cps)	Amplitude
5-14	0.5 in. displacement amplitude
14-40	5 g
40-400	7.5 g
400-3000	15 g

During an early vibration check, excessive resonant vibration of the roof of the electronics can was detected. The instrument

was modified to strengthen the can at its open end with a flange support machined from 0.063-inch-thick aluminum plate. Following this modification, vibration checks were repeated and no excessive resonant vibrations were noticed. After these tests, the instrument operated satisfactorily within acceptable performance standards.

b. Shock Tests

These tests were performed on a Consolidated Electrodynamics Corporation Model HY 6407 shock piston. Shock waveforms of approximately one-half sinusoidal were applied to the instrument three times in both directions along each of three mutually perpendicular axes. Typical oscillograph pictures of various test shocks, showing the pickup signal from a Statham A5A-100-350 strain gauge, are presented in figure 59. Average shock waveforms were characteristically 12 milliseconds in duration with a 40 g peak. After all shock tests, the instrument operated satisfactorily within acceptable performance standards.

c. Acceleration Tests

These tests were performed on a Genisco g-accelerator (a 100-inch centrifuge).

Accelerations of 12 g were applied to the instrument for 10 minutes in both directions along its longitudinal and lateral axes. After all acceleration tests, the instrument operated satisfactorily within acceptable performance standards.

2. Environmental Tests

The environmental tests consisted of operating the instrument under various temperature, altitude (vacuum chamber), and humidity conditions.

a. Temperature Tests

During the development phase, all subsystems (e.g., voltage regulators, amplifiers, and count-rate meters) were checked for stability over the temperature range from -25°C to

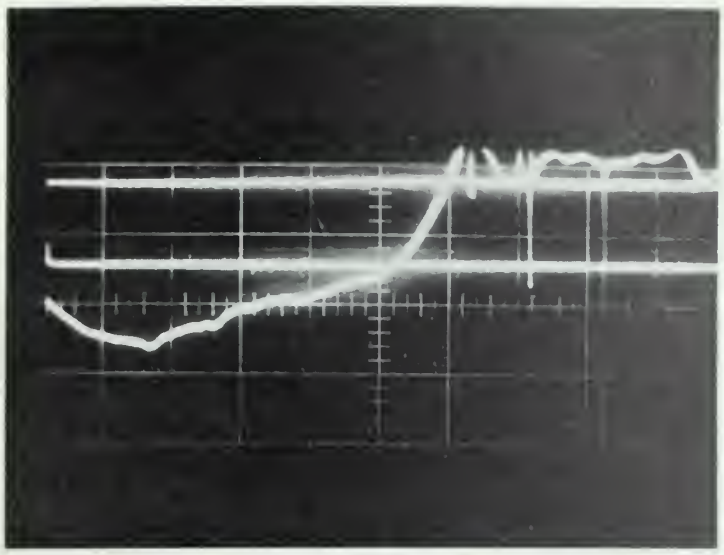

Lateral Plane No. 1
1st Line = 0 g
2nd Line = 12.4 g
3rd Line = signal (-20 g)
Time = 2 msec/cm

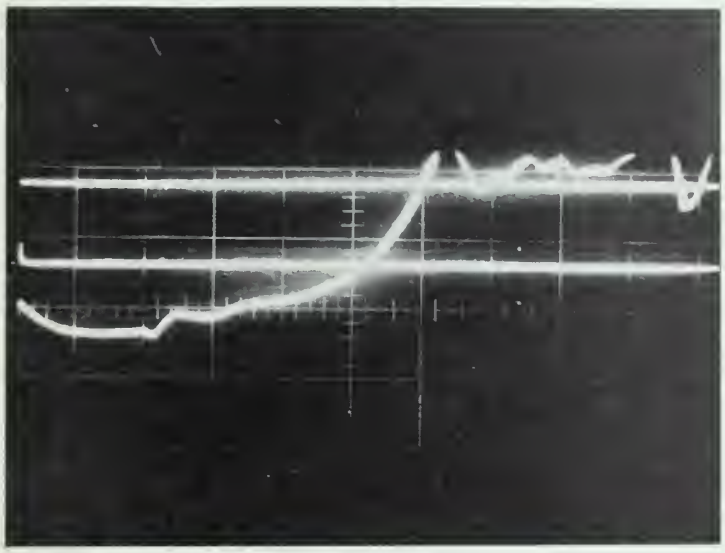

Lateral Plane No. 2
1st Line = 0 g
2nd Line = 12.4 g
3rd Line = signal (20g)
Time = 2 msec/cm

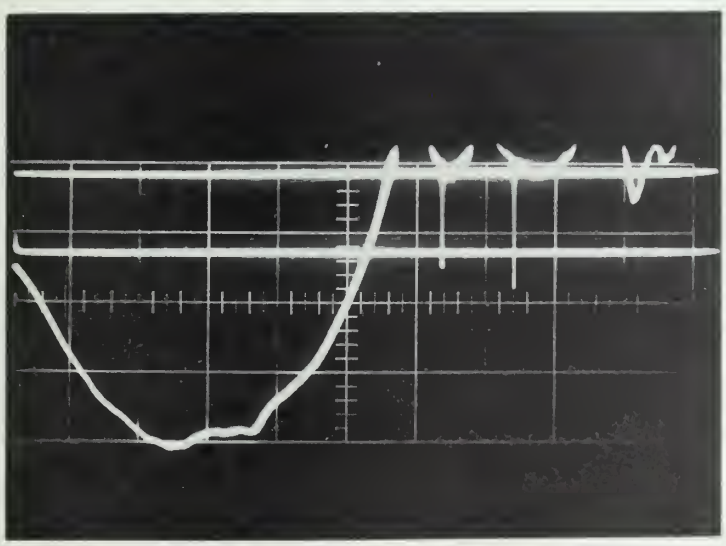

Lengthwise Shock
1st Line = 0 g
2nd Line = 12.4 g
3rd Line = signal (40 g)
Time = 2msec/cm

Figure 59. Shock Waveforms

+65°C. These tests were conducted in a temperature test chamber (Delta Design, Inc., Model 1060A) where heat transfer by means other than radiation was minimized. Design modifications were made, e.g., to count-rate meter circuitry, whenever variations in operating performance were considered excessive. During the fabrication phase, all printed-circuit boards were heat-cured after coating the conformal potting material (HySol 12005A/B) for 4 hours at temperatures between 65°C and 75°C. No defects were noted. Finally, the count-rate meters were calibrated by inclosing the instrument within the temperature test chamber as discussed later. Checks for variations in instrument response were conducted at temperatures of -25°C, at room temperature, and at 65°C. The instrument operated satisfactorily within acceptable performance standards at all temperatures tested.

b. Altitude (Vacuum) Tests

During the development phase, subsystems critically sensitive to pressure (e.g., photomultiplier tubes and high-voltage supply circuitry) were tested under vacuum for corona effects or excessive variations in operating performance. Some defects in potting techniques for photomultiplier bases were found and corrected. Finally the entire instrument was placed under vacuum and operated while cycling slowly between altitudes from zero to over 200,000 feet. Stability of operation of the instrument was verified by observing pulses due to radioactive sources at the amplified outputs of the three detectors. Each amplified output remained consistent throughout the vacuum tests.

3. Reliability Tests

The reliability tests consisted of constant operation, electrical overstress, and shelf-life evaluation of the instrument.

a. Constant Operation

During the development phase, vital subsystems were operated repeatedly for long periods (left on during six weekends) to establish failure rates and accumulate operating performance

data. The final instrument was operated constantly for three periods of greater than 16 hours without failures. To summarize, no component failures directly attributable to normal operation were observed.

b. Overstress Test

The instrument was exposed to electrical overstress tests by applying excessive input voltage up to 35 volts. No circuit failures were observed. Instrument operation (stable gain, etc.) was satisfactory in the range of 22 to 35 volts. In addition, the input isolation filter was separately tested. For a period of four hours, its input side was switched by relay action from ground to positive 27 volts at a repetition rate of six per minute. This produced over 1500 on/off current-surge cycles. No failures were observed.

c. Shelf-Life Tests

After preliminary calibration and check-out of the instrument, it was placed on the shelf in an inactive state to await a space flight. When removed from the shelf, 20 months later, tests indicated no degradation in operating performance except that the solid-state detector had, understandably, become noisy. A new solid-state dE/dx detector was procured for the flight. All other components and subsystems functioned adequately on pre-flight bench tests.

APPENDIX II

INSTRUMENT CALIBRATIONS

Calibration of the instrument consisted principally of measuring responses of the detectors and the counting circuitry, and then adjusting amplifier gains and setting thresholds of the pulse-height analyzers to achieve meaningful information.

1. Detectors

Responses of Detectors 1 and 2 were measured at the Los Alamos Scientific Laboratory (LASL). This procedure use a proton beam from a Cockcroft-Walton accelerator. Helium^3 ions were first electrically accelerated and then magnetically targeted onto a deuterium-enriched gas providing protons according to the nuclear reaction $He^3(d,p)He^4$.

The protons (~13.6 Mev) left the target area through a 0.25-mil beryllium exit window and entered the telescope through its entrance aperture.

In calibrating Detector 1, the telescope was in its flight assembly which included a low-activity, alpha-radioactive deposit of Am^{241} on each of the two aluminized mylar diaphragms. Because detector response to these 5.5-Mev alpha particles was recorded concurrently with detector response to proton beams of known energies, it was possible to establish the equivalent proton response of Detector 1 for the alpha source. These measurements thus provided reference data to permit later adjustment of system characteristics for Detector 1. Response data of Detector 1 as recorded by the LASL analyzer for proton beams of various energies used in its calibration are shown in table III. The occurrence of two energy distributions from alpha particles was discussed in section II. The linearity check for the LASL amplifiers and analyzer is shown in figure 60.

Based upon these data, Detector 1 showed a response to protons as shown in figure 61. This response curve agreed well with

Table III

DETECTOR 1 CALIBRATION DATA

ANALYZER CHANNEL	ALUMINUM ABSORBER $\left(\frac{mg}{cm^2}\right)$				
	260	200	179	132	2.0
	RELATIVE PULSE HEIGHT				
1					634
2	843	586	439	405	563
3	3,068	2,322	1,508	920	1,068
4	5,531*	4,804*	3,963*	2,817	3,251
5	2.158	2,351	3,150	3,267*	4,749*
6	691	317	605	956	1,976
7	1,476	42	86	117	254
8	3,160	27	24	36	29
9	5,113	16	24	19	27
10	6,263**	17	18	14	17
11	5,426	15	18	24	16
12	3,549	22	21	17	14
13	1,821	12	18	15	11
14	729	16	20	17	7
15	279	14	17	14	17
16	105	14	31	14	13
17	49	14	19	14	15
18	18	25	24	22	11
19	15	71	20	23	17
20	6	597	20	14	16
21	10	2,550	20	11	14
22	12	5,500	22	18	19
23	3	6,759**	49	26	15
24	1	4,519	395	23	13
25	1	1,854	2,000	25	8
26	3	536	5,956	34	12
27	1	137	8,785**	42	24
28	1	46	6,590	32	13
29	1	17	2,984	37	27
30	2	5	816	50	12
31	2	6	199	117	26
32	0	5	50	681	20
33	0	3	23	3,340	17
34		2	9	7,502	24
35		2	8	7,851**	18
36		2	1	4,240	14
37		1	1	1,233	26
38		1	1	255	26
39		1	1	60	20
40		4	2	25	23
41		0	0	6	25
42		1	1	1	28
43		2	1	3	23
44		0	0	0	19
45		1	0	0	42
46		1	0	1	312
47		0	0	1	2,318
48		0	0	0	6,268
49		1	2	2	6,559**
50		0	1	0	3,168
51		0	0	0	886
52			0	0	177
53			1	0	29
54				1	6
55				0	7
56					1
57					0
58					1
59					0
60					0

* Am^{241}
** PROTONS

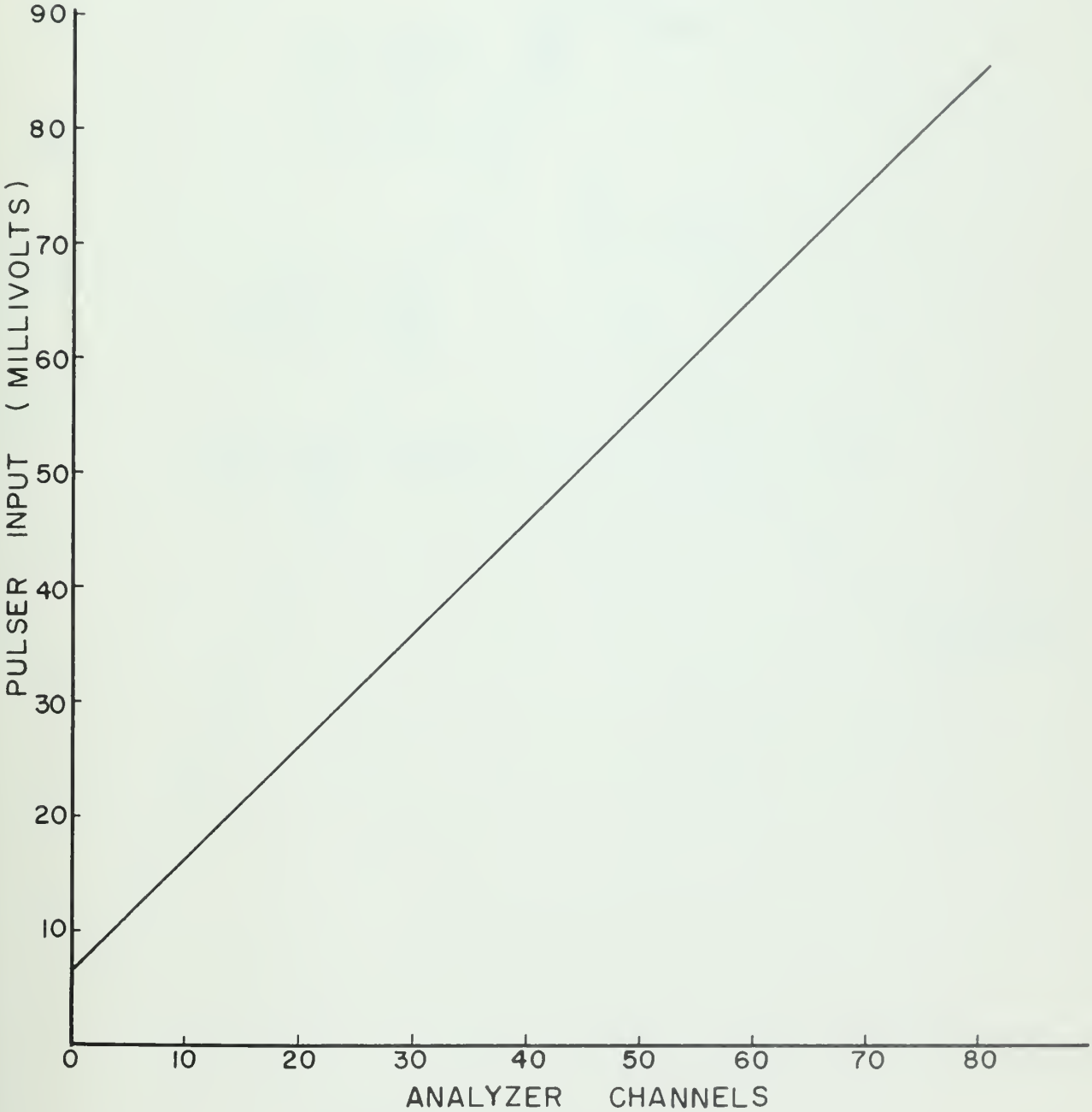

Figure 60. Amplifier and Analyzer Linearity Check

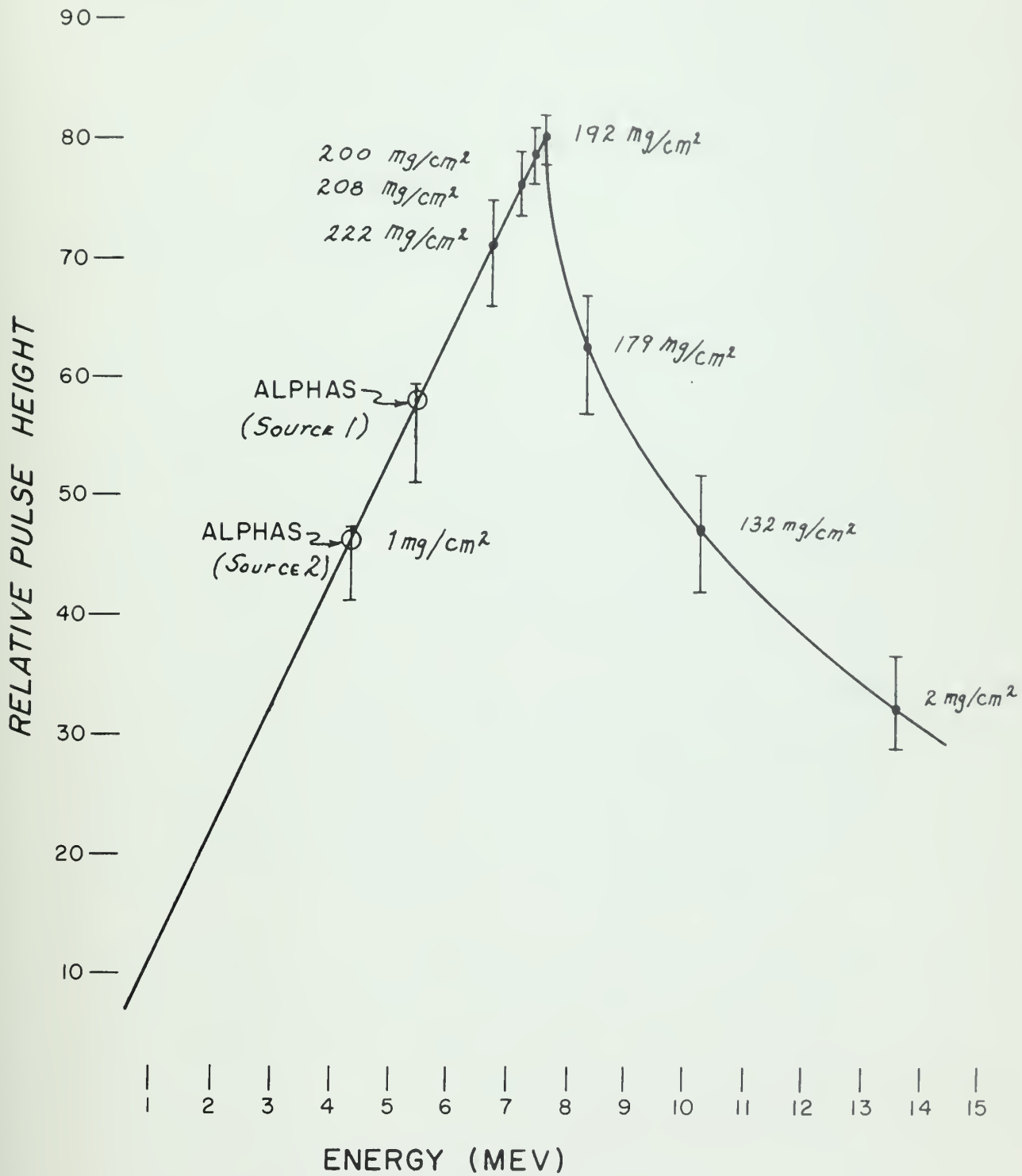

Figure 61. Calibration Curve - Detector 1

theoretical expectations based upon the data furnished by ORTEC. It should be noted that the peak of the more energetic alpha distribution corresponds, as expected, to the peak from a distribution of 5.5-Mev protons. The small departure of experimental points from linearity in the vicinity of the maximum stopping energy (7.6 Mev) is attributed to a "folding back" of protons that transit the detector, thereby distorting the pulse-height distribution in the vicinity of 7.6 Mev.

System calibration for Detector 1 consisted of adjusting the most energetic signal pulses (caused by alpha particles) as measured at the low-gain output stage of the charge-sensitive amplifier to a predetermined voltage (8 volts). This setting calibrated that voltage level to an equivalent monoenergetic proton of 5.5 Mev. The most energetic signal was chosen for setting this level rather than the peak of the distribution because this energy level was to be used as a transition between telemetry channels TM2 and TM3. Such a threshold setting would record the pulses from the inflight-calibration sources in one telemetry channel, TM2. This level was set using Technical Measurements Corporation Model 402 multichannel analyzer to compare the distribution of alpha pulses with monoamplitude pulses of the predetermined voltage. These monoamplitude pulses were generated by a Radiation Instrument Development Laboratory Model 47-1 Pulse Generator which shaped the pulse to correspond closely to alpha pulses.

In calibrating Detector 2, the telescope was not in its flight assembly. First, Detector 1 was removed to utilize the 13.6-Mev protons available. (It was necessary to remove all major absorptive materials from the path of the beam before it entered Detector 2.) Second, another similar aluminized mylar diaphragm without Source 1 was substituted for the diaphragm nearest the entrance of the telescope (Source 2 on the diaphragm side nearest to Detector 2 provided 5.5-Mev alpha particles for a reference standard). This calibration procedure was justified because Detector 2 is affected only by Source 2 since during

flight all alpha particles emitted from Source 1 (on the front diaphragm) are totally absorbed by intervening materials. Response data of Detector 2 as recorded by the LASL analyzer for proton beams of the various energies used in its calibration are shown in table IV. Based upon these data, Detector 2 showed a response to protons as shown in figure 62. This response curve is in fair agreement with the data of Meyer and Murray (reference 16) (figure 7). Considering that factors of source geometry and light collection greatly influence detected pulse distributions, the measurements which indicated that 5.5-Mev alpha particles have responses in Detector 2 equivalent to ~2.83-Mev protons were reasonable.

System calibration for Detector 2 consisted of adjusting the signal pulse equivalent to the peak of the alpha pulse distribution as measured at the high-gain output stage of its amplifier to a predetermined level (4.0 volts). This setting calibrated that voltage level to an equivalent proton energy of 2.83 Mev. This setting was made in the same manner as discussed earlier in the calibration of Detector 1.

Since Detector 3 was not used for pulse-height information, it was not formally calibrated for response to particle radiation. Instead, a suitable lower threshold of system response was set while exposing the guard fluor to 1.33-Mev gamma rays from a radioactive cobalt-60 source. System calibration for Detector 3 consisted of adjusting the gain of its amplifier so that the majority of pulses (~90 percent) from the 1.33-Mev gamma rays were sufficient to trigger anticoincidence and counting circuitry. Triggering required pulse amplitudes of approximately 2 volts at the high-gain output of the amplifier. No radioactive source was used in flight to check system gain stability for Detector 3.

2. Counting Circuitry

Counting circuits were calibrated by using a variable-frequency Rutherford Model B7 Pulse Generator to provide input pulses to the systems. Frequencies were determined with a

Table IV

DETECTOR 2 CALIBRATION DATA

ANALYZER CHANNEL	ALUMINUM ABSORBER $\left(\frac{mg}{cm^2}\right)$								
	1	222	208	200	192	185	179	132	2
	RELATIVE PULSE HEIGHT								
20	195	92	66	75	124	113	38	101	53
21	225	110	48	88	138	97	52	171	99
22	220	122	70	94	143	112	42	261	201
23	219	105	72	98	150	122	38	639	567
24	246	127	80	93	149	142	66	1,536	1,440
25	275	153	101	101	198	131	61	3,214	3,115
26	322	133	102	126	210	153	57	4,810	4,689
27	379	204	140	146	236	197	79	5,225	5,108**
28	449	208	148	158	274	246	86	4,136	3,983
29	511	225	168	199	309	225	101	2,545	2,392
30	561	292	177	192	334	287	101	1,171	998
31	582	321	240	252	405	299	123	599	364
32	747	347	245	276	486	368	147	480	199
33	878	396	284	323	572	455	159	542	156
34	1,013	528	331	389	616	473	207	628	177
35	1,122	586	350	388	670	575	225	885	201
36	1,271	636	400	483	820	671	257	1,258	228
37	1,400	718	440	520	820	714	281	1,644	245
38	1,544	762	526	569	924	784	317*	2,269	243
39	1,767	881*	586*	600*	1,013*	833*	273	3,043	255*
40	1,785*	759	510	561	857	613	316	3,316**	186
41	1,488	426	324	409	504	360	159	3,299	96
42	916	270	195	238	301	278	130	3,309**	90
43	570	215	180	187	333	308	119	2,824	83
44	529	285	195	199	369	398	158	2,166	92
45	656	303	205	247	478	478	229	1,361	131
46	690	375	263	282	538	571	290	975	147
47	760	426	245	342	602	780	432	667	141
48	962	520	338	384	747	940	594	600	195
49	1,052	564	384	437	883	1,149	692	598	192
50	1,135	652	411	471	1,003	1,324	868	619	192
51	1,394	704	455	539	1,065	1,740	1,046	686*	229*
52	1,544	769*	509*	579*	1,271	1,925	1,184	672	226
53	1,680*	696	492	526	1,321*	2,340	1,355	445	129
54	1,538	447	343	420	1,154	2,409	1,444	210	42
55	1,115	240	180	227	1,072	2,838	1,462	64	22
56	472	158	95	160	1,258	3,263	1,456	39	19
57	86	226	56	138	1,495	3,603	1,469**	30	17
58	34	412	55	208	1,861	3,817**	1,363	21	12
59	24	721	53	238	2,113	3,756	1,235	22	11
60	9	1,205	91	307	2,443	3,772	1,120	16	9
61	1	1,976	80	366	2,574	3,586	935	27	13
62	1	2,711	113	407	2,780	3,294	779	17	11
63	0	3,608	149	461	2,807	2,865	553	16	9
64	0	4,273	210	464	2,852	2,320	379	13	8
65	0	4,459**	371	525	2,724	1,971	277	18	7
66	1	3,948	670	556	2,600	1,483	188	15	10
67	0	3,222	1,163	649	2,432	1,224	125	17	8
68		2,330	2,110	752	2,279	961	92	18	10
69		1,528	3,269	946	2,160	769	51		8
70		891	4,062	1,548	2,015	624	32		4
71		515	4,318**	2,414	2,033	427	29		11
72		293	3,711	3,471	2,511	425	18		4
73		163	2,684	4,064**	3,429	412	14		4
74		65	1,465	3,486	4,394**	494	15		
75		20	602	2,177	3,377	460	13		
76		1	149	707	1,115	210	7		
77		1	26	121	180	61	11		
78		2	3	13	31	47	4		
79		0	0	1	9	17	3		
80		1	1	0	7	6	8		

* Am^{241}

** PROTONS

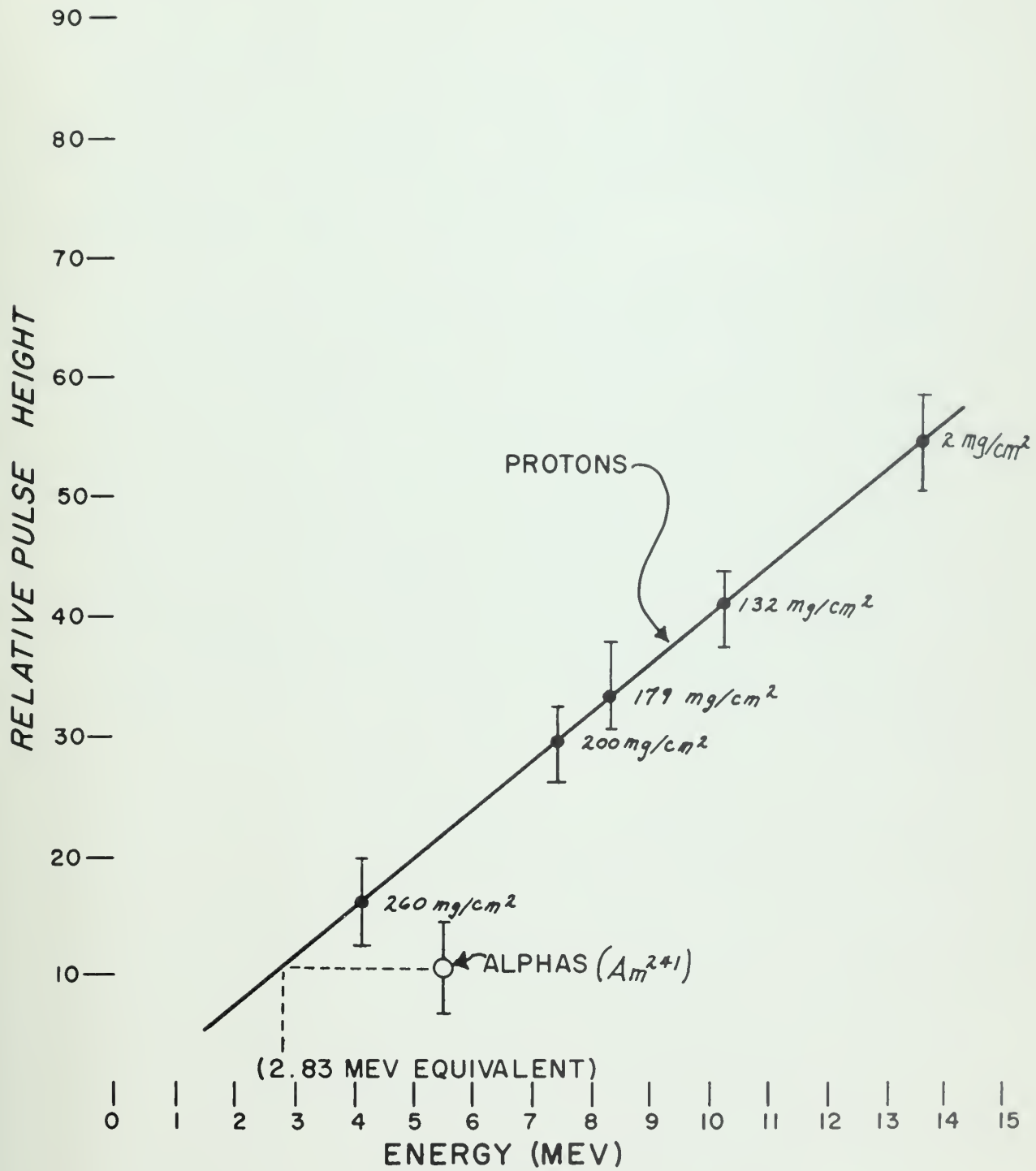

Figure 62. Calibration Curve - Detector 2

Beckman Model 5571 Frequency Meter. A Hewlett Packard Model 405 AR Digital Voltmeter was used to measure output voltages of the count-rate meters. An oscilloscope was used to measure voltage, sequencing, and proper operation of scaling circuits. Because of telemetry limits, maximum outputs of both type circuits were set at positive 4.95 volts d.c. This upper voltage limit represented 20,000 counts per second on the count-rate meters, or the 31st-step level on scaling circuits.

For the five count-rate meters used, voltage versus counting-rate curves were obtained between 10 and 20,000 counts per second at three temperatures (-25°C, room, and +65°C). Variations in output due to temperature were negligible. All runs on all count-rate meters fell within a variation of ± 5 percent from the typical "S" calibration curve (figure 18). The six scaler circuits were observed as "staircases" on an oscilloscope. Frequency response of the scalers was checked by comparing the time duration for 32 counts on an oscilloscope with the frequency of pulse inputs to the amplifier of Detector 2. Outputs of the scalers were both linear in voltage and accurate in frequency to better than 1 percent.

APPENDIX III

DATA REDUCTION METHODS AND LIMITATIONS

1. Methods

The 10-minute telemetry flight data were recorded on a magnetic tape using standard IRIG B format. Visirecorder traces were generated from the tapes for the preliminary analysis. The eleven commutator points associated with the proton spectrometer were stripped out along with the magnetometer traces, sun sensor signals, and the timing channel. Each of the 355 frames of useful experimental data was initially read visually (later the tape was processed by computer). These d.c. readings (accurate to 0.1 volt) were hand plotted for TM5, 6, 7, and 8 on a 0-5 volt versus frame number plot. These 31-count scaler channels displayed a characteristic monotonic rise to 5 volts and then recycling occurred. For an example of data reduction, consider the counting rates of TM7, which were such that no recycling occurred within a commutator period (~1.13 seconds), permitting unambiguous assignment of voltage levels (and subsequent differential counting rates during the commutator period). The counting rates of TM7 were averaged over five frame intervals (5.6 seconds) and hand plotted as counts per frame versus center frame number. This resultant curve was converted using the GMT time record to counts per second versus GMT time for the experimental flight data. The counting rate data of channels TM5, 6, and 8 were obtained in a similar manner; however, it was occasionally necessary to insert "phantom" cycles in regions of high counting rates where the trend of the counting-rate curve indicated a high probability that the 31-count scalar circuit had recycled during the period between samples. In every case when a cycle was inserted, the visirecorder trace was inspected to ascertain if the actual sample period (0.038 second) contained a few (1 to 3) discrete counts indicating that the true counting rate was about 30-90 cps. In telemetry channels TM1, 2, 3, 10, and 11 (which were fed by count-rate meters which

integrated the counting rates directly) no ambiguities existed. These channels were averaged over 5-second intervals to smooth out statistical fluctuations. The counting rates near apogee were combined with the energy spread of each channel and the mean solid angles calculated using double-aperture zonal geometry to provide the directional flux measurements listed in table II.

2. Limitations

Limitations on measurements by this experiment are primarily due to telescope resolution characteristics, geometrical and electrical. Geometrically, the resolution of the telescope is affected by uncertainties in "fringe" trajectories of high-energy particles which graze the aperture casing or are partially absorbed in the 17-mil aluminum liner. Although the discriminator thresholds are precisely known (and are accurate and reproducible to 0.1 volt) uncertainty (of about 0.5 Mev) exists in the thresholds of the channels TM4, 5, 6, 7, and 8 because of absorption inaccuracies at the liner interface. However, the logic of the experiment requires the next higher channel to cancel out the lower channel, so that the uncertainty of threshold due to geometrical (and absorptive) paths only represents a fuzziness in thresholds, not an overlap or duplication of events.

Electrically, because this experiment was designed for a low flux environment, the resolving time of the telescope was set at 2 microseconds. This 2-microsecond resolving time was determined by pulse stretching circuits (monovibrators in the discriminator circuits) which were chosen of this duration to ensure all coincidence-anticoincidence functions could be carried out regardless of the rise time of the signal pulse (estimated to be $\leq$0.4 microsecond). In view of actual counting rates encountered in the measurements, the effects of circuit resolving time and dead times were less than five percent. Detailed corrections for these effects should not significantly alter the results.

REFERENCES

1. Rossi, B., Trans. Amer. Geophys. Union, 41, 410 (1960).

2. Van Allen, J.A., et al., "Observation of High Intensity Radiation by Satellites 1958 Alpha and Gamma," Jet Propulsion, 28, 588-592 (1958).

3. Singer, S.F., and A.M. Lenchek, Geomagnetically Trapped Radiation, AFOSR 1518, Tech. Report 224, U. of Maryland Physics Dept., Aug. 1961.

4. Rosen, A., et al., A Comprehensive Map of the Space Radiation Environment, Final Report, STL report No. 8644-6002-RU-000, Sept. 28, 1962.

5. Kurnosova, L.V., et al., "Discovery of Radiation Anomalies Above the South Atlantic at Heights of 310-340 KM," Planet. Space Sci., 9, (1962).

6. Seward, F.D., and H.M. Kornblum, Near-Earth Charged Particle Backgrounds Measured With Polar-Orbiting Satellites, UCRL 6693, U. of California, Lawrence Radiation Laboratory, 1962.

7. Heckman, H.H., and G.H. Nakano, "East-West Asymmetry in the Flux of Mirroring Geomagnetically Trapped Protons," J. Geophys. Res., 68, 2117 (1963).

8. Lenchek, A.M., and F.S. Singer, J. Geophys. Res., 67, 4073 (1962).

9. Freden, S.C., and G.A. Paulikas, "Trapped Protons at Low Altitudes in the South Atlantic Anomaly," J. Geophys. Res., 69, 1259-1270 (1964).

10. Dessler, A.J., "Effect of Magnetic Anomaly on Particle Radiation Trapped in the Geomagnetic Field," J. Geophys. Res., 64, 713 (1959).

11. Yoshida, S., G.H. Ludwig, and J.A. Van Allen, J. Geophys. Res., 65, 807 (1960).

12. Vernov, S.N., et al., "Discovery of the Inner Radiation Belt at a Height of 320 Km in the Region of the South Atlantic Magnetic Anomaly," Soviet Physics-Doklady, 6, 893-896 (1961), translated from Doklady Akademii Nauk SSSR, 140, 1041-1044 (1961).

13. Gledhill, J.A., and H.O. Van Rooyen, "Cape Town Anomaly and Auroral Emission," Nature, 196, 973-975 (Dec. 8, 1962).

14. Vestine, E.H., and W.L. Sibley, J. Geophys. Res., 65, 1967 (1960).

15. O'Brien, B.J., et al., J. Geophys. Res.,67, 1209 (1962).

16. O'Brien, B.J., J. Geophys. Res., 67, 1227 (1962).

17. Meyer, A., and R.B. Murray, "Scintillation Response of Activated Ionic Crystals to Charged Particles," IRE Trans. Nuc. Sci., NS-7, 22-5 (1960).

18. Tuzzolino, A.J., et al., "Photoeffects in Silicon Surface-Barrier Diodes," J. Appl. Phys., 33, 148-149 (1962).

19. Holmquist, C.O., "The Water Launch of Rocket Vehicles for Scientific Probes," Proceedings of the 6th COSPAR Conference, Buenos Aires, Argentina, May 1965.

20. U.S. Committee on Extension to the Standard Atmosphere, U.S. Standard Atmosphere, 1962, U.S. Government Printing Office, Wash., D.C., 1962.

21. Freden, S.C., J.B. Blake, and G.A. Paulikas, "Spatial Variations of the Inner Zone Trapped Proton Spectrum," to be published in J. Geophys. Res.

22. Naugle, J.E., and D.A. Kniffen, "Variations of the Proton Energy Spectrum With Position in the Inner Van Allen Belt," J. Geophys. Res., 68, 4065-4078 (1963).